

Copy

NASA TM X-688

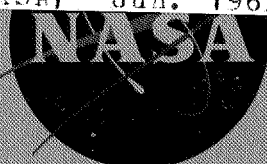
635

(NASA-TM-X-688) INVESTIGATION OF HEAT
TRANSFER AND PRESSURES ON HIGHLY SWEEPED FLAT
AND DIHEDRALED DELTA WINGS AT MACH NUMBERS
OF 6.8 AND 9.6 AND ANGLES OF ATTACK TO 90
DEG J.C. Dunavant (NASA) Jun. 1962 77 p 00/99

N72-71500

Unclas
24286

NASA TM X-688



TECHNICAL MEMORANDUM

CLASSIFICATION CHANGED
UNCLASSIFIED

X-688

TO: _____

By Authority of 6072-165 Date 4-7-72

INVESTIGATION OF HEAT TRANSFER AND
PRESSURES ON HIGHLY SWEEPED FLAT AND DIHEDRALED DELTA WINGS
AT MACH NUMBERS OF 6.8 AND 9.6 AND
ANGLES OF ATTACK TO 90°

By James C. Dunavant

Langley Research Center
Langley Station, Hampton, Va.

NATIONAL AERONAUTICS AND SPACE ADMINISTRATION
WASHINGTON

June 1962

P



NATIONAL AERONAUTICS AND SPACE ADMINISTRATION

TECHNICAL MEMORANDUM X-688

INVESTIGATION OF HEAT TRANSFER AND

PRESSURES ON HIGHLY SWEEPED FLAT AND DIHEDRALED DELTA WINGS

AT MACH NUMBERS OF 6.8 AND 9.6 AND

ANGLES OF ATTACK TO 90° *

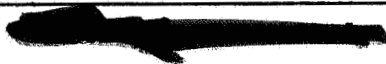
By James C. Dunavant

SUMMARY

Investigation of the pressures and heat transfer to delta wings of various sweeps, dihedral angles, and Mach numbers shows that over the range of angle of attack from 0° to 90° widely different types of flow fields exist. Knowledge of these types of flow fields and the angle-of-attack ranges for which they are present greatly enhances the prediction of pressure and heat transfer to delta wings. Spanwise pressure distributions are predictable from a strip-type flow at very low angles of attack and from a cross-flow distribution at high angles of attack. Similarly, much of the heat transfer is found amenable to prediction based on a single predominant type of flow peculiar to the angle of attack. In the angle-of-attack range from 0° to 25° the heating is best predicted by using a strip-type flow. At angles of attack from about 35° to 65° the center-line heating is best estimated from a streamline divergence theory and the spanwise distribution from a cross-flow theory. Near 90° angle of attack the flow was clearly three dimensional and not predictable by two-dimensional theories.

INTRODUCTION

Considerations of high lift and leading-edge heating make the highly swept delta wing attractive for high-lift, low-heating, hypersonic glide and reentry vehicles. The heating rates to delta wings at hypersonic speeds both to the critical leading edge and the surface of the wing are influential in determining vehicle design. Little is known about the



L
9
2
8

heat-transfer characteristics of delta wings over the angle-of-attack range from 0° to 90° , the range of interest in glider and reentry work. Thus far no generalized flow-field solution applicable over this range of angle of attack for delta wings has been found. In order to supply some of the necessary information for the successful application of the delta wings to hypersonic flight, a series of delta wings has been tested. The variables studied have been sweeps of 60° and 75° , dihedral angles from 0° to 26° , sharp and blunt leading edges, and Mach number effects at 6.8 and 9.6 in air and 18 in helium.

Previously, portions of the data and conclusions contained herein were presented in reference 1.

L
9
2
8

SYMBOLS

A	constant
a	speed of sound
c	root chord
c_p	specific heat of gas at constant pressure
C	coefficient in linear equation for viscosity
c_w	specific heat of skin material at wall temperature
D	diameter
h	heat-transfer coefficient, $\frac{q}{T_e - T_w}$
j	exponent in power-law equation
k	thermal conductivity of gas
k_w	thermal conductivity of skin material
m	mass per unit area
M	Mach number
N_{Pr}	Prandtl number

N_{St}	Stanton number based on free-stream conditions unless otherwise noted
p	static pressure
p_{max}	stagnation pressure behind normal shock
q	heat flow per unit time and area
R	Reynolds number based on free-stream conditions unless otherwise noted
R_x	Reynolds number based on distance from leading edge
T	absolute temperature
T_e	equilibrium temperature
t	time
u	velocity
x	distance parallel to chord
y	distance perpendicular to chord
α	angle of attack
α'	angle of attack of wing panel to wind
β	angle between shock and free stream
ϵ	wing semiapex angle
γ	ratio of specific heats
λ	wall thickness
θ	flow angle measured from wing center line
θ^*	theoretical flow angle at leading edge
ϕ	angle of ray through vertex measured from center line or ridge
ρ	density

4

μ viscosity

Γ dihedral angle, angle between plane of leading edges and wing panel measured in plane normal to plane of leading edges and center line

Λ sweep angle

Subscripts:

b component of flow normal to ray angle

c chord, root or chordwise

cl on center line

l based on conditions just outside boundary layer

Th theory

LE leading edge

N component of free-stream flow normal to wing-surface plane

t total

w wall

σ behind normal shock

∞ free stream

2-dim two-dimensional

Superscripts:

' boundary-layer reference condition

* sonic

L
9
2
8

APPARATUS, MODELS, AND METHODS

Apparatus

The tests were conducted in the Langley 11-inch hypersonic tunnel which is an intermittent blowdown facility with a running time of 1

to 2 minutes. In the two-dimensional nominal Mach number 7 Invar nozzle used in a part of the tests the Mach number varied with Reynolds number and to a small extent with time. At Reynolds numbers per inch of 0.05×10^6 and 0.20×10^6 the measured Mach numbers were 6.6 and 6.8, respectively. The nominal Mach number 10 nozzle had a three-dimensional rectangular cross section and a measured Mach number of 9.6 at a Reynolds number per inch of 0.1×10^6 . Air was preheated to approximately $1,160^\circ \text{R}$ for the $M = 7$ nozzle and $1,660^\circ \text{R}$ for the $M = 10$ nozzle. A more detailed description of the tunnel and some calibration data for the nozzles may be found in references 2, 3, and 4.

A contoured axisymmetric Mach number 18 nozzle using helium at atmospheric temperature was employed for one heat-transfer test. The nozzle had a calibrated Mach number of 17.8 at a Reynolds number per inch of 0.5×10^6 . Calibration data and a detailed description of the nozzle and design are given in references 5 and 6.

Models

Sketches and dimensions of the eight wing models tested are shown in figure 1. Models I to V were formed of Inconel sheet $1/32$ inch thick. On model VI the instrumented surface was 0.050 inch thick. Variation in the instrumented skin thickness on any model was no more than 0.0015 inch. Model size was largely limited by tunnel size, the smaller models being designed for operation at higher angles of attack. The sharp-edge models were made from top and bottom sheets, prebent and preinstrumented; they were brazed together at the leading edge on a roll seam electric welding machine. Braze material was a 0.002- by $1/8$ -inch ribbon of material, the length of the seam. After brazing, leading edges were ground to a thickness of 0.001 to 0.002 inch.

On the models with 0.1-inch leading-edge radius, the blunt leading edges were bent into the surface to be instrumented. Thus, the instrumented portion of the model and leading edges were of continuous sheet. The other surface was bolted to the leading edge just beyond the shoulder, and the lap joint was smoothly faired. The assembled skins were mechanically fastened to a $1/4$ -inch-thick base plate and integral sting for mounting in the tunnel.

Model VII was designed to operate at angles of attack to 90° . Separate pressure and heat-transfer models were made. The pressure model was a $3/16$ -inch-thick square-edge plate with exposed pressure leads running inside a sting attached to the rear surface near the center of the model. The heat-transfer model was similar except the surface was an 0.080-inch-thick square-edge steel plate supported by three small pins

(to reduce conduction) from a windshield behind the model. The windshield extended nearly to the edge of the model and was separated from the edge of the model by a 0.015-inch air gap for insulation. Model VIII was made of solid brass and was instrumented for pressures but not for heat transfer.

Thermocouple and pressure-orifice instrumentation was installed before assembly of the sheet-metal welded models. Chromel-alumel thermocouple wires (No. 30 gage) were spot welded to the surface separately but less than 1/32 inch apart. Pressure orifices and leads had a 0.060-inch inside diameter at the model surface. Orifice lead size was increased to approximately 0.14-inch inside diameter just beyond the model sting. All instrumentation leads came out through the sting in the base of the model. Pressure-orifice and thermocouple locations are given for each model in table I. On models having both pressure orifices and thermocouples, pressure orifices were located on one-half of one surface of the model and thermocouples on the other half of the same surface; thus the pressures and temperatures were both recorded during the same test although at different times. During the 60-second running time required for pressure-instrument stabilization the thin-skin models heated severely. Where one side of a model was particularly exposed to the heating and the other was sheltered, the differential heating of the two skin surfaces caused the model to bend. The chordwise bending of the model was observed in the schlieren photographs. It is believed that the models also bent in the spanwise direction although this was not observed. Upon cooling the model returned to its original shape. At the time the heat transfer was measured (approximately 2 seconds after the start of the flow) no bending of the models could be detected in the schlieren photographs. The temperature differences between the surfaces of the model were so little that the models could not be deformed at this time. The surfaces of pressure models VII and VIII which were made of a single skin were not bent at the end of the test. The effects of thermal distortion of the models on measured pressures are discussed with the presentation of the pressure data.

L
9
2
8

Methods

Pressures.— Pressures were recorded on six-cell aneroid recording-type pressure instruments and were read at approximately 60 seconds after the start of the test to insure that the instruments were fully stabilized. The accuracy of the cells is $\pm \frac{1}{2}$ percent of the full-scale deflection. Maximum inaccuracy of pressure measurements is estimated to be ± 3 percent. The angle of attack for the pressure tests as well as for the heat-transfer tests was measured from schlieren photographs taken 2 seconds after the start of the test.

Heating.- Aerodynamic heating was measured by the transient calorimetry technique by which the rate of heat storage in the skin is measured. Temperatures of the skin were continuously recorded on two 18-channel D'Arsonval type galvanometers calibrated for temperature. The airflow temperature was stabilized through the electrical heater by bypassing the air around the tunnel. A quick-opening valve released air to the nozzle at zero test time. Temperature-rise rates were read as soon as the flow conditions were stabilized and while the model was at a nearly constant temperature and conduction was a minimum. Approximately 2 seconds were required to stabilize the stagnation temperature and pressure in the $M = 10$ nozzle; however, because of the higher mass flow in the $M = 7$ nozzle 2.5 to 5 seconds were required to stabilize the flow. Thus, conduction was significant particularly in the $M = 7$ tests and the measured q was modified by a conduction term to give the aerodynamic heating as follows:

$$q = mc_w \frac{dT}{dt} - k_w \lambda \left(\frac{\partial^2 T}{\partial x^2} + \frac{\partial^2 T}{\partial y^2} \right)$$

In practice it was found that the maximum temperature gradient was in a direction perpendicular to the leading edge and significant only in the leading-edge region. Temperatures were plotted against distance

from the leading edge and $\left(\frac{\partial^2 T}{\partial x^2} + \frac{\partial^2 T}{\partial y^2} \right)$ was determined graphically.

The maximum conduction occurring in any of the tests was 40 percent of the aerodynamic heating. However, for about 80 percent of the heating measurements at $M = 7$, the conduction was small enough to neglect.

A single heat-transfer test was made at zero angle of attack at $M_\infty = 18$ in helium. Since the equilibrium temperature of the helium was approximately 460°R , the model was cooled to provide a temperature differential for model heating. Before the test a trough was placed below the model and packed with pulverized frozen carbon dioxide which cooled the model to a temperature below 340°R . Several seconds before the flow was initiated and with the tunnel evacuated the trough was retracted to the tunnel wall. The first blast of the tunnel main flow quickly removed any remaining dry ice from the model. The model was not cooled to one uniform temperature because of conduction, particularly in the region of the model sting and base plate. However, as the model was aerodynamically heated, the skin temperature fortuitously came to a nearly constant value at one time during the test. Temperature-time rates were measured at this instant; hence conduction was practically zero.

Measured aerodynamic heating was reduced to Stanton number based on free-stream conditions where

$$N_{St} = \frac{q}{\rho_{\infty} u_{\infty} c_{p, \infty} (T_e - T_w)}$$

The equilibrium temperature T_e is always considered to be that for laminar flow - that is,

$$T_e = T + \sqrt{N_{Pr}} (T_t - T)$$

The Prandtl number was assumed to be that given at temperature T' . Since the T' equation of Monaghan (ref. 7) is also a function of Prandtl number, N_{Pr} was solved for by iteration. Within the range of these test conditions and the assumption of local flow, the local value of $\sqrt{N_{Pr}}$ was found to vary less than 1 percent from 0.84 at $M_{\infty} = 7$ and 0.83 at $M_{\infty} = 10$; these values were used in all test data reduction.

Surface film flow tests.- Shear stresses of the innermost layer of the boundary layer were studied by observing the streaks in oil on the model surface to provide an indication of the boundary-layer-flow direction. Such tests were made on the flat 75° swept wing to angles of attack of 90° and on the 26° dihedral 75° swept wing to angles of attack of 30° . Patterns made by the flow of a thick mixture of a mineral oil and lampblack distributed in dots over the entire surface were photographed after the test. At low angles of attack where the surface shear in the boundary layer was low, portions of the model were brush coated with a thinner mixture which, after the test, persisted as very thin streaks of mostly lampblack.

DISCUSSION AND ANALYSIS

Pressures

In figure 2 side-view schlieren photographs show shock waves at free-stream Mach numbers of 6.8 and 9.6 on the flat, sharp-leading-edge, 75° swept-wing models (square-edge models at high angles of attack) at angles of attack from approximately 0° to 90° . In figure 3 photographs are shown of the blunt-leading-edge, 13° dihedral, 75° swept-wing model at $M_{\infty} = 9.6$ for angles of attack to about 30° and in figure 4

for the 13° dihedral, blunt-leading-edge, 60° swept model at angles of attack to 47.5° . Shocks are straight on the sharp-leading-edge models (fig. 2) at angles of attack to almost 70° . At $\alpha = 70^\circ$ a small curvature of the shock can be seen at both $M_\infty = 6.8$ and $M_\infty = 9.6$ and at $\alpha = 90^\circ$ the shocks are highly curved. At $\alpha = 90^\circ$ and $M_\infty = 9.6$ an irregularity and fading out of the shock can be seen at the apex (top of photograph) which is caused by the apex of the model protruding into the tunnel-wall boundary layer. This condition is also barely discernible at $\alpha = 70^\circ$ and $M_\infty = 9.6$ but is not seen at $\alpha = 90^\circ$ and $M_\infty = 6.8$ where the tunnel-wall boundary layer is thinner. The effect on the pressures of the apex protruding into the boundary layer is discussed subsequently.

Shocks on the blunt-leading-edge, dihedral, $\Lambda = 75^\circ$ and $\Lambda = 60^\circ$ models, shown in figures 3 and 4, are also straight except at low angles of attack as in figure 4(a) at $\alpha' = 1.1^\circ$. However, it is notable that the curved portion due to the flow about the apex extends many nose diameters from the apex at low angles of attack but is confined to perhaps 1 or 2 diameters at angles of attack greater than roughly 15° . A plot of side-view shock-wave angles measured from photographs taken in the tests at $M_\infty = 9.6$ are shown in figure 5. The shocks are seen to lie considerably closer to the wing surface than for a two-dimensional wedge-type flow. The wing with the lower sweep angle, model V ($\Lambda = 60^\circ$), has shock-wave angles which are only slightly less than those of the 75° swept wings in the range of angle of attack from 10° to 25° . The angle of attack used for comparison of wings having dihedral in this paper is the Newtonian panel angle of attack α' which is the minimum angle of the inclined wing panel (semispan wing) to the free stream and is

$$\sin \alpha' = \frac{\tan \Gamma \tan \epsilon \cos \alpha + \sin \alpha}{\left[1 + \left(\frac{\tan \Gamma}{\cos \epsilon} \right)^2 \right]^{1/2}} \quad (1)$$

Comparison of the shock-wave angle for this angle of attack shows no difference for dihedral wings (up to 26° dihedral). As was shown in reference 1 pressures on the center line beyond the influence of the apex may be correlated with the angle of attack α' for dihedral angles at least up to 26° .

Spanwise and chordwise distributions of pressure on the thin-wall heat-transfer models I, II, III, IV, V, and VI are shown in the top portions of figures 6, 7, 8, 9, 10, and 11, respectively. It is noted that these pressures are known to be in error due to thermal distortion during the relatively long running time (1 minute) required to stabilize

pressure measurements. In figures 2 and 3 bending of the model in the forward portions can be observed in the photographs for $\alpha \approx 0^\circ$ and 20° . Successive photographs of models made during tests indicated that this bending increased with the model temperature to a maximum deflection of the apex of about $3\frac{1}{2}^\circ$. This deflection could cause a maximum increase in pressure of 100 percent at 0° angle of attack and 20 percent at 30° angle of attack. Although only a chordwise bending of the model was observed, measured skin-temperature differentials would also indicate the probability of a bending in the spanwise direction but of a smaller magnitude because of the greater cross-sectional area.

Models VII and VIII were of different construction and showed no bending except a small amount near the sharp apex of model VIII. Pressure distribution from these models for the angle-of-attack range from 0° to 90° are shown in figures 12 to 15. The measured surface pressures are divided by p_{\max} which is the total pressure behind a normal shock at the free-stream Mach number. The pressure on the center line at all angles of attack is almost constant along the chord except for a few effects which are to be noted. In the low-angle-of-attack tests on model VIII ($\alpha = 0^\circ$ to 30°) the pressure is higher near the apex (fig. 12). At $\alpha = 0^\circ$ the pressure is approximately that predicted by boundary-layer displacement (ref. 4) but the high pressure near the apex persists to angles of attack of 30° where the boundary-layer-displacement effect is negligible. This condition is probably due to the slight amount of upward bending of the model near the apex, because at $\alpha = 30^\circ$ model VII (fig. 13) did not bend and the pressures are constant for the entire chord at both $M_\infty = 6.8$ and 9.6 .

At angles of attack above about 60° (fig. 13) at both Mach numbers, pressures near the trailing edge are less than those near the center of the model, a condition typical of an end effect. At 90° angle of attack the pressure was a maximum at $x/c = 0.75$ but at slightly lower angles of attack the maximum point moves forward to about $x/c = 0.2$ for $M_\infty = 6.8$. The lower pressures near the apex at $M_\infty = 9.6$ are caused by the apex of the model extending beyond the cone of uniform flow in this nozzle. At angles of attack of 50° and below pressures are almost constant for the entire length of the model.

Successful correlation of delta-wing surface pressure has been shown in references 1 and 8 for pressures on the wing center lines at distances from the nose where the pressure is invariant with distance. As indicated by both pressure measurements and the straightness of the shock waves in side view, the center-line pressure was invariant with distance far from the apex of the wings.

Spanwise distributions of pressure for the flat 75° swept wings (models VII and VIII) are plotted in figures 14 and 15. At angles of

attack of 50° and above (figs. 14(a) to (e)) the distribution of pressure is similar to that of cross-flow pressure distribution where the pressure at any x/c station decreases from a maximum on the center line to the pressure for sonic velocity at the edge. It would be expected that at even lower angles of attack this typical cross-flow distribution of pressure would exist; however, even at $\alpha = 30^\circ$, where the component of the free-stream Mach number normal to the surface is 4.8 for $M_\infty = 9.6$, the surface pressure is nearly constant spanwise. (See figs. 15(a) and 14(g).) At the lowest angles of attack (figs. 15(b) and (c)) the pressure is highest near the edges.

Hypersonic Flow Field and Viscid Surface Flow

Theory.— The inviscid flow field between the shock and the surface of a flat delta wing at positive angle of attack is indeed complex. To obtain an approximate solution to part of the flow field, it is convenient to analytically divide the flow into components which are more easily approximated. Thus, the flow at the surface of a delta wing may be divided into a component parallel to the center line and a cross-flow component normal to the center line. The component of velocity on the surface parallel to the chord is approximately the component of the free-stream velocity parallel to the chord:

$$u_c = u_\infty \cos \alpha \quad (2)$$

The component of the flow normal to the center line is produced by the component of free-stream velocity normal to the wing surface. This component is approximated from a data correlation of velocity over a disk normal to the flow at Mach numbers for which the flow is essentially invariant with Mach number. (A data correlation for a disk was used rather than that for a two-dimensional flat face because the disk data were available and a very small amount of unpublished two-dimensional data showed nearly identical surface velocities.) Such data have been correlated for sharp-edge disks and disks of various edge radii and are presented in figure 20 of reference 1. Thus, the cross-flow component of velocity on the delta-wing surface is approximated from the surface velocity on a disk normal to the flow where

$$\frac{u_b}{a_{t,N}} = f\left(\frac{x}{D}\right)_{\text{disk}}$$

For a sharp-leading-edge delta wing, superposition of the disk flow was used as

$$\left(\frac{x}{D}\right)_{\text{disk}} = \frac{\varphi}{2\varphi_{\text{LE}} \text{ delta wing}}$$

With these assumptions the angle of the flow from the center line of the wing made by adding the vectors of the two flow components is then

$$\tan \theta = \frac{\frac{u_b}{a_{t,N}} \cos \varphi}{\frac{u_\infty}{a_{t,N}} \cos \alpha - \frac{u_b}{a_{t,N}} \sin \varphi} \quad (3)$$

L
9
2
8

Since

$$\frac{u_\infty}{a_{t,N}} = M_\infty \left(\frac{T_\infty}{T_{t,N}} \right)^{1/2} = \frac{M_\infty}{\sqrt{1 + \frac{\gamma - 1}{2} (M_\infty \sin \alpha)^2}} \quad (4)$$

then equation (3) becomes

$$\tan \theta = \frac{\frac{u_b}{a_{t,N}} \cos \varphi}{\frac{M_\infty \cos \alpha}{\sqrt{1 + \frac{\gamma - 1}{2} (M_\infty \sin \alpha)^2}} - \frac{u_b}{a_{t,N}} \sin \varphi} \quad (5)$$

The angle of the flow at the leading edge of the wing may be obtained since the cross-flow component is sonic, that is, $\frac{u^*}{a_{t,N}} = 0.913$, and

$$\tan \theta^* = \frac{0.913 \cos \varphi_{\text{LE}}}{\frac{M_\infty \cos \alpha}{\sqrt{1 + \frac{\gamma - 1}{2} (M_\infty \sin \alpha)^2}} - 0.913 \sin \varphi_{\text{LE}}}$$

At high angles of attack it is possible that the flow angle at the leading edge is greater than the leading-edge angle, $\theta^* > \varphi_{\text{LE}}$. A minimum angle of attack for this condition ($\theta^* = \varphi_{\text{LE}}$) and several

sweep angles is shown in figure 16 for $\gamma = 7/5$. Note that the minimum angle of attack is not very sensitive to Mach number in the moderate and high Mach number range. The curves are terminated at the sonic normal component Mach number, $M_{\infty} \sin \alpha = 1.0$. However, it is reasonable to assume that a much higher normal component Mach number would be required to produce the cross-flow distribution of velocity that is invariant with Mach number.

Oil-flow tests.— Photographs of oil-flow traces on a flat, sharp-leading-edge, 75° swept delta wing at $M_{\infty} = 9.6$ are shown in figure 17. The variation of the oil-flow directions with angle of attack is pronounced. At $\alpha = 0^\circ$ the flow is in towards the center of wing as a result of the high boundary-layer induced pressures near the leading edges of the wing and the relatively low pressure farther in from the leading edge. A similar result is shown in reference 8 for delta wings having relatively blunt leading edges. It is not to be assumed that these oil-flow traces (particularly at $\alpha = 0^\circ$) are the inviscid-flow directions but rather that they indicate the sense of the flow of the inner edge of the boundary layer and probably do not coincide with the inviscid-flow directions as shown in references 1 and 8. An angle of attack of 15° reduces the inward flow so that the entire surface flow is almost parallel to the center line. Higher angles of attack produce a flow increasingly away from the center of the wing with all streamlines passing through the apex of the delta wing. It is of interest to note that at $\alpha = 30^\circ$ the angle of the oil traces at the edge of the wing is a little greater than the leading-edge ray angle and the leading edge of the wing has in the sense of air-flow direction become a trailing edge. When this condition occurs, a parting line similar to a stagnation line moves on to the wing from the leading edge. Increasing the angle of attack moves the parting line away from the leading edge until it reaches the center of the wing at an angle of attack of about 45° .

Measured oil-flow angles as a function of ray angle are presented in figure 18(a) for angles of attack of 30° , 45° , and 60° . Inviscid flow angles calculated from the disk cross-flow distribution are seen to underestimate the measured oil-flow angles. In figure 18(b) the flow angles are correlated by dividing by θ^* , the flow angle at the leading edge; this produces a distribution of flow angle similar to that of the theory but higher than the theory by nearly a factor of 2. Such a result might be anticipated, inasmuch as the pressure gradient at high angles of attack is likely to cause a boundary-layer-flow direction having angles greater than the inviscid-flow theory would predict.

At the two highest angles of attack, $\alpha = 75^\circ$ and $\alpha = 90^\circ$ (figs. 17(f) and (g)), the oil-flow angles were not constant along the ray and a three-dimensional stagnation point appears at $\alpha = 75^\circ$ near the quarter-chord station and moves back to about two-thirds chord

at $\alpha = 90^\circ$. The flow field must be subsonic throughout with all three edges having influence on the entire inviscid flow field between the shock and the wing surface. A theory based on the transformation of the known flow pattern on a disk to a delta wing at 90° angle of attack was presented in reference 8 and was found to accurately predict the streamline pattern and the pressure on the wing. However, comparable results cannot yet be obtained at angles of attack less than 90° . As discussed in reference 8 secondary flows in the boundary layer would be expected to be less for the delta wing at $\alpha = 90^\circ$ than at lower angles of attack when the flow approaches a radial distribution.

Photographs of oil-flow traces on a wing having 26° dihedral at a Mach number of 9.6 are shown in figure 19. At $\alpha' = 0^\circ$ (keel line parallel to the flow) the oil flow shows an inflow towards the keel line of the model as did the flat wing; however, with the presence of the keel the flow lines from the two panels now intersect with a significant angle at the keel. (Compare with fig. 17(a).) At $\alpha' = 13.5^\circ$ the oil-flow lines are out from the keel line, whereas on the flat wing at this angle of attack the oil flowed approximately parallel to the center line. (See fig. 17(b).) In figure 19(c) for $\alpha' = 27^\circ$, there is a strong outward flow of the oil and the flow angles even at the keel line are large. (Compare with fig. 17(c).)

If each panel of a dihedralized delta wing is considered separately, a surface angle may be obtained from a Newtonian type of flow analysis. This flow direction is along the surface streamline that requires the least deflection of the free-stream flow. In terms of wing-geometry definitions used herein the angle of the surface flow from the keel line in the plane of the wing panel is given by

$$\sin \theta = \frac{\sin \alpha + \cos \alpha \tan \Gamma \tan \epsilon}{\sqrt{1 + \left(\frac{\cos \alpha}{\tan \Gamma} - \tan \epsilon \sin \alpha\right)^2} \sqrt{1 + \tan^2 \Gamma \tan^2 \epsilon}} \quad (6)$$

where θ is measured in the plane of the wing panel and α is the angle of attack of the plane of the leading edges. In figure 20 the oil-flow angles measured at $\alpha' = 27^\circ$ (fig. 19(c)) are plotted for the spanwise location. The trend of the angle variation is similar to that of the flat wing, as shown in figure 18(a), but the angle is greater by almost a constant increment. A theory can be predicted, based on the addition of a constant (with span) incremental angle of the flow due to Newtonian component and an inviscid flow angle derived as for the flat wing from the cross flow on the equivalent disk. This value shown in figure 20 overestimates the flow angle inboard and underestimates

the angle outboard, whereas the theory consistently underestimated the flow angle for the flat wing (fig. 18(a)).

Heat Transfer

Theory.- If the observed oil-flow patterns can be considered a valid indication of the inviscid flow field over the delta wing, then a continuously varying (with angle of attack) flow field is seen to change from a flow direction nearly parallel to the chord at low angles of attack to one with very large spanwise flow components at high angles of attack. Comparison of some simple calculations of the flow field with experimental data has produced an inconclusive result in that considerable differences did exist, even though logically explainable, between the measured oil-flow angles and the calculated flow angles. Even though a generalized flow-field solution is lacking, heat transfer can be predicted for some flow regimes, based upon an ideal flow. At relatively low angles of attack (5° or 10°) the oil-flow streamlines were nearly parallel to the wing center line. For this case a strip or flat-plate value of the Stanton number may be obtained from the Blasius skin-friction value and a modified Reynolds analogy by using the reference-temperature T' method (ref. 7). The heat-transfer correlating parameter, with Reynolds number based upon the strip distance x , measured parallel to the center line from the leading edge is

$$(N_{St}\sqrt{R_x})_l = \frac{0.332\sqrt{C'}}{(N_{Pr}')^{2/3}} \quad (7)$$

where $C' = (\mu'T)/(\mu T')$ and local conditions are just outside the boundary layer. The correlating parameter based on the free-stream condition is

$$N_{St}\sqrt{R_x} = \frac{0.332\sqrt{C'}}{(N_{Pr}')^{2/3}} \frac{c_p}{c_{p,\infty}} \sqrt{\frac{pM_\infty}{p_\infty M_\infty \mu_\infty}} \left(\frac{T_\infty}{T}\right)^{1/4} \quad (8)$$

In figure 21 this relationship, called laminar strip theory, is plotted against angle of attack for nominal tunnel conditions at a Mach number of 9.6. Local conditions are obtained from oblique shock theory by using the angle of attack as the wedge angle.

In the high angle-of-attack regimes where significant spanwise flow is present, the heating at the stagnation point may be calculated from the velocity gradient by assuming that this gradient is produced by the component of the free stream normal to the surface. Also, it is assumed

that the tangential component of velocity influences only T_e . Squire (ref. 9) found that the Nusselt number Nu at the forward stagnation point of a two-dimensional blunt body in incompressible flow is

$$Nu = \alpha_3(\sigma) \left(\beta_1 \frac{d^2}{\nu} \right)^{1/2}$$

where $\alpha_3(\sigma) = 0.57(N_{Pr})^{0.4}$, $\beta_1 = du/dx$, d is a characteristic length, and ν is the kinematic viscosity. If, as Sibulkin did for the hemisphere (ref. 10), the free-stream conditions are assumed to be those behind the normal shock, then the heating in the present notation is

$$h = 0.57(N_{Pr,\sigma})^{0.4} k_\sigma \left(\frac{\rho_\sigma}{\mu_\sigma} \frac{du}{dx} \right)^{1/2} \quad (9)$$

and the heat-transfer correlating parameter for a two-dimensional stagnation line, based on upstream conditions, is

$$N_{St}\sqrt{R_x} = \frac{h}{\rho_\infty u_\infty c_{p,\infty}} \sqrt{\frac{\rho_\infty u_\infty x}{\mu_\infty}} = 0.57 \frac{c_{p,\sigma}}{c_{p,\infty}} (N_{Pr,\sigma})^{-0.6} \sqrt{\frac{\mu_\sigma \rho_\sigma}{\mu_\infty \rho_\infty} \left(\frac{x}{u_\infty} \right) \left(\frac{du}{dx} \right)} \quad (10)$$

This equation can be applied to the center line of the delta wing. The velocity gradient on the center line may be approximated (using the disk-flow velocity-gradient correlation of ref. 1) for a sharp-leading-edge wing by

$$\left. \frac{du}{dy} \right|_{y=0} = 0.745 \frac{a_{t,N}}{(2x \tan \epsilon)} \quad (11)$$

where x and y refer to the chordwise and spanwise coordinates, respectively.

From equations (4), (10), and (11) the heat-transfer correlating parameter for a delta wing is

$$N_{St}\sqrt{R_x} = 0.57 \frac{c_{p,\sigma}}{c_{p,\infty}} (N_{Pr,\sigma})^{-0.6} \sqrt{\frac{\mu_\sigma \rho_\sigma}{M_\infty \mu_\infty \rho_\infty} \left(\frac{0.745}{2 \tan \epsilon} \right) \left[1 + \frac{\gamma-1}{2} (M_\infty \sin \alpha)^2 \right]^{1/4}} \quad (12)$$

This relationship, called cross-flow theory, is also plotted in figure 21 for nominal Mach number 9.6 nozzle conditions. To obtain the flow properties behind the shock, the shock was assumed to be parallel to the wing surface.

If x and y are coordinates of the surface streamlines, the flow angle near the center of the wing may be obtained from equation (3) as

$$\tan \theta = \frac{u_b}{u_c} = \frac{dy}{dx}$$

$$\frac{dy}{u_b} = \frac{dx}{u_c} \quad (13)$$

Again from the disk cross flow of reference 1, the spanwise velocity near the center of a sharp-leading-edge delta wing may be approximated as (in the present notation)

$$u_b = \frac{0.745(y)^{a_{t,N}}}{2(x)\tan \epsilon} \quad (14)$$

Substituting equation (14) into equation (13) yields

$$\frac{dy}{0.745ya_{t,N}} = \frac{dx}{2xu_c \tan \epsilon} \quad (15)$$

and integrating gives

$$\frac{\log_e y}{0.745a_{t,N}} = \frac{\log_e x}{2u_c \tan \epsilon} + \text{Constant}$$

The equation for the initial shape of the streamlines near the center of the wing is then

$$y = Ax^{\left(\frac{0.745a_{t,N}}{2u_c \tan \epsilon}\right)} \quad (16)$$

Substituting equations (2) and (4) into equation (16) yields

$$y = Ax \left[\frac{0.745 \sqrt{1 + \frac{\gamma-1}{2} (M_\infty \sin \alpha)^2}}{2 \tan \epsilon M_\infty \cos \alpha} \right] = Ax^j \quad (17)$$

Now, if y is assumed to be equal to the radius on an axially symmetric body at 0° angle of attack, the divergence of the body surface streamlines with respect to the axial length will be directly proportional to the divergence of the delta-wing streamlines. Then, if the local flow conditions are assumed to be equal on the body and on the wing and if the body surface and axial lengths are equal, the Mangler transformation (ref. 11) can be used to obtain the ratio of the correlating parameter for the divergent and nondivergent flow as

L
9
2
8

$$\frac{N_{St} \sqrt{R_x}}{\bar{N}_{St} \sqrt{\bar{R}_x}} = \sqrt{2j + 1} \quad (18)$$

where j is the exponent in equation (17) and the quantities with bars are the nondivergent two-dimensional values. A similar result may be obtained from the work of Vaglio-Laurin in reference 12. This relation, called streamline divergence theory, is also plotted in figure 21. Local conditions, constant along the chord, were assumed to be those given by a single oblique shock from the delta-wing pressure correlation of reference 1.

Center-line heating.— Heating measured at $M_\infty = 9.6$ along the center line of models I and VII (flat, sharp-leading-edge, 75° swept-wing models) is plotted in figure 21. The data match the trend of increased heating with angle of attack and agree well with the strip theory in the angle-of-attack range from about 0° to 25° . This result might have been expected from the oil-flow tests which showed a flow of the oil generally parallel to the root chord in this angle-of-attack range from 0° to 30° . At $\alpha = 0^\circ$, there is a significant (although not discernible in fig. 21) change in the heating which is discussed in the section entitled "Effects of Mach number." Beginning at $\alpha = 30^\circ$ the heating deviates markedly from the strip theory and compares better with the streamline divergence theory up to angles of attack of 60° or 70° where the data no longer are correlated by the parameter $N_{St} \sqrt{R_x}$. At angles of attack of 70° and above the wing shock is curved in side view and the correlation based on a single characteristic length, either chordwise or spanwise, is expected to break down. Indeed the flow pattern at $\alpha = 90^\circ$ (fig. 17(g)) shows a three-dimensional stagnation point on the center line at about two-thirds of the root chord. The cross-flow theory predicts the heating in the angle-of-attack range from 70° to 90° for approximately the midchord station; however, being

a correlation based on span and neglecting any chordwise component of the flow, this simple theory cannot predict the heating where the flow pattern is three-dimensional as at $\alpha = 90^\circ$. At $\alpha = 60^\circ$ the cross flow does predict the heating, but at lower angles of attack it underpredicts the heating by neglecting the large chordwise component of the flow. Thus, it can be seen that much of the heating on the center line of the delta wing can be estimated by using a theory appropriate to the flow pattern peculiar to the angle-of-attack range.

Spanwise heating distribution.- To facilitate the interpretation of the variation of heat transfer over the delta wings, local heating is divided by a theoretical laminar heating calculated for the center-line station. Spanwise distributions of heating for the tests of models I through VI are compared with strip theory distribution since most of these tests were at angles of attack less than 30° . Distribution of heating and pressure for these models are shown in figures 6 to 11. Taking the distance from the leading edge and local flow condition from oblique shock theory, strip theory defines the variation of heating with span which is also shown in these figures. The data generally show agreement with the strip-theory heating distribution. Most notable disagreement (except for the high Reynolds number test shown in figure 11 for which much of the flow was turbulent) between strip-theory distribution and the measured heating is that the theory overpredicts the heating near the center of the wing at low angles of attack and also in the regions adjacent to the leading edges at angles of attack near 30° . The results are similar at a Mach number of 6.8 where laminar flow occurred. (Compare figs. 6 and 22.) Except near the keel line equally good agreement with theory is shown for the blunt-leading-edge models (models IV and V in figs. 9 and 10(a) to (d)) for heating on the flat portions of the wing. The heating very close to the leading edge, however, shows a small rise above the trend for the inner portions of the wing. This rise may be due to conduction from the hot leading edge rather than to aerodynamic heating but the small size of the leading-edge radius and lack of thermocouples in this region prevent the assessment of this effect.

Theoretical heating on the wing panels of the dihedral wings was found from oblique shock theory by assuming a wedge angle equal to the wing-panel angle of attack (eq. (1)) and a strip flow parallel to the center plane of the wing. The measured and theoretical distributions of heating for the dihedral models II, III, IV, and V are shown in figures 7 to 10. The same agreement with theory and the same effects of the flow field as found for the flat wing are present for the dihedral wing. In addition, the relatively sharp keel line on the dihedral wings causes an increase in the heating at the center of the wing above about $\alpha = 10^\circ$ for the 13° dihedral wings and above $\alpha = 5^\circ$ for the 26° dihedral wing.

The heating measured on the high-angle-of-attack model with $\Lambda = 75^\circ$ is divided by the theoretical center-line cross-flow heating from figure 21. Spanwise distribution of heating for this model is shown in figure 23 at $M_\infty = 6.8$ and in figure 24 at $M_\infty = 9.6$. The theory of Lees (ref. 13) was used to obtain the theoretical spanwise distribution of heating for comparisons with the data in these figures. The shapes of the measured heating distributions clearly resemble the theoretical cross-flow distribution of heating above $\alpha = 30^\circ$. As shown by the oil flow the surface flow is diverging from the center of the wing (figs. 17(c) to (e)) but even at $\alpha = 60^\circ$ the chordwise component of the flow is greater than the cross-flow component over most of the wing. Hence, it is probably coincidental that the measured distribution of heating should resemble the theoretical cross-flow distribution. At $\alpha = 90^\circ$ even though it has been seen that the chordwise heating is not correlated by $(R_x)^{-1/2}$ (fig. 21), the spanwise distribution of heating (figs. 23(d) and 24(g)) for individual spanwise segments are very nearly the shape of the theoretical distribution. It has been shown that the flow at $\alpha = 90^\circ$ is predictable by three-dimensional methods; however, it is not surprising that an attempt to correlate heating by a two-dimensional method should be unsuccessful.

Effects of Mach number.—Distributions of pressure and heat transfer on delta wings at hypersonic speeds are largely independent of Mach number. Most notable effect of Mach number on pressure and heat transfer was found at $\alpha = 0^\circ$ where the local surface Mach number was highest and the boundary-layer-displacement effects were greatest. In figure 25(a) the pressures measured on flat, sharp-leading-edge, 75° swept delta wings at $\alpha \approx 0^\circ$ for three Mach numbers are compared with the theoretical boundary-layer displacement pressure. Fair agreement of the trend of pressure with Reynolds number for the various rays was obtained at all Mach numbers; however, for this correlation, the pressure on the center-line ray was usually higher than for the other rays. The pressure gradient increases greatly with Mach number as can be seen in figure 25(a). The effect of this gradient and its increase upon the heat transfer is illustrated in figure 25(b). Here the heat transfer measured in the same tests is compared with that obtained from the laminar strip theory with no pressure gradient and with that obtained from a local similarity theory which uses the boundary-layer displacement pressure and pressure gradient (from refs. 14 and 15). Very little effect of the displacement pressure is seen at $M = 6.8$ for both the data and the theory. At the higher Mach numbers of 9.6 and 17.8, the boundary-layer displacement pressure and pressure-gradient theory does not correctly estimate the heat transfer. The explanation for this lies in the viscous-flow pattern shown in figure 17(a). The low-energy fluid at the surface is observed to be flowing from both sides of the wing toward the center line where apparently it greatly thickens the

boundary layer and reduces the heat transfer. The pressure gradient producing this secondary flow decreases with distance downstream from the apex. Hence, this effect should disappear if the wing were long enough but the available data do not permit an assessment of how far this effect will exist. The secondary-flow pattern disappears at angles of attack less than 15° (fig. 17(b)) and the effect on heat transfer is negligible at an angle of attack of about 12° at a Mach number of 9.6. (See figs. 6(c) and 11(b).) A similar secondary-flow effect was found in the test of the blunt-leading-edge model with $\Lambda = 70^\circ$ (ref. 8). In this test the secondary flow is caused by the high local pressures in the vicinity of the leading edge and is further complicated by the flow over the blunt apex of the model. Comparison of the heat transfer at almost 0° angle of attack for the blunt-leading-edge and sharp-leading-edge wings at $M_\infty = 9.6$ can be made from figures 6(a) and 9(a). Approximately the same heating distributions are shown.

Leading-edge heat transfer.— Heat transfer measured from the thermocouples located on the forwardmost point on the blunt leading edges of models IV and V was greatly affected by conduction. Furthermore, the lack of detailed temperature distributions around the leading edge prevented the calculation of the conduction, but correction for conduction could hardly alter the trends of relative heating along the leading edge in any one test. Nevertheless, it is interesting to observe some effects of the apex and the flow field on the relative values of the uncorrected heat transfer at these stations. The differences in the relative values of heating may be caused by changes in the stagnation-point heating rate or by some change in the flow field along the leading edge which on a delta wing at high angle of attack cannot be considered an isolated, infinitely long swept cylinder. It must be remembered that the thermocouples were located at the stagnation point for the 0° angle-of-attack condition only and the measured values of heating at other angles of attack are not indicative of the maximum heating on the leading-edge heating. The shift of the stagnation point causes the point of maximum heating to move away from the thermocouple as the angle of attack increases. The measured heat transfer divided by a calculated leading-edge stagnation-point heat transfer is plotted against leading-edge station for the 75° swept-wing model IV in figure 26(a) and for the 60° swept-wing model V in figure 26(b). Note that at all angles of attack probably only about one-half or less of the aerodynamic heating is being measured due to the heat being conducted away. The distributions along the leading edge change considerably with angle of attack. In figure 26(a) the lowest heating measured at low angles of attack was at $x/D = 3.2$ but at the highest angle of attack the greatest heating was also measured at this station. Measured heating decreases at stations beyond $x/D = 5.8$ at all angles of attack, the greatest decrease taking place at high angles of attack. Somewhat similar trends were observed on the 60° swept-wing model (fig. 26(b)) at $x/D = 3$ and

beyond. The shoulder, $x/D = \frac{1}{2}$, usually experienced the highest heating.

The trend at high angles of attack of decreasing heating with chord may be due to the formation of a conical shock which lies farther from the leading edge at the rearward stations than when the shock was parallel to the leading edge at low angles of attack. (See refs. 1 and 8 for change in plan-view shock shape with angle of attack.)

Transition. Stanton numbers measured at $M_\infty = 6.8$ in three tests at approximately the same angle of attack are plotted against Reynolds number based on a streamwise length from the leading edge in figure 27. The decreasing values of Stanton number with Reynolds number show good agreement with the laminar theory of heat transfer varying as $(R_x)^{-1/2}$. The two tests at higher Reynolds numbers show an increasing heat transfer with Reynolds number over part of the model which is a positive sign of transition. The heat transfer varies approximately as $(R_x)^{-1/4}$ for the tests farther back along the model. These values compare well with the turbulent theory of Van Driest (ref. 16) in spite of the fact that Van Driest's theory is for turbulent flow from the leading edge. The Reynolds number at which transition begins and ends on the rays through the vertex varies slightly as seen in figure 27. The center-line ray ($\phi = 0^\circ$) has the highest transition Reynolds number. Hence, the turbulent region is approximately triangular in shape with transition occurring along a line nearly parallel to the leading edge but slightly earlier in the regions far from the vertex. Average local transitional Reynolds numbers for rays off the center line are shown in figure 28 for the several tests at $M_\infty = 6.8$ where transition appeared. The local transitional Reynolds number changes little with angle of attack. The transitional Reynolds number also decreases with a decrease in Reynolds number per inch, a result that has been observed on other configurations.

L
9
2
8

CONCLUSIONS

Results of tests of a variety of delta wings including blunt- and sharp-leading-edge wings, dihedral wings, and wings of 60° and 75° sweep angles at Mach numbers of 6.8 and 9.6 in air and 17.8 in helium have indicated the following conclusions:

1. Spanwise pressure distributions at very low angles of attack are in agreement with boundary-layer-displacement pressures, whereas at high angles of attack the distribution correlates with a cross-flow distribution of pressure.

2. Extreme changes in the flow field over delta wings occur with variation of angle of attack. At low angles of attack there is an inward flow, whereas at high angles of attack the flow is outward from the center of the wing and off the leading edge. The leading edge itself in the sense of airflow direction becomes a trailing edge at high angles of attack.

3. The heat transfer to delta wings has been found to be amenable to simple analytical approaches which take into account the flow pattern peculiar to the angle-of-attack range under consideration.

Langley Research Center,
National Aeronautics and Space Administration,
Langley Air Force Base, Va., March 12, 1962.

REFERENCES

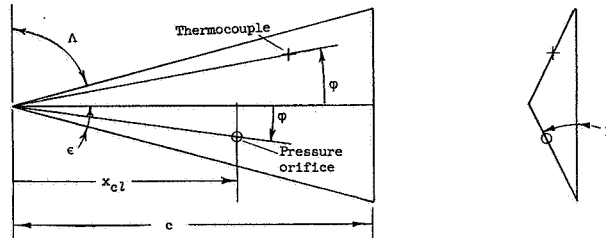
1. Bertram, Mitchel H., Feller, William V., and Dunavant, James C.: Flow Fields, Pressure Distributions, and Heat Transfer for Delta Wings at Hypersonic Speeds. NASA TM X-316, 1960.
2. McLellan, Charles H., Williams, Thomas W., and Bertram, Mitchel H.: Investigation of a Two-Step Nozzle in the Langley 11-Inch Hypersonic Tunnel. NACA TN 2171, 1950.
3. Bertram, Mitchel H.: Exploratory Investigation of Boundary-Layer Transition on a Hollow Cylinder at a Mach Number of 6.9. NACA Rep. 1313, 1957. (Supersedes NACA TN 3546.)
4. Bertram, Mitchel H.: Boundary-Layer Displacement Effects in Air at Mach Numbers of 6.8 and 9.6. NASA TR R-22, 1959. (Supersedes NACA TN 4133.)
5. Armstrong, William O., and Ladson, Charles L. (With Appendix A by Donald L. Baradell and Thomas A. Blackstock): Effects of Variation in Body Orientation and Wing and Body Geometry on Lift-Drag Characteristics of a Series of Wing-Body Combinations at Mach Numbers From 3 to 18. NASA TM X-73, 1959.
6. Henderson, Arthur, Jr., and Baradell, Donald L.: Recent Work at Langley Research Center in the Development of Hypersonic Helium Tunnels. Proc. Nat. Symposium on Hypervelocity Techniques, Inst. Aero. Sci., Oct. 1960, pp. 131-141.
7. Monaghan, R. J.: An Approximate Solution of the Compressible Laminar Boundary Layer on a Flat Plate. R. & M. No. 2760, British A.R.C., 1956.
8. Bertram, Mitchel H., and Henderson, Arthur, Jr.: Recent Hypersonic Studies of Wings and Bodies. ARS Jour., vol. 31, no. 8, Aug. 1961, pp. 1129-1139.
9. Fluid Motion Panel of the Aeronautical Research Committee and Others: Modern Developments in Fluid Dynamics. Vol. II., S. Goldstein, ed., The Clarendon Press (Oxford), 1938, p. 631.
10. Sibulkin, M.: Heat Transfer Near the Forward Stagnation Point of a Body of Revolution. Jour. Aero. Sci. (Readers' Forum), vol. 19, no. 8, Aug. 1952, pp. 570-571.
11. Pai, Shih-I: Viscous Flow Theory. I - Laminar Flow. D. Van Nostrand Co., Inc., c.1956, pp. 262-264.

12. Vaglio-Laurin, Roberto: Laminar Heat Transfer on Blunt-Nosed Bodies in Three-Dimensional Hypersonic Flow. WADC Tech. Note 58-147, ASTIA Doc. No. AD 155 588, U.S. Air Force, May 1958.
13. Lees, Lester: Laminar Heat Transfer Over Blunt-Nosed Bodies at Hypersonic Flight Speeds. Jet Propulsion, vol. 26, no. 4, Apr. 1956, pp. 259-269, 274.
14. Bertram, Mitchel H., and Feller, William V.: A Simple Method for Determining Heat Transfer, Skin Friction, and Boundary-Layer Thickness for Hypersonic Laminar Boundary-Layer Flows in a Pressure Gradient. NASA MEMO 5-24-59L, 1959.
15. Bertram, Mitchel H., and Blackstock, Thomas A.: Some Simple Solutions to the Problem of Predicting Boundary-Layer Self-Induced Pressures. NASA TN D-798, 1961.
16. Van Driest, E. R.: The Problem of Aerodynamic Heating. Aero. Eng. Rev., vol. 15, no. 10, Oct. 1956, pp. 26-41.

L
9
2
8

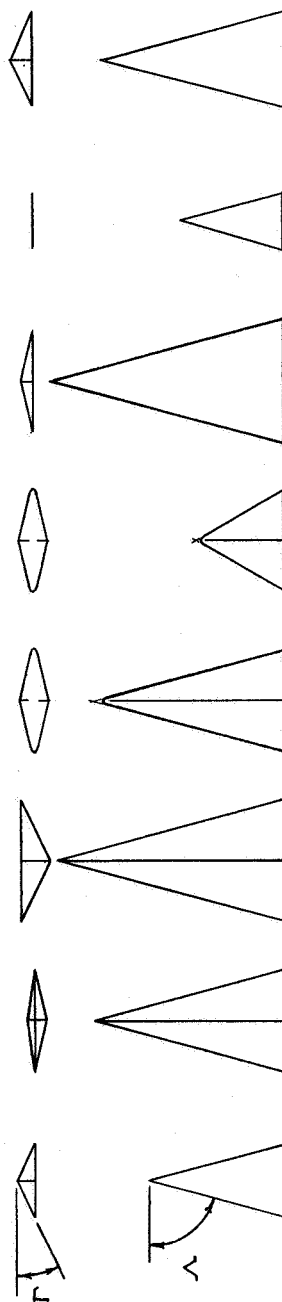


TABLE I.- THERMOCOUPLE AND PRESSURE-ORIFICE LOCATIONS

Note: ϕ is measured in the plane of the instrumented surface

Thermocouple	Model I		Model II		Model III		Model IV		Model V		Model VI		Model VII	
	x_{cl} , in.	ϕ , deg	x_{cl} , in.	ϕ , deg	x_{cl} , in.	ϕ , deg	x_{cl} , in.	ϕ , deg	x_{cl} , in.	ϕ , deg	x_{cl} , in.	ϕ , deg	x_{cl} , in.	ϕ , deg
1	1.50	0	2.90	0	2.00	0	2.90	1.8	2.40	0	3.50	0	0.50	0
2	2.00	0	2.90	1.0	3.00	12.0	5.17	0	3.50	0	4.00	4.0	.75	0
3	2.00	6.0	2.90	3.8	4.00	0	4.90	2.0	1.00	3.8	4.00	8.0	1.00	0
4	3.00	0	2.90	6.9	4.00	6.0	5.90	2.0	1.40	4.0	4.50	0	1.25	0
5	3.00	3.0	3.65	4.4	4.00	12.0	6.90	2.0	3.10	4.0	5.00	2.0	1.50	0
6	3.00	6.0	3.65	7.8	5.00	6.0	7.90	2.0	3.50	4.0	5.00	6.0	1.50	9.5
7	3.00	9.0	4.40	0	5.00	12.0	1.40	8.3	.60	12.5	5.00	10.0	2.50	0
8	4.00	0	4.40	1.2	6.00	0	1.90	6.6	1.40	12.5	5.50	0	2.50	5.7
9	4.00	3.0	4.40	2.8	6.00	6.0	2.90	6.7	1.90	12.8	6.00	2.0	2.50	9.1
10	4.00	6.0	4.40	5.0	6.00	12.0	5.90	4.5	2.40	12.5	6.00	6.0	2.50	11.3
11	4.00	9.0	4.40	6.5	7.00	4.0	4.90	7.2	1.00	17.5	6.00	10.0	2.75	0
12	4.50	9.0	4.40	8.0	7.00	8.0	5.90	7.2	1.90	17.7	6.50	0	2.75	4.2
13	4.50	12.0	4.40	9.8	7.00	12.0	6.90	5.4	2.40	17.7	6.50	4.0	3.00	0
14	5.25	0	5.40	5.1	7.00	15.0	7.90	5.6	3.10	17.7	6.50	8.0	3.25	0
15	5.25	3.0	5.40	6.7	8.00	2.0	7.90	7.2	.60	24.8	7.00	2.0	3.25	2.9
16	5.25	6.0	5.40	10.3	8.00	6.0	6.90	8.4	1.40	24.8	7.00	6.0	3.25	8.7
17	5.25	9.0	6.40	0	8.00	10.0	7.90	8.6	1.90	24.8	7.00	10.0	3.25	4.4
18	5.25	12.0	6.40	1.0	8.00	14.0	1.90	11.9	2.40	24.8	7.50	0	3.25	12.9
19			6.40	2.0	8.50	0	2.90	11.7	3.10	24.8	7.50	4.0	3.50	0
20			6.40	5.1	8.50	4.0	7.40	0	3.50	24.9	7.50	8.0	3.50	5.4
21			6.40	5.1	8.50	8.0	4.90	12.3	0.40	31.4	8.00	2.0	3.75	0
22			6.40	6.9	8.50	12.0	5.90	10.4	1.40	31.4	8.00	6.0	3.75	9.6
23			6.40	10.4	9.00	2.0	5.90	12.4	2.40	31.4	8.00	10.0	4.00	0
24			7.40	2.0	9.00	6.0	7.90	12.1	2.60	31.4	8.50	0	4.00	11.4
25			7.40	3.3	9.00	10.0	1.90	15.4	3.50	31.4	9.00	2.0	4.25	0
26			7.40	5.3	9.00	12.0	2.90	15.4	2.72	6.5	9.00	4.0	4.25	3.5
27			7.40	7.1	9.00	14.0	5.90	15.4	3.10	11.9	9.00	6.0	4.25	6.7
28			7.40	8.8	9.00	15.0	7.90	15.4	3.50	22.9	9.00	8.0	4.25	9.9
29			7.40	10.6			7.90				9.00	10.0	4.25	12.9
30			7.40	12.3							9.00	12.0		

Pressure orifice	Model I		Model II		Model III		Model IV		Model V		Model VI		Model VII		Model VIII	
	x_{cl} , in.	ϕ , deg	x_{cl} , in.	ϕ , deg	x_{cl} , in.	ϕ , deg	x_{cl} , in.	ϕ , deg	x_{cl} , in.	ϕ , deg	x_{cl} , in.	ϕ , deg	x_{cl} , in.	ϕ , deg	x_{cl} , in.	ϕ , deg
1	2.50	0	3.40	0	3.00	0	1.90	2.1	1.00	3.8	3.00	0	0.50	0	0.80	0
2	3.00	6.0	5.40	0	4.00	8.0	2.90	2.0	1.40	4.0	4.00	6.0	1.00	0	1.60	0
3	3.50	0	7.40	0	5.00	0	4.90	2.1	2.40	4.0	5.00	8.0	1.50	0	2.40	0
4	3.50	9.0	4.40	3.2	5.00	12.0	5.90	2.1	3.10	4.0	6.50	10.0	2.00	0	2.40	4.8
5	4.50	0	5.40	3.0	7.00	0	7.90	2.1	3.50	4.0	9.25	0	2.00	6.6	2.40	9.4
6	4.50	6.0	6.40	3.2	7.00	6.0	2.90	6.7	.60	12.5	9.25	2.0	2.25	12.5	2.40	11.8
7	4.50	10.5	7.40	3.3	7.00	12.0	4.90	6.8	1.40	12.5	9.25	4.0	2.50	0	3.20	0
8	5.50	0	3.40	5.8	9.00	0	5.90	6.8	3.10	11.9	9.25	6.0	2.50	5.7	4.00	0
9	5.50	3.0	5.40	6.5	9.00	4.0	6.90	6.7	3.50	8.5	9.25	8.0	2.50	11.3	4.00	4.3
10	5.50	6.0	7.40	6.8	9.00	8.0	7.90	6.7	1.00	17.5	9.25	10.0	3.00	0	4.00	8.5
11	5.50	9.0	4.40	8.2	9.00	12.0	1.90	9.9	1.40	25.1	9.25	12.0	3.30	3.8	4.00	12.7
12	5.50	12.0	6.40	8.4	9.00	14.0	2.90	9.7	2.40	17.9			3.30	8.6	4.00	13.3
13			7.40	8.6			6.90	9.4	3.10	17.8			3.30	12.8	4.80	0
14			5.40	10.2			7.90	8.8	2.40	27.8			3.50	0	5.60	0
15			7.40	10.6			4.90	12.0	3.10	24.2			3.58	7.1	6.40	0
16							5.90	12.0	3.50	21.7			3.84	9.9	6.40	2.7
17							6.90	12.0	3.50	24.4			3.92	0	6.40	5.4
18							7.90	12.0	3.50	28.2			4.10	12.2	6.40	8.0
19													4.35	0	6.40	10.6
20													4.35	4.6	6.40	13.2
21													4.35	9.1	6.40	14.0
22													4.35	14.2	7.20	0



	Model I	Model II	Model III	Model IV	Model V	Model VI	Model VII	Model VIII
Sweep, deg	75	75	75	75	60	75	75	75
Chord to vertex, in.	6.0	8.4	10.0	8.4	3.9	10.25	4.5	8
Dihedral (instrumented ¹ surface), deg	0	13	26	13	13	0	0	0
Dihedral (uninstrumented surface), deg	25	8	0	13	13	13	-----	25
Leading-edge radius, in.	0.001 to 0.002	0.001 to 0.002	0.001 to 0.002	0.100	0.100	0.001 to 0.002	Square	0.001 to 0.002
Nominal skin thickness, in.	0.031	0.031	0.031	0.030	0.030	0.050	0.080	Solid
Plan-view nose radius, in.	-----	-----	-----	0.200	0.200	-----	-----	-----

Figure 1.- Delta-wing models.

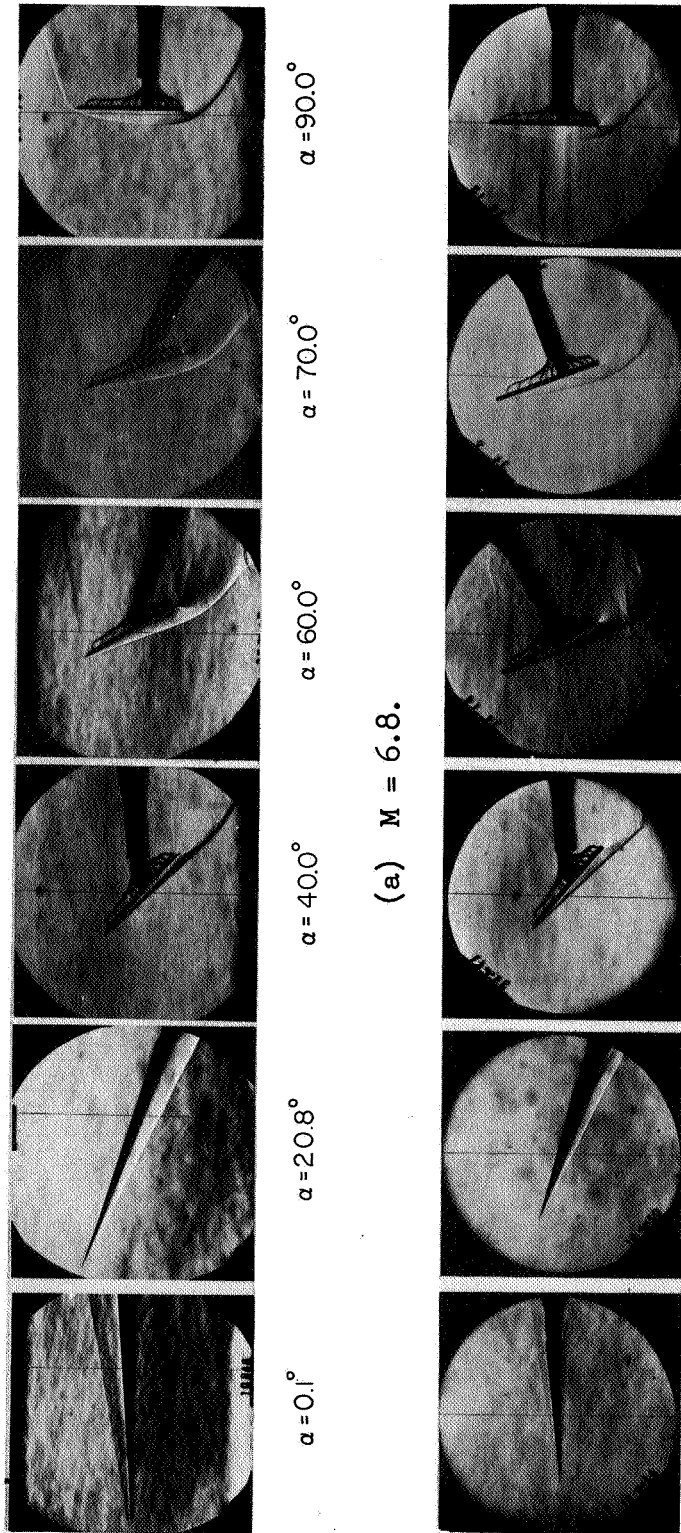
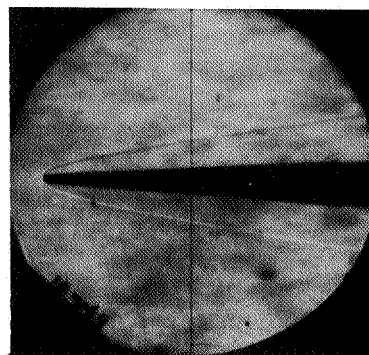
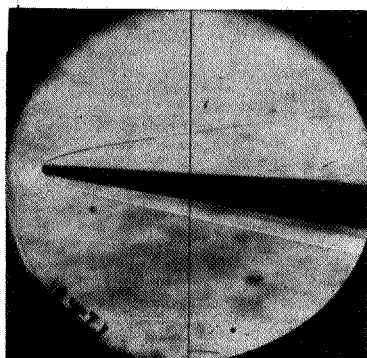
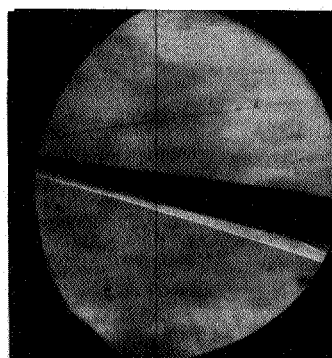
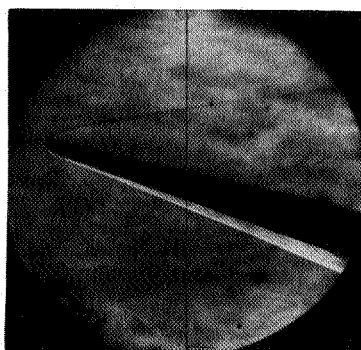


Figure 2.- Side-view schlieren photographs of flat, sharp-leading-edge, 75° swept delta-wing models.

(a) $M = 6.8$.

(b) $M = 9.6$.

L-62-47

(a) $\alpha' = -1.0^\circ$.(b) $\alpha' = 4.0^\circ$.(c) $\alpha' = 9.0^\circ$.(d) $\alpha' = 14.2^\circ$.(e) $\alpha' = 18.9^\circ$.(f) $\alpha' = 29.9^\circ$.

L-62-48

Figure 3.- Side-view schlieren photographs of blunt-leading-edge, 75° swept delta-wing model IV at $M_\infty = 9.6$.

CONFIDENTIAL

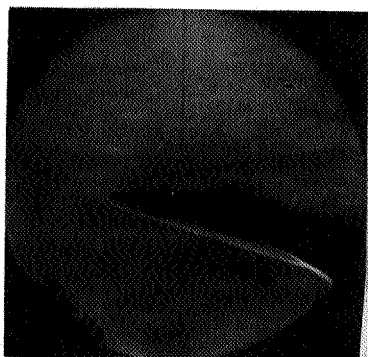
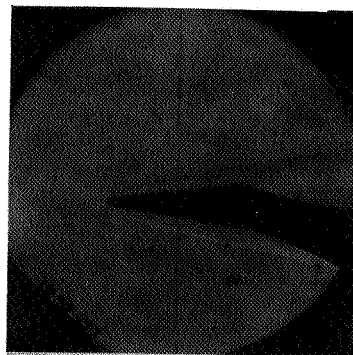
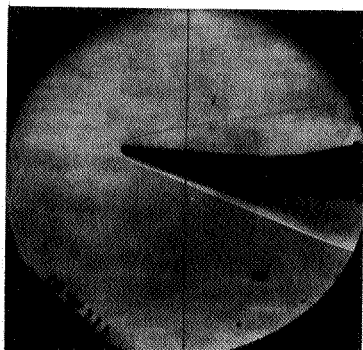
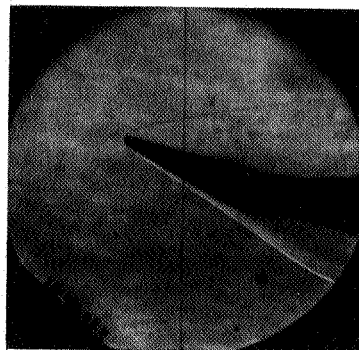
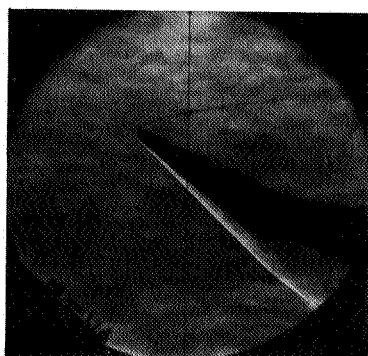
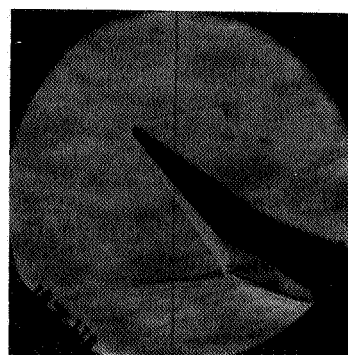
(a) $\alpha' = 1.1^\circ$.(b) $\alpha' = 6.8^\circ$.(c) $\alpha' = 16.6^\circ$.(d) $\alpha' = 28.4^\circ$.(e) $\alpha' = 38.0^\circ$.(f) $\alpha' = 47.5^\circ$.

Figure 4.- Side-view schlieren photographs of blunt-leading-edge, 60° swept delta-wing model V at $M_\infty = 9.6$. L-62-49

CONFIDENTIAL

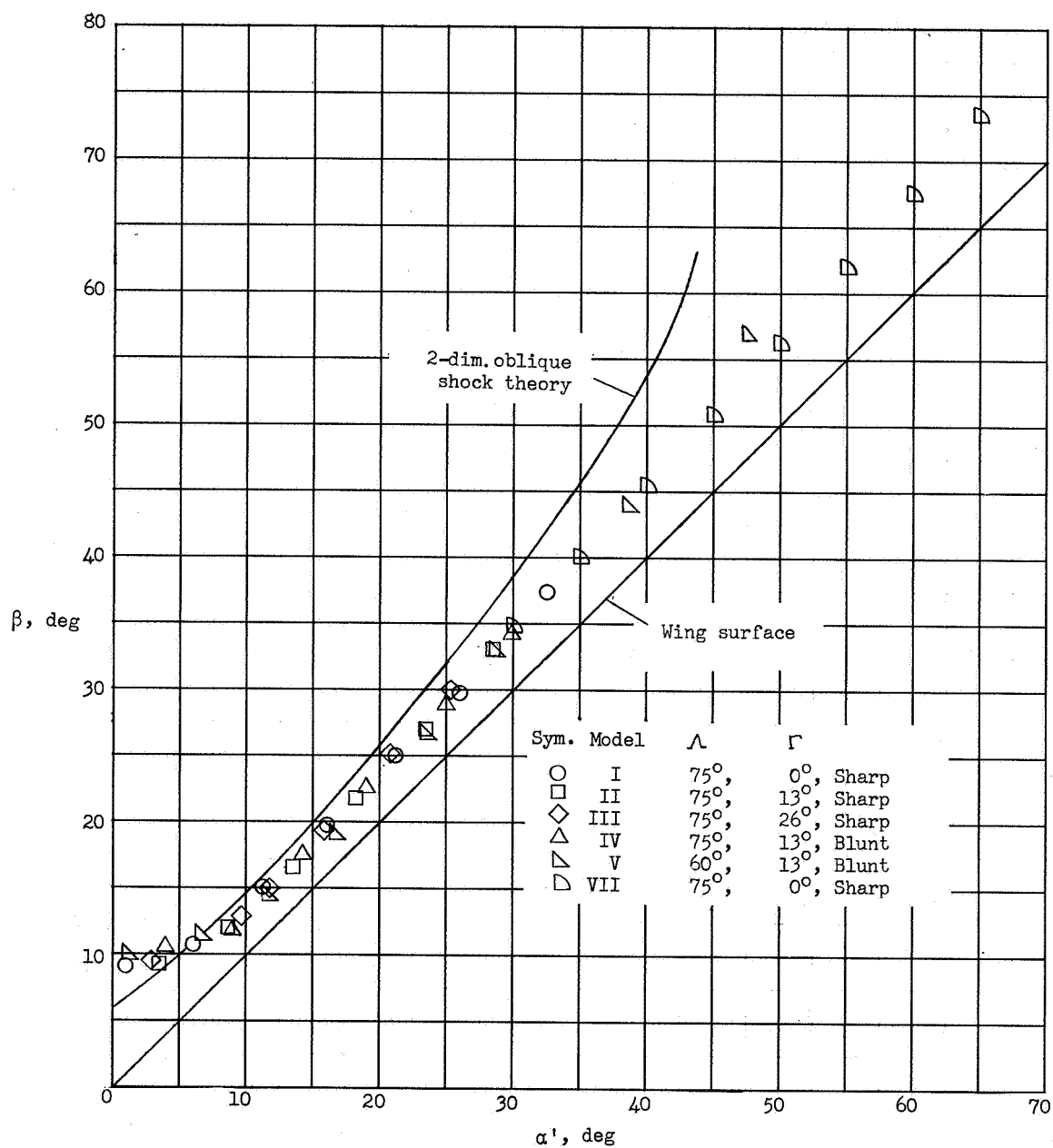
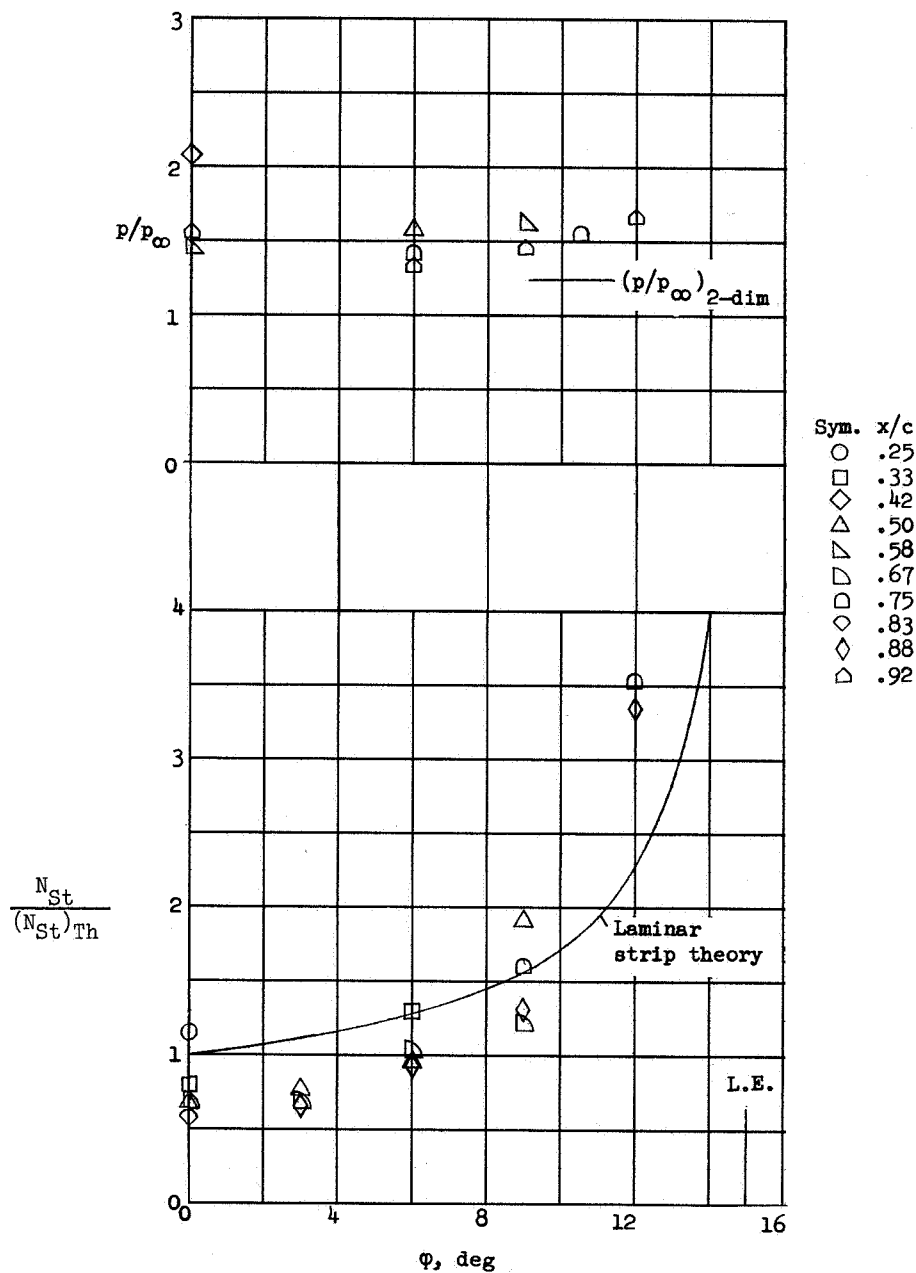
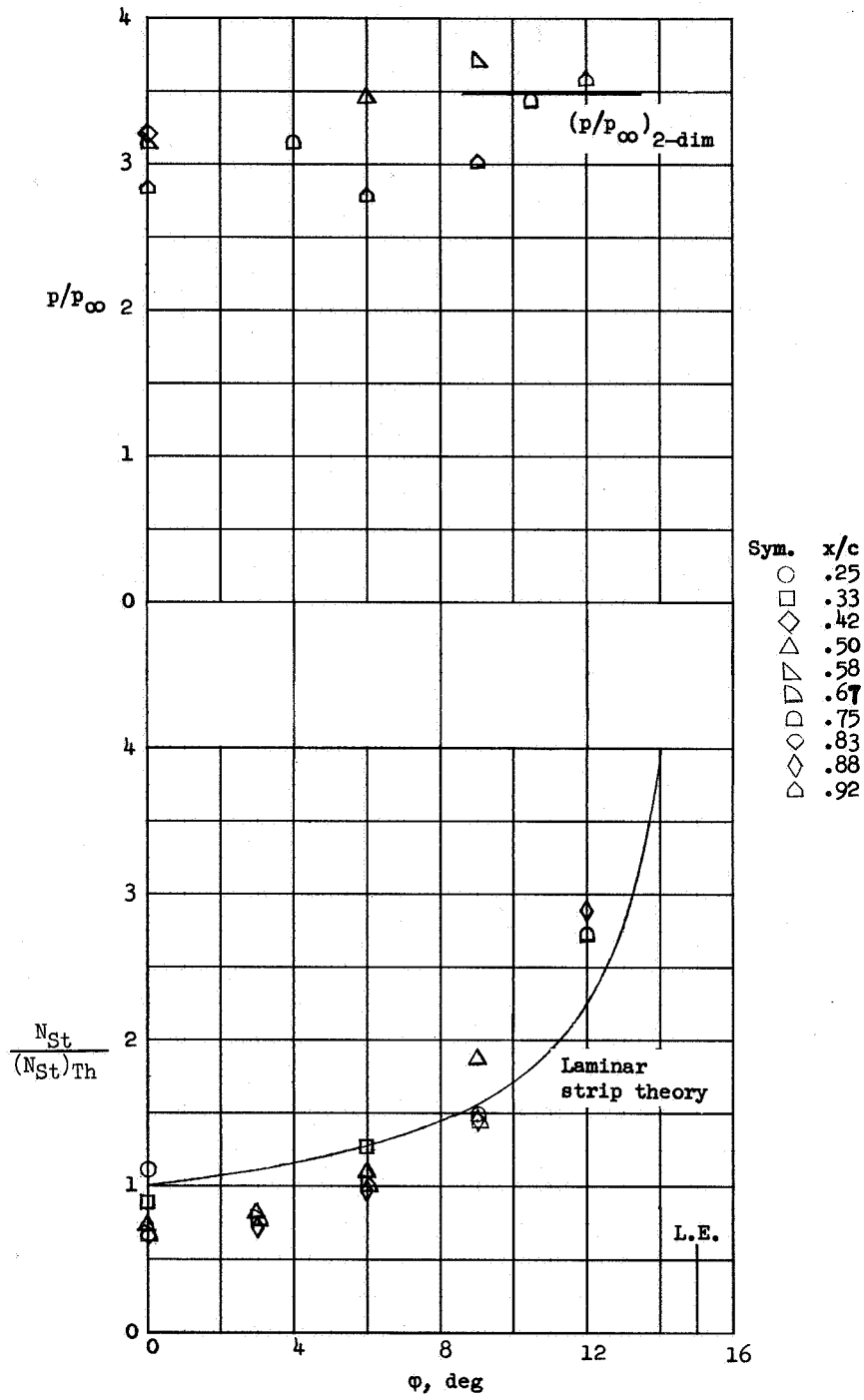


Figure 5.- Shock-wave-angle correlation for delta-wing models. $M_\infty = 9.6$.



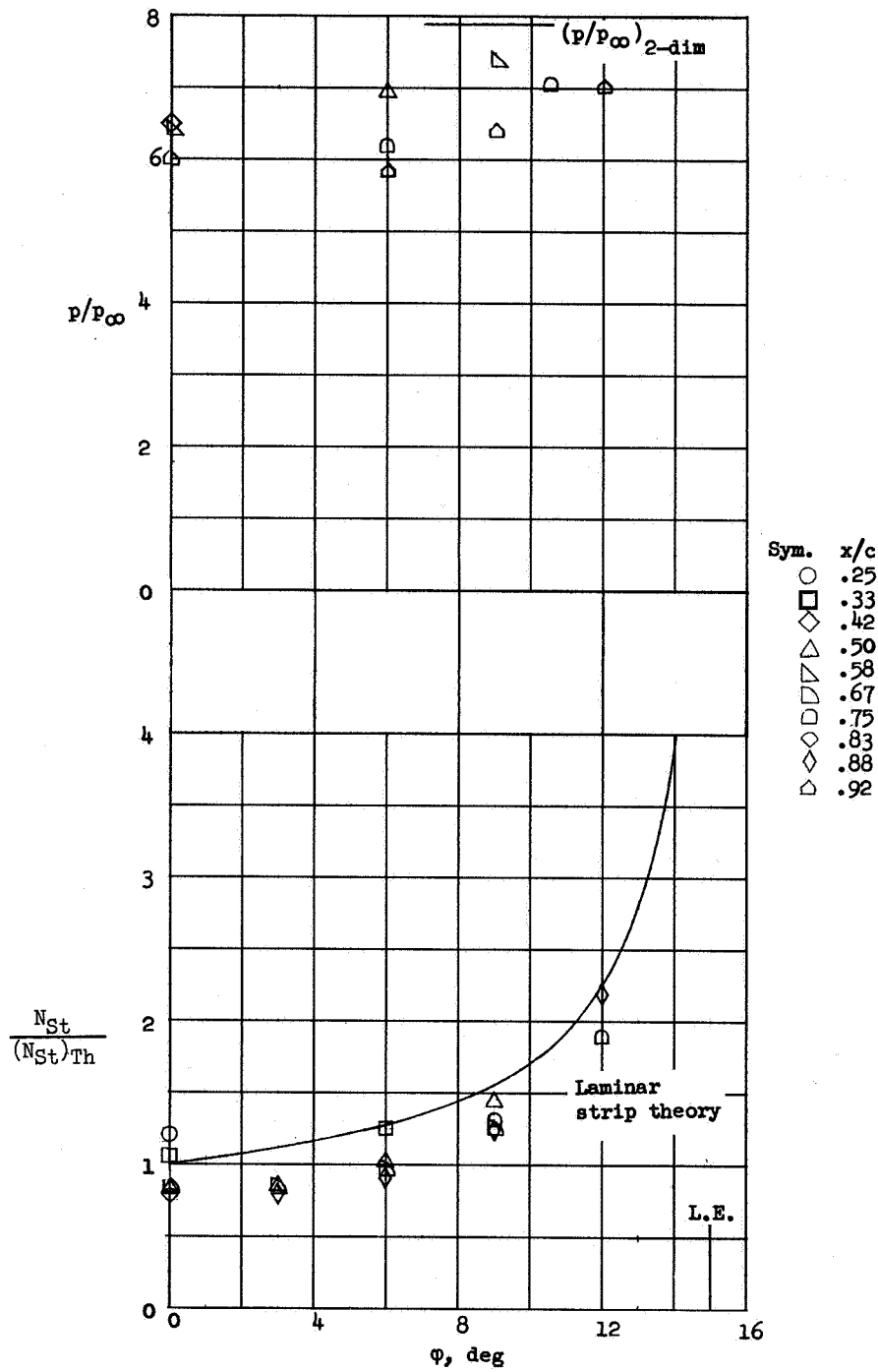
(a) $\alpha = 1.0^\circ$.

Figure 6.- Spanwise distribution of pressure and ratio of heating to theoretical laminar heating on center line for strip theory. Delta-wing model I ($\Lambda = 75^\circ$, $\Gamma = 0^\circ$, sharp leading edge) at $M_\infty = 9.6$ and $R_c = 0.6 \times 10^6$.



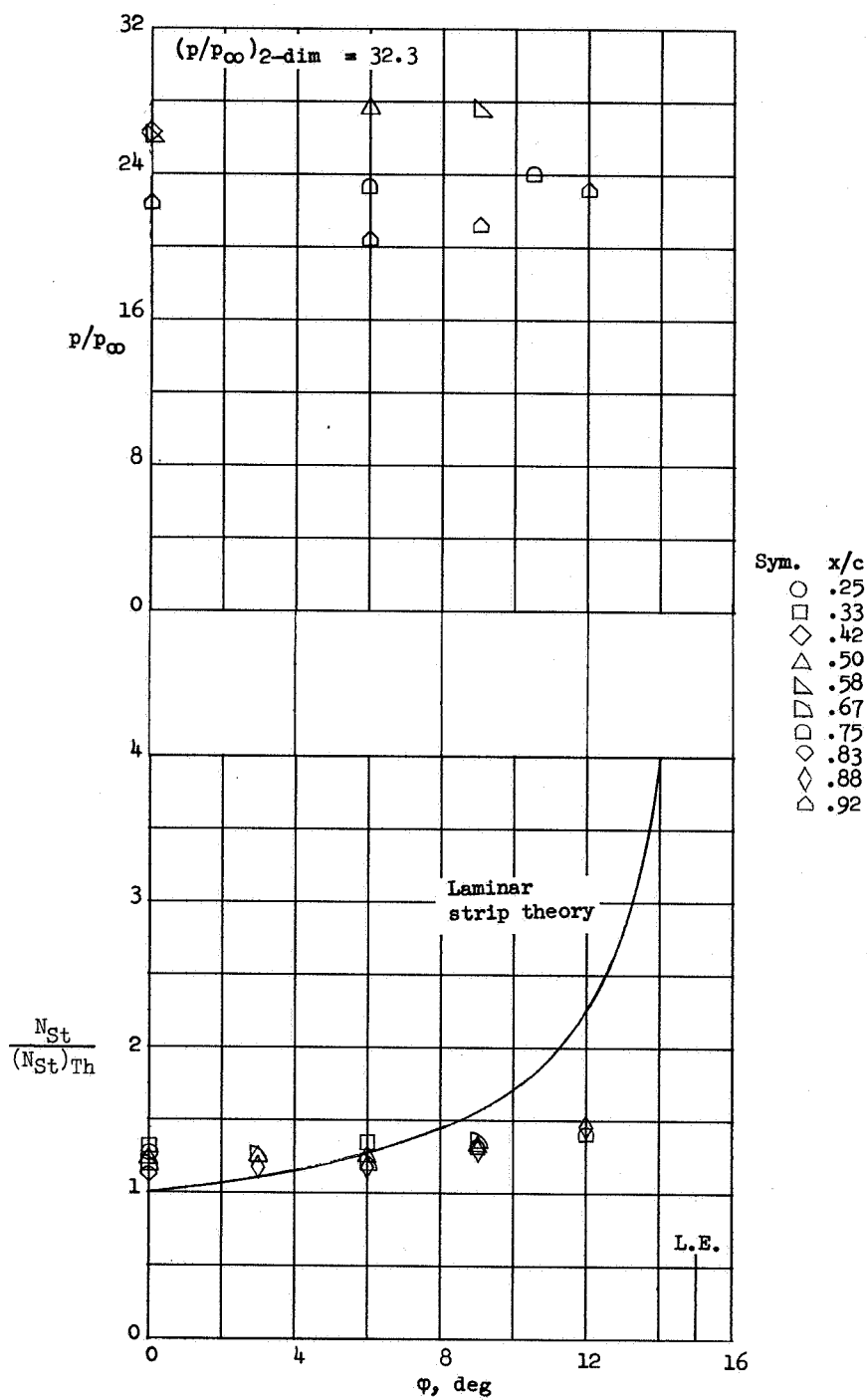
(b) $\alpha = 6.0^\circ$.

Figure 6.- Continued.



(c) $\alpha = 11.2^\circ$.

Figure 6.- Continued.



(d) $\alpha = 26.0^\circ$.

Figure 6.- Concluded.

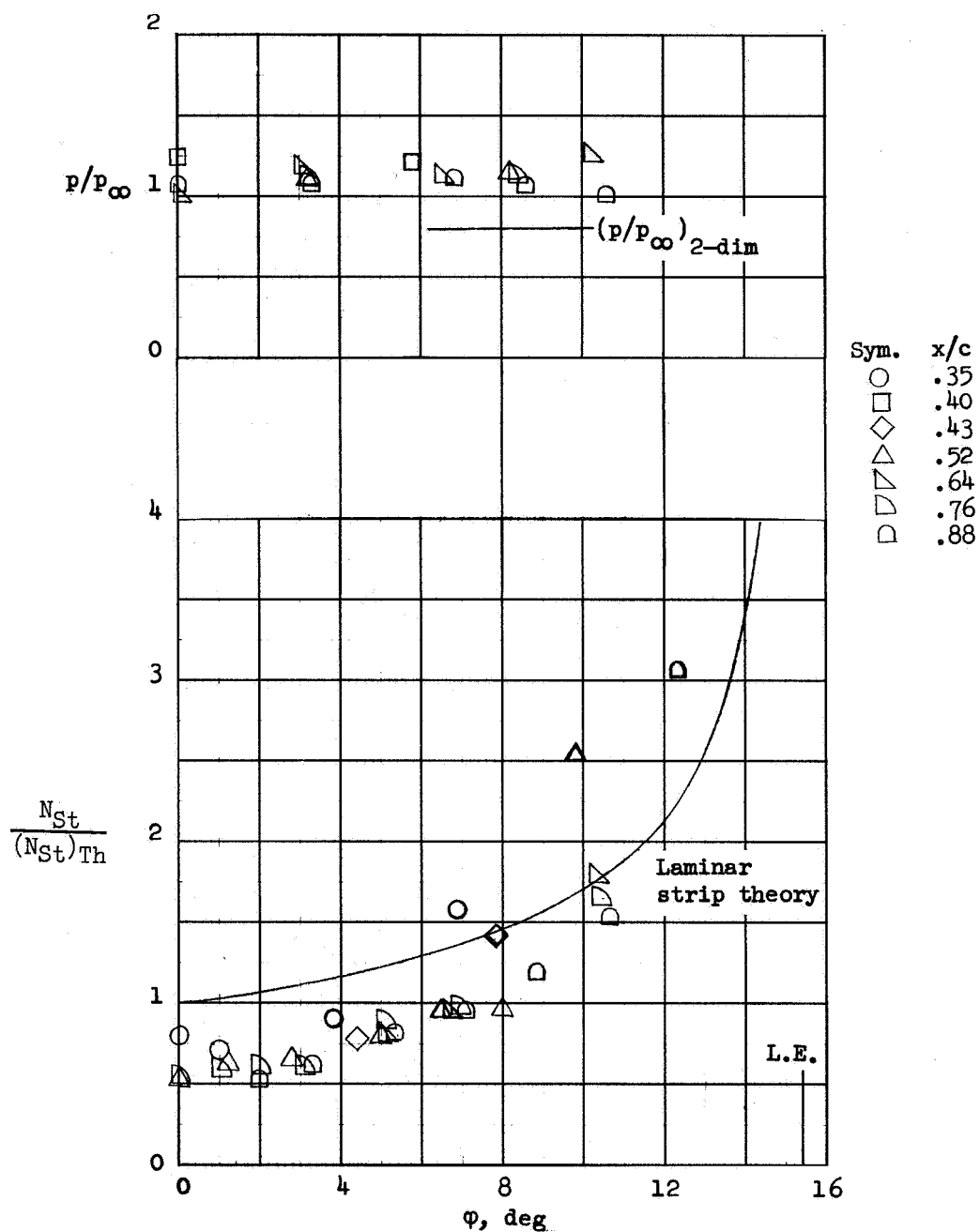
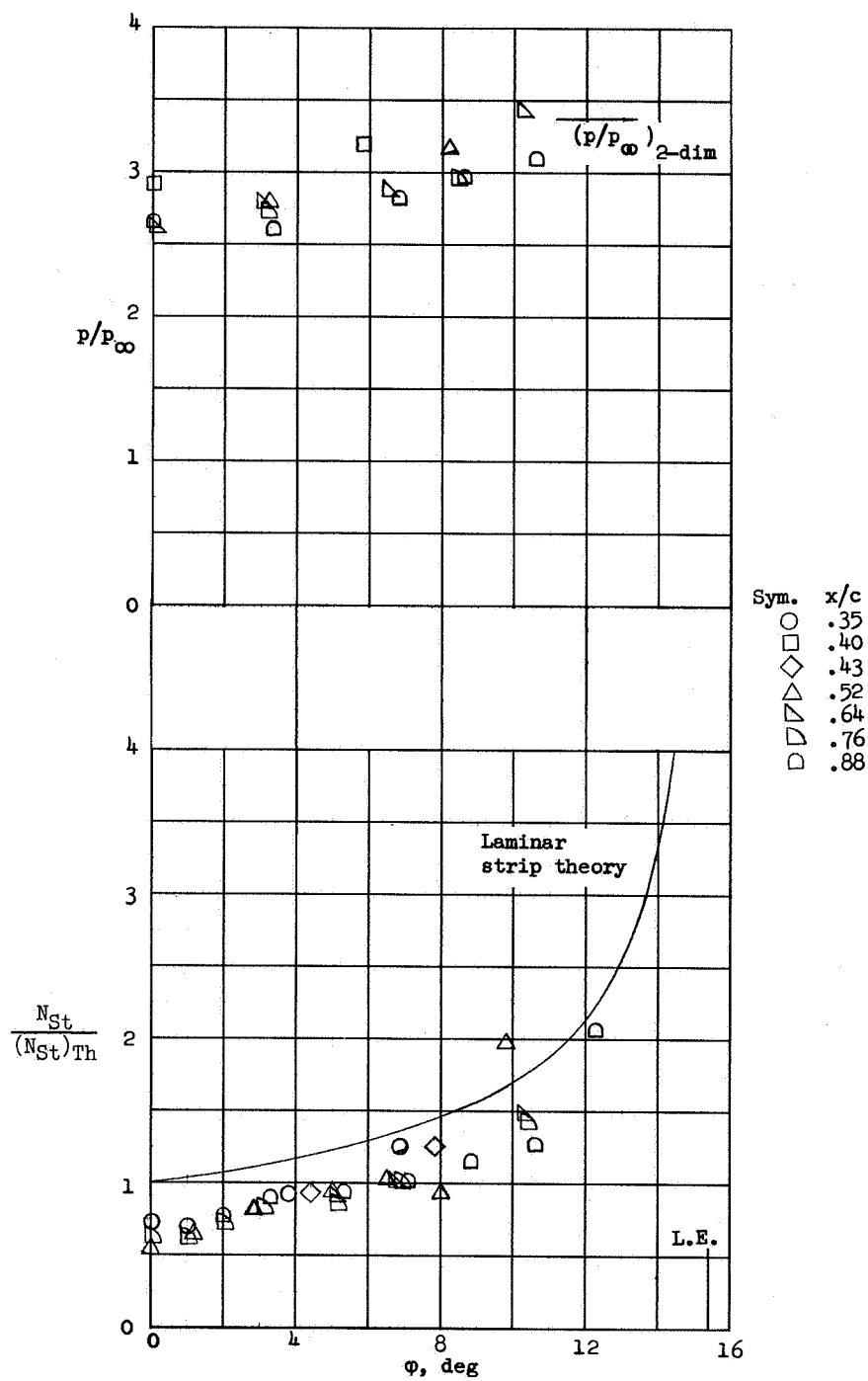
(a) $\alpha' = -1.0^\circ$.

Figure 7.- Spanwise distribution of pressure and ratio of heating to theoretical laminar heating on center line for strip theory. Delta-wing model II ($\Lambda = 75^\circ$, $\Gamma = 13^\circ$, sharp leading edge) at $M_\infty = 9.6$ and $R_c = 0.8 \times 10^6$.

[REDACTED]

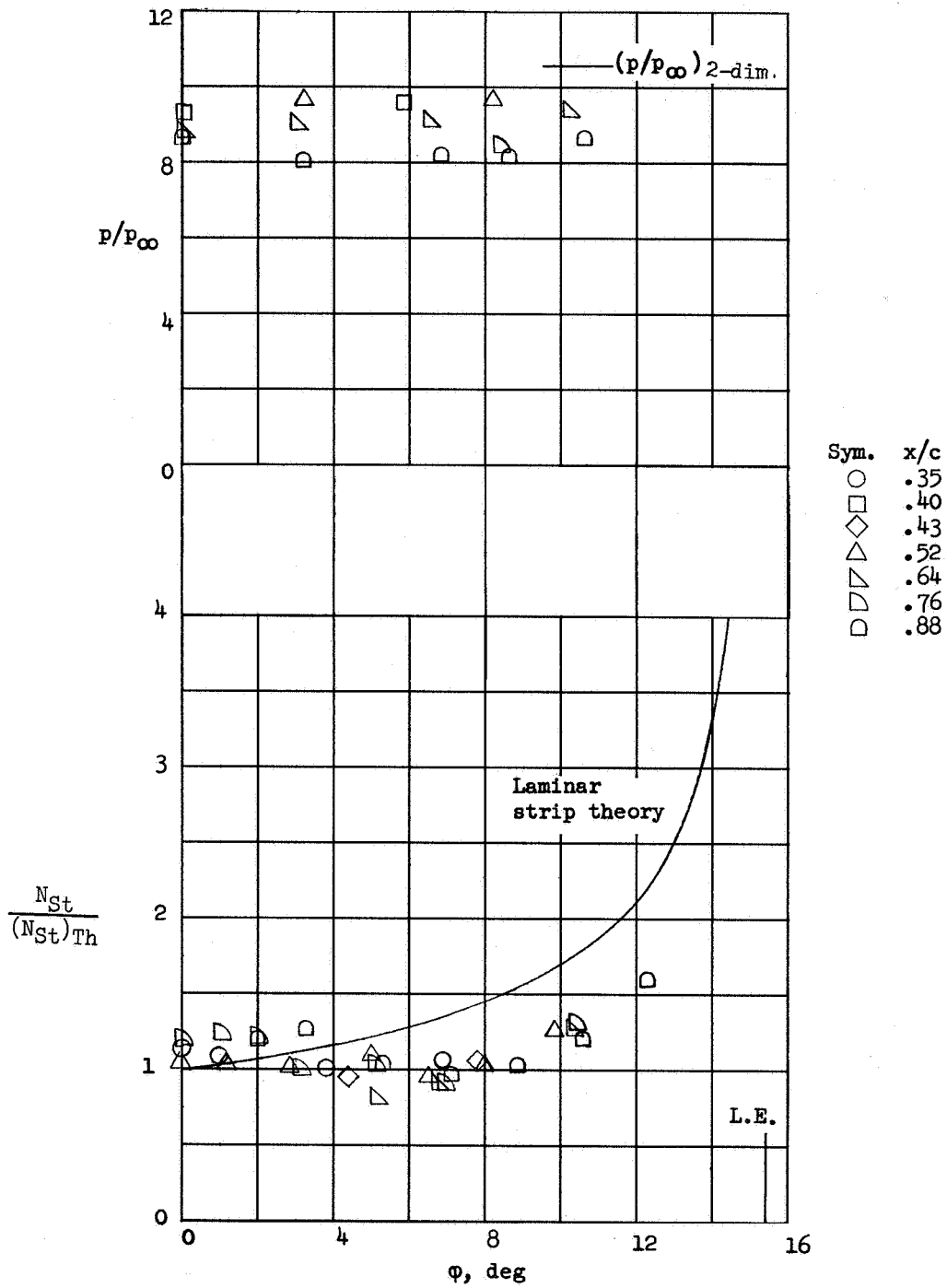
L-928



(b) $\alpha' = 5.8^\circ$.

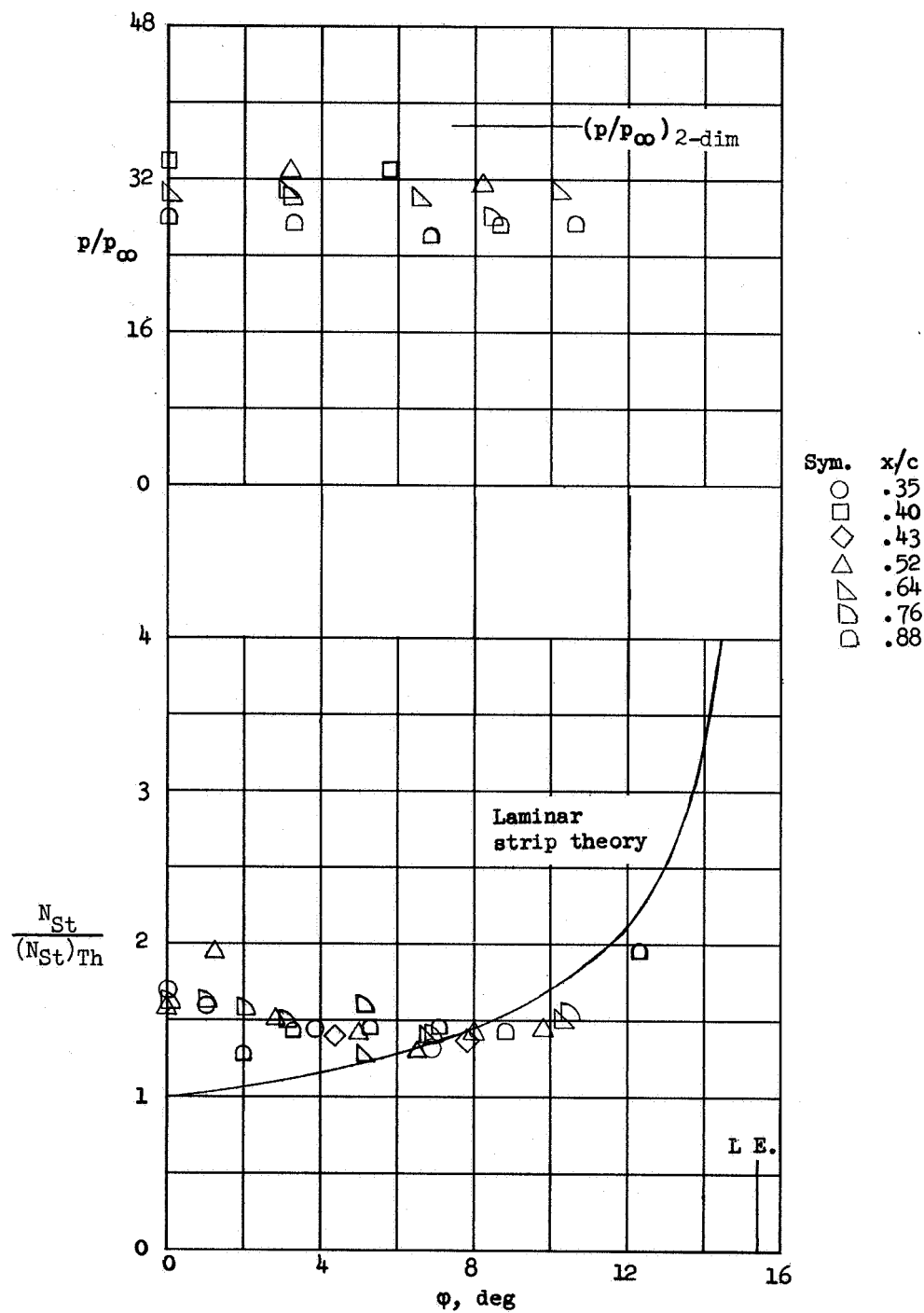
Figure 7.- Continued.

[REDACTED]



(c) $\alpha' = 13.5^\circ$.

Figure 7.- Continued.



(d) $\alpha' = 28.5^\circ$.

Figure 7.- Concluded.

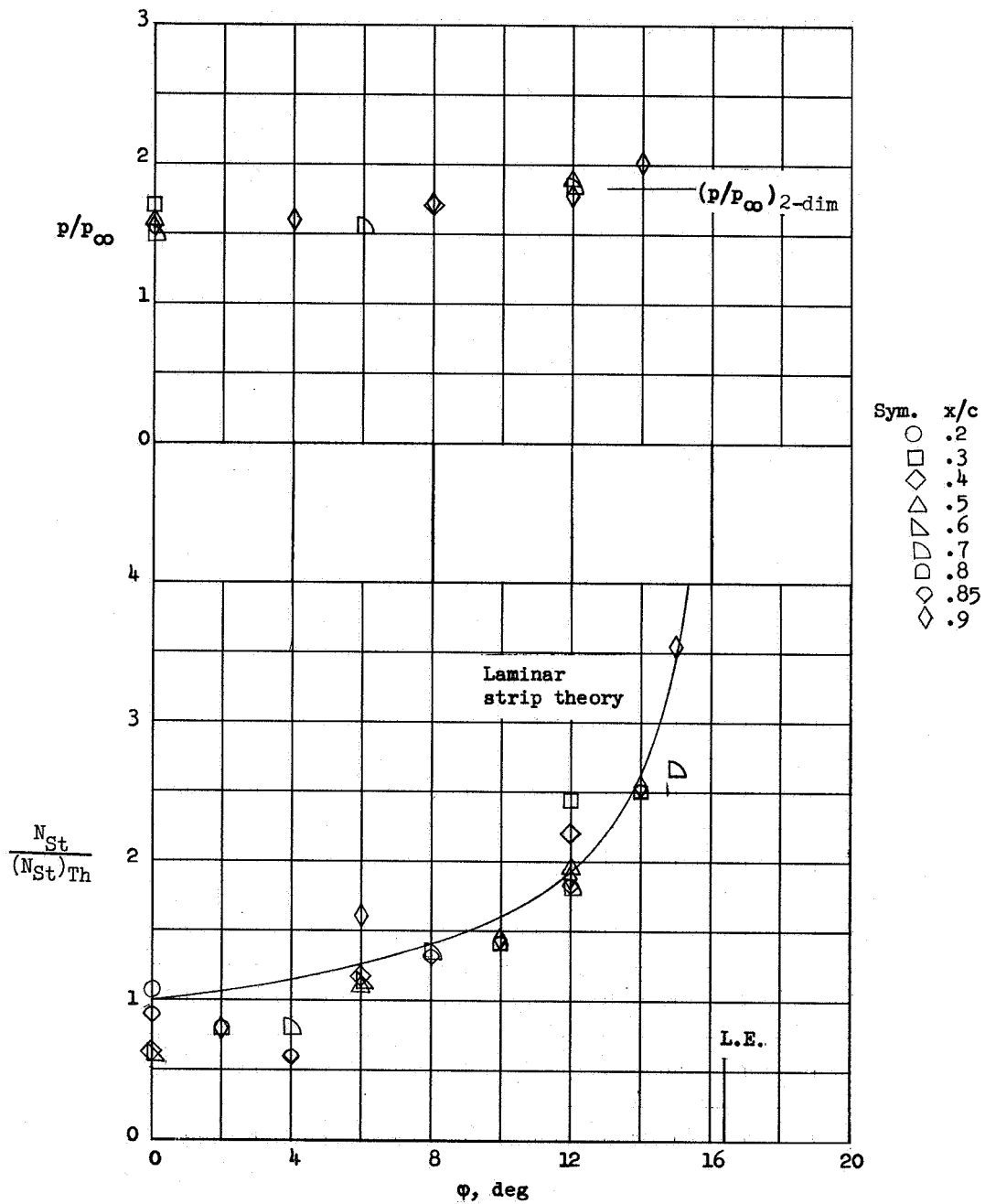
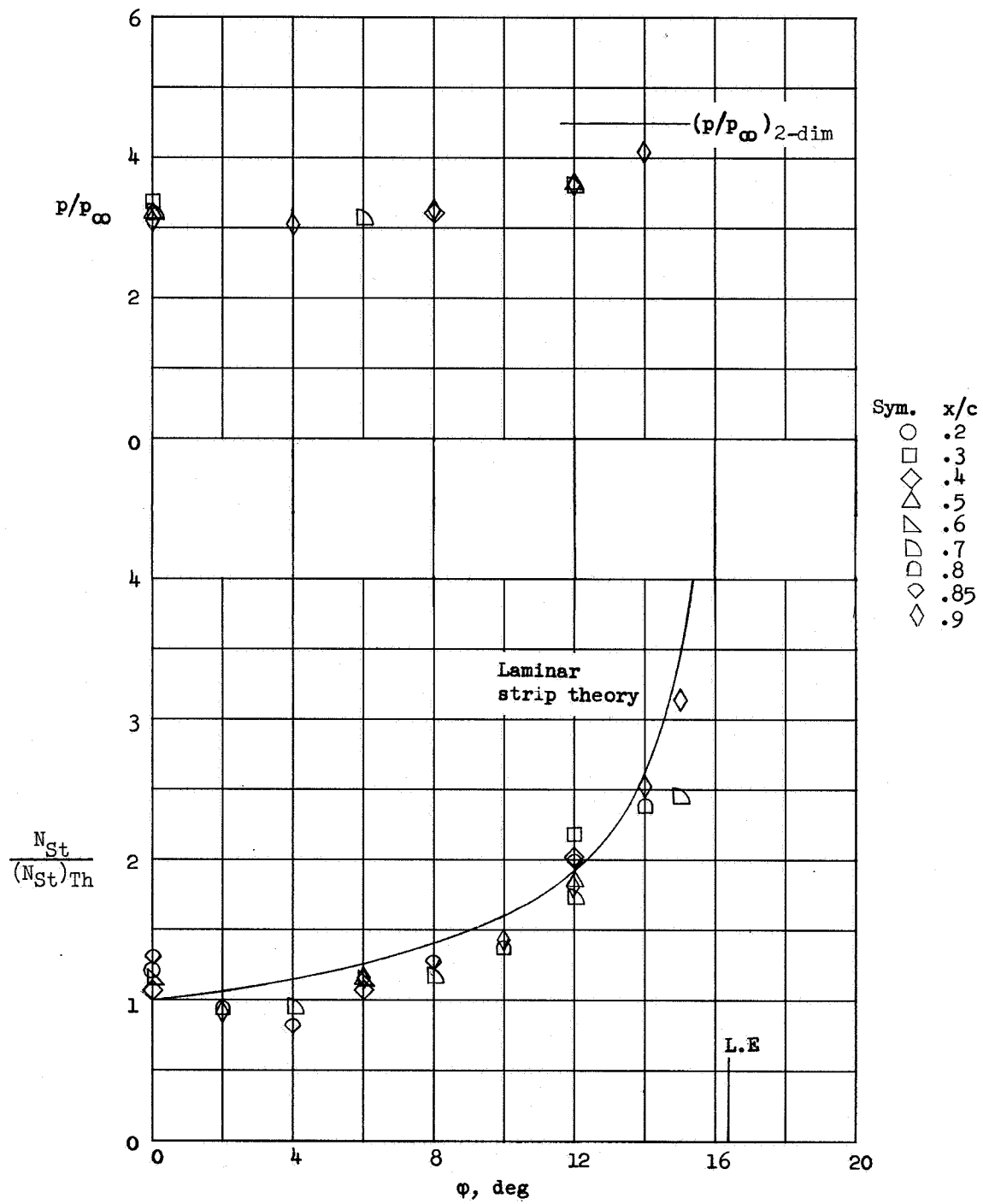
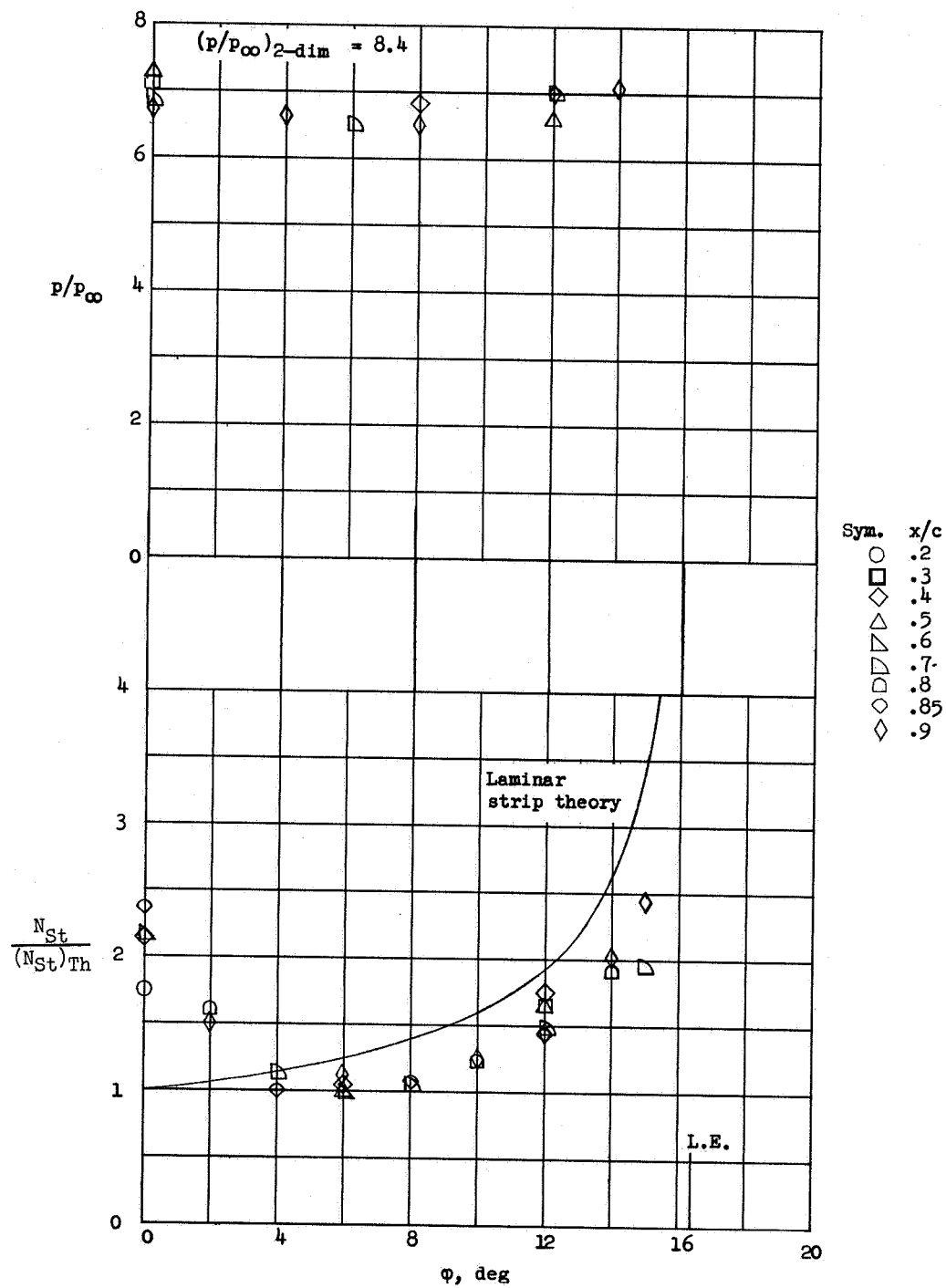
(a) $\alpha' = 2.7^\circ$.

Figure 8.- Spanwise distribution of pressure and ratio of heating to theoretical laminar heating on center line for strip theory. Delta-wing model III ($\Lambda = 75^\circ$, $\Gamma = 26^\circ$, sharp leading edge) at $M_\infty = 9.6$ and $R_c = 1 \times 10^6$.



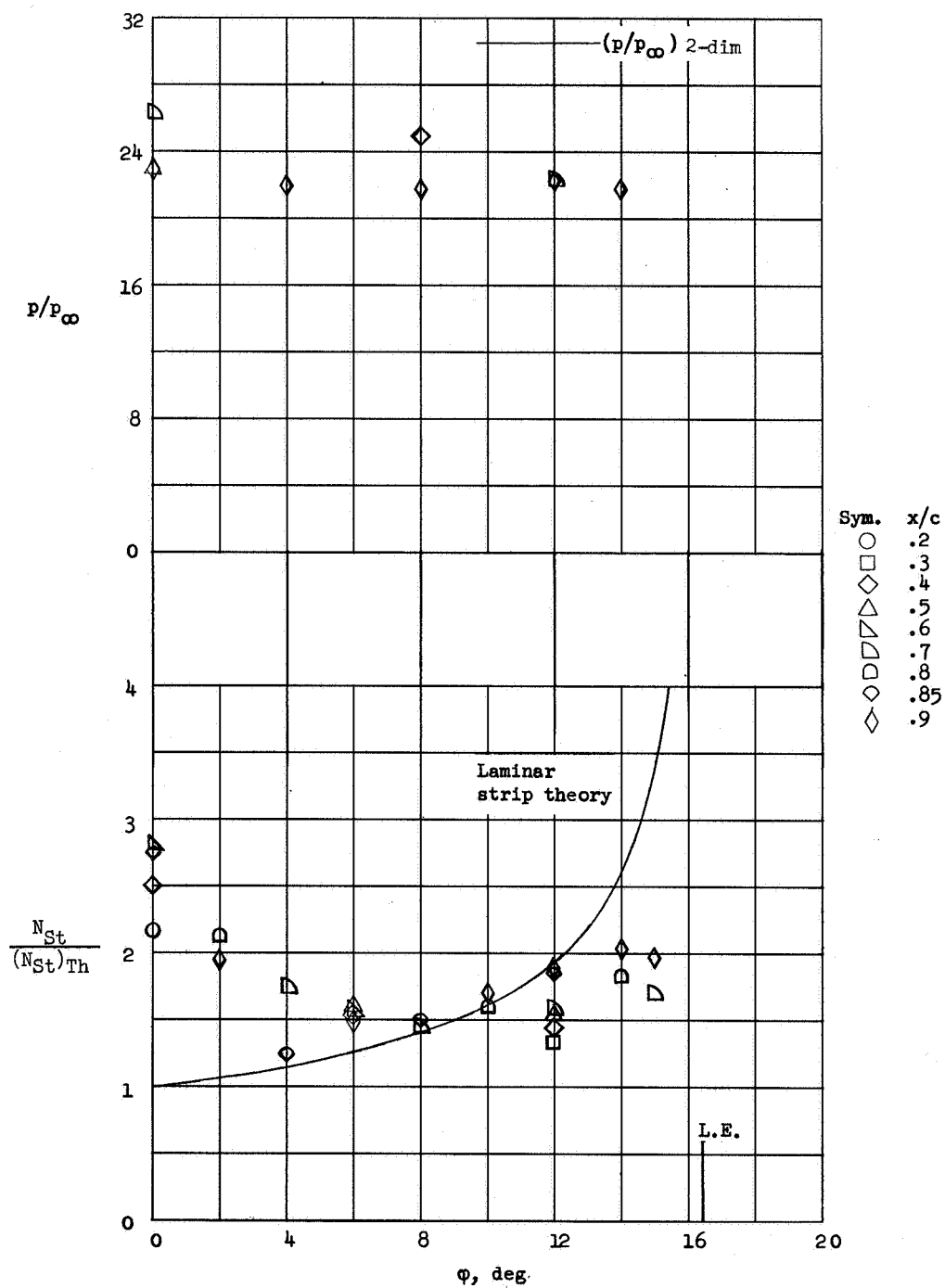
(b) $\alpha' = 7.3^\circ$.

Figure 8.- Continued.



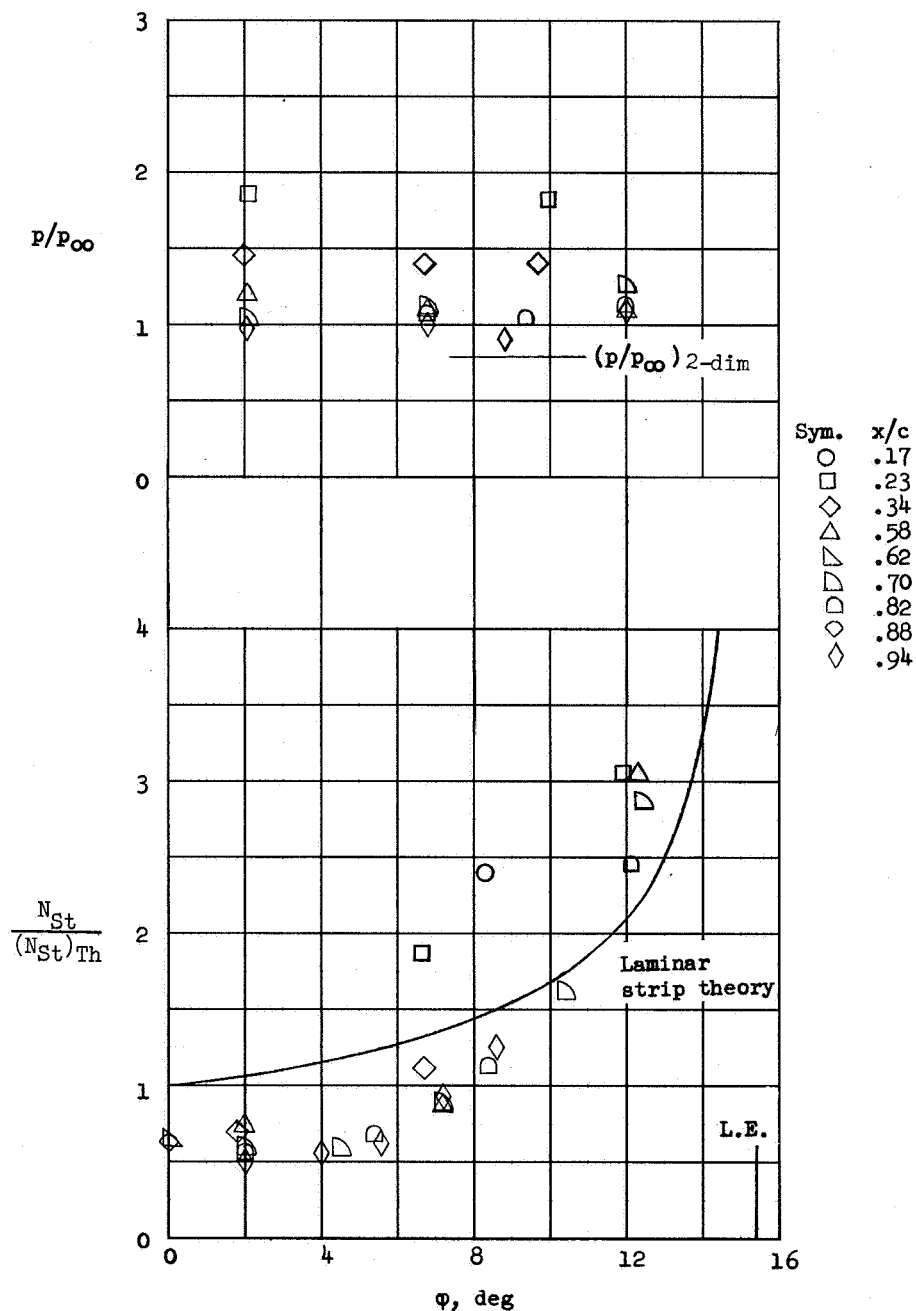
(c) $\alpha' = 11.7^\circ$.

Figure 8.- Continued.



(d) $\alpha' = 25.2^\circ$.

Figure 8.- Concluded.



(a) $\alpha' = -1.0^\circ$.

Figure 9.- Spanwise distribution of pressure and ratio of heating to theoretical laminar heating on center line for strip theory. Delta-wing model IV ($\Lambda = 75^\circ$, $\Gamma = 13^\circ$, blunt leading edge) at $M_\infty = 9.6$ and $R_c = 0.8 \times 10^6$.

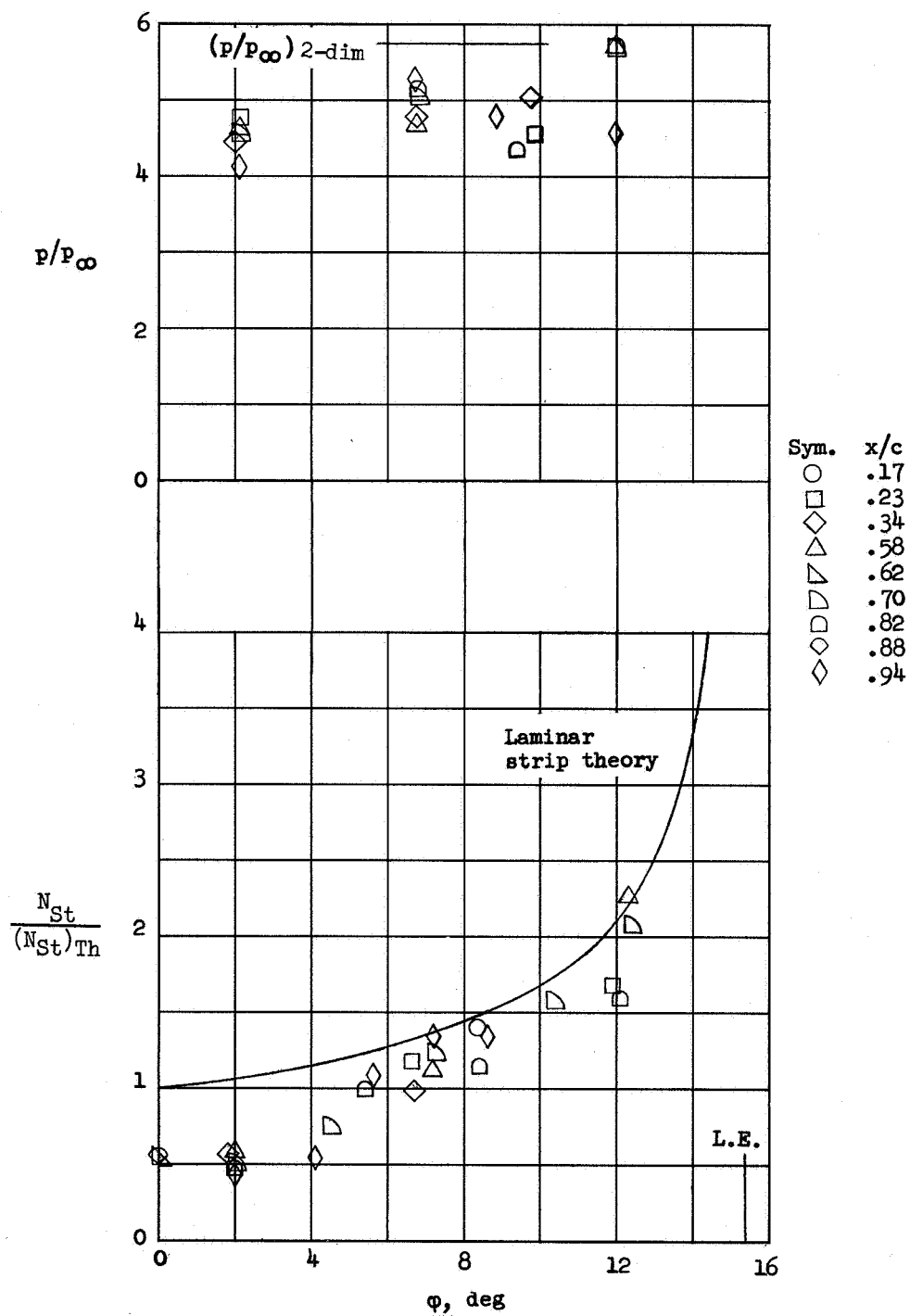
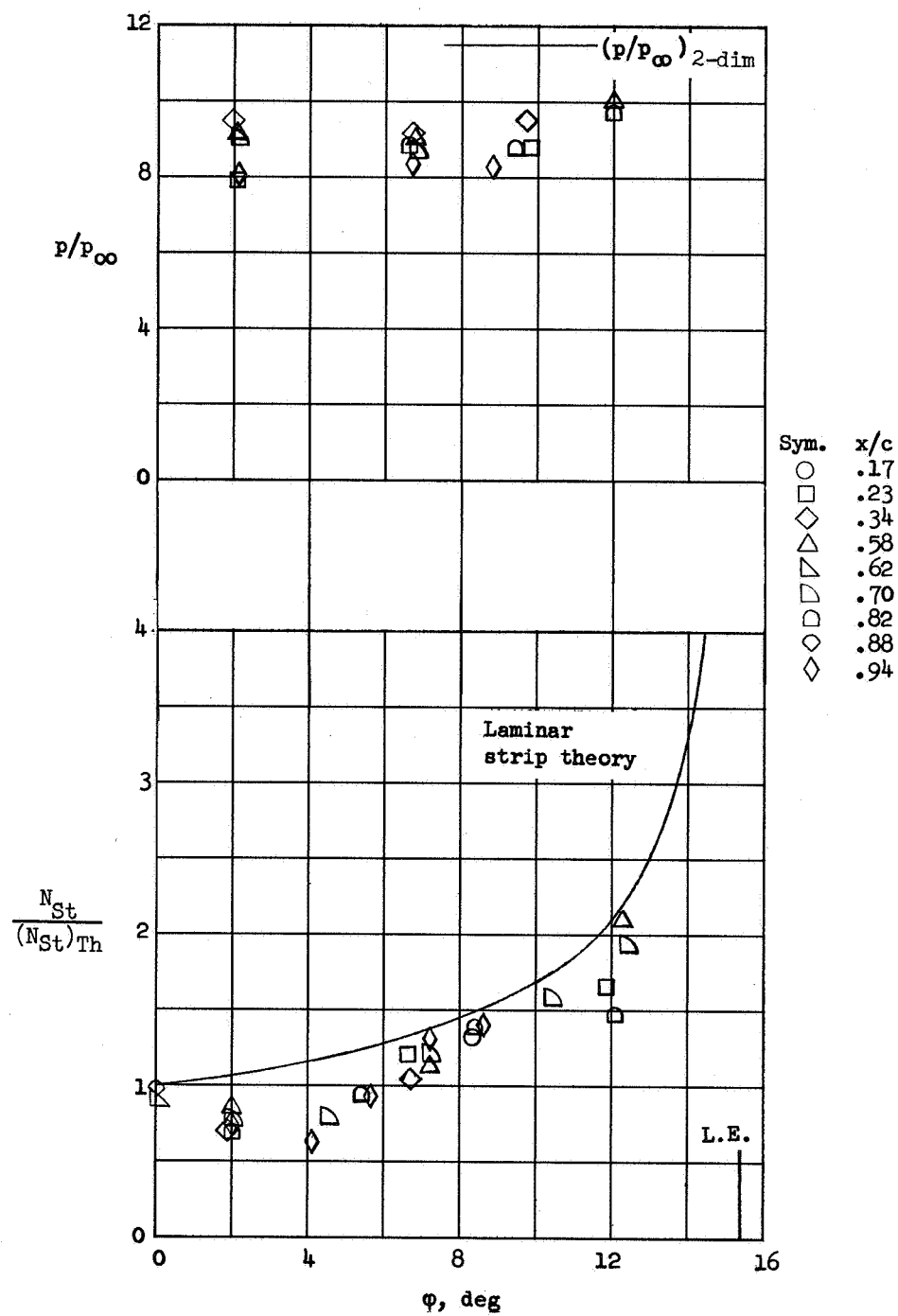
(b) $\alpha' = 9.0^\circ$.

Figure 9.- Continued.

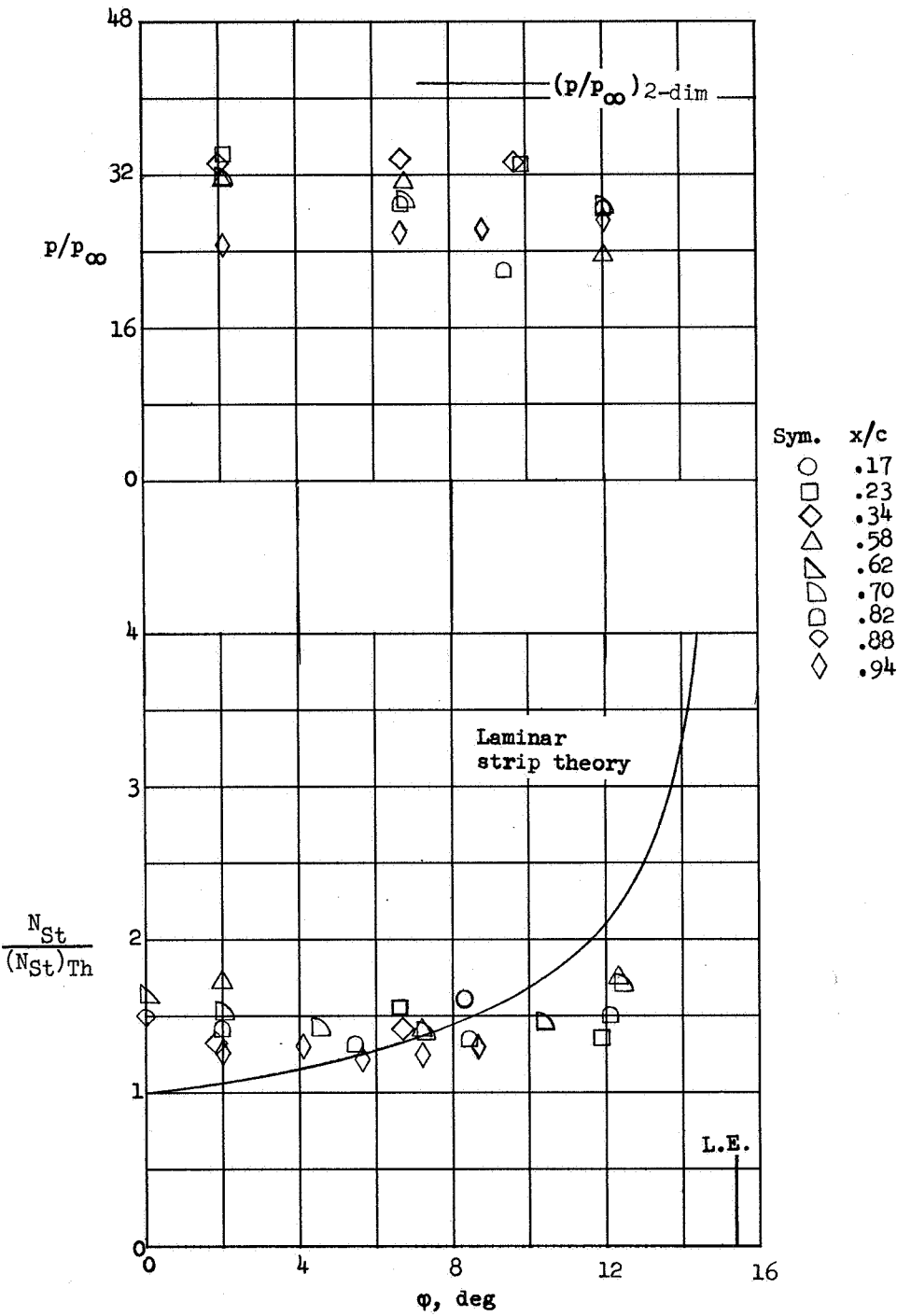


(c) $\alpha' = 14.2^\circ$.

Figure 9.- Continued.



L-928



(d) $\alpha' = 29.9^\circ$.

Figure 9.- Concluded.



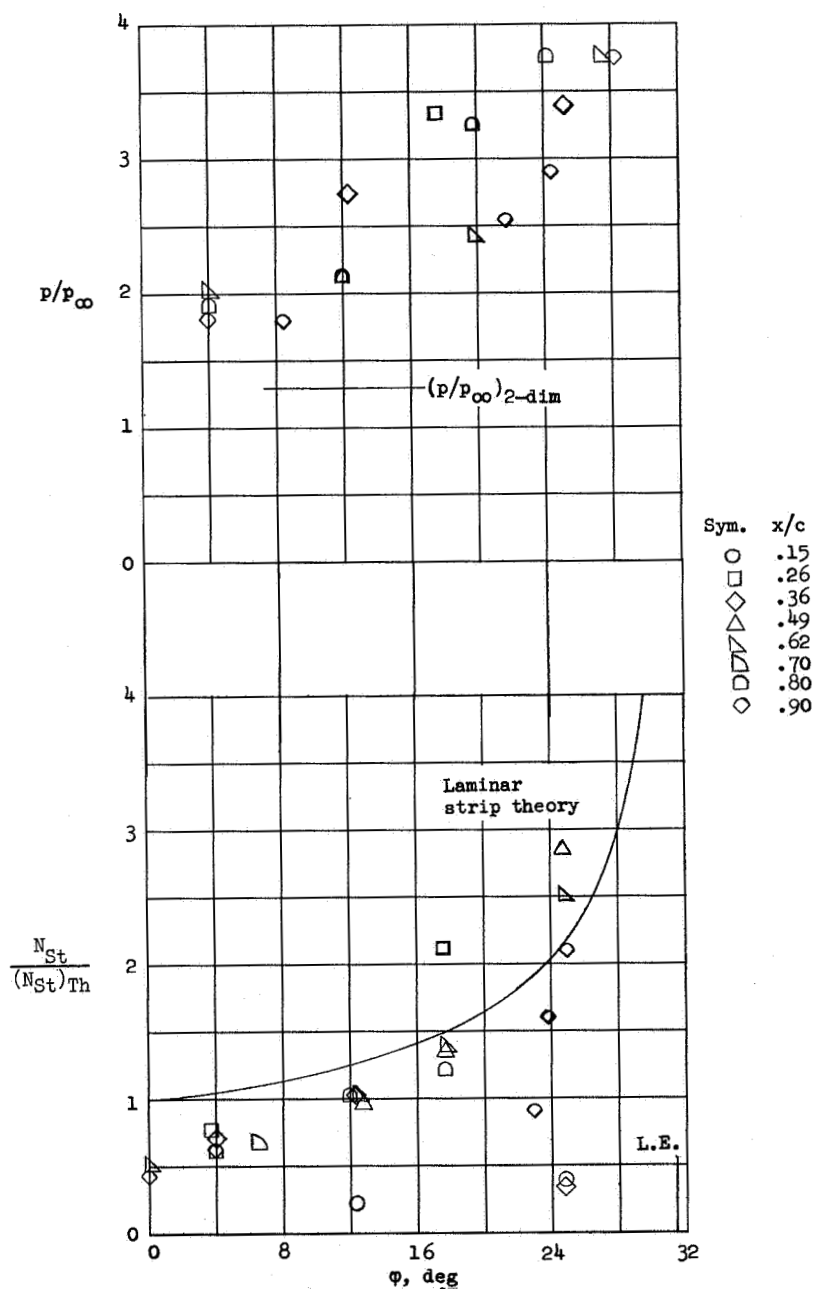
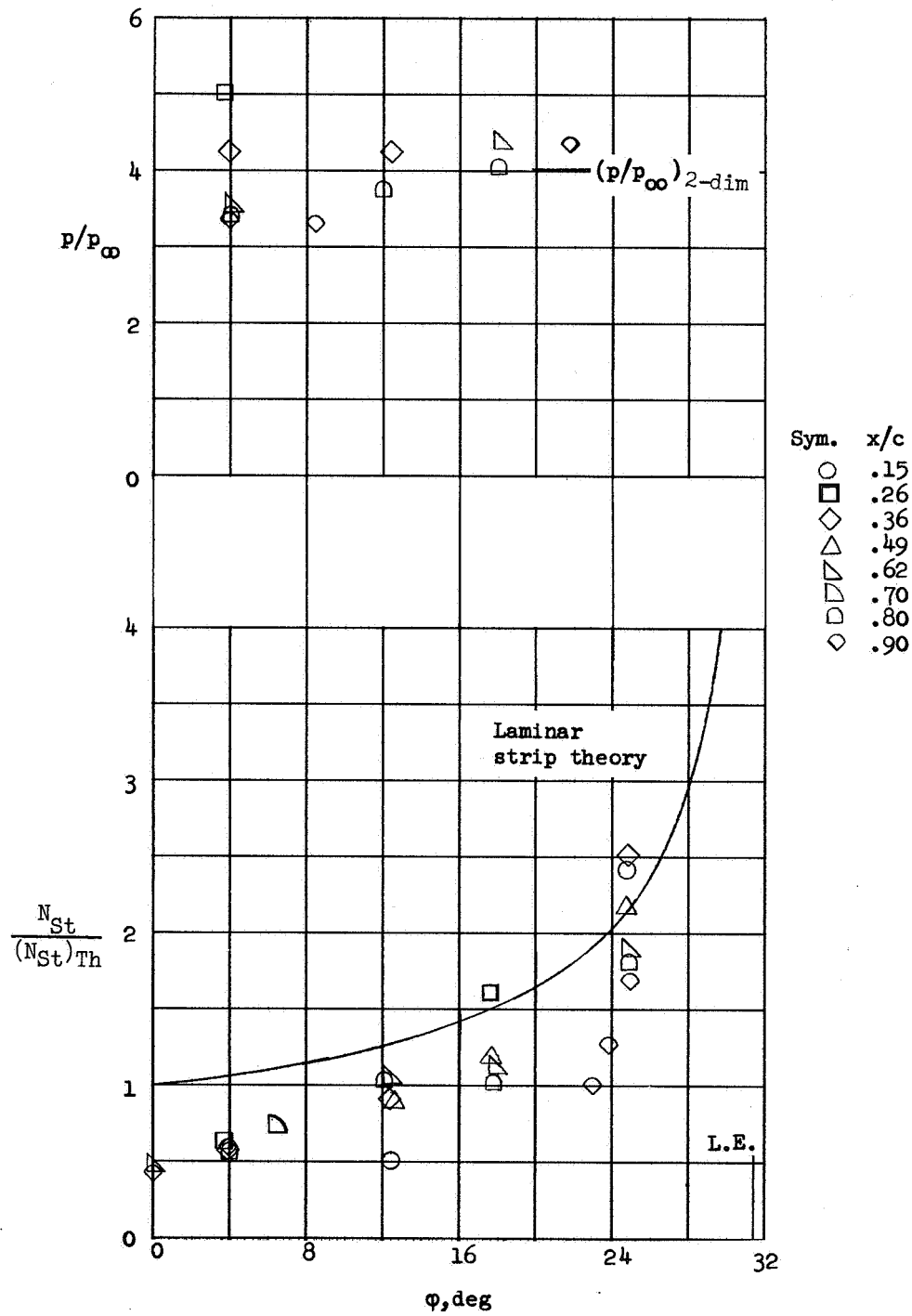
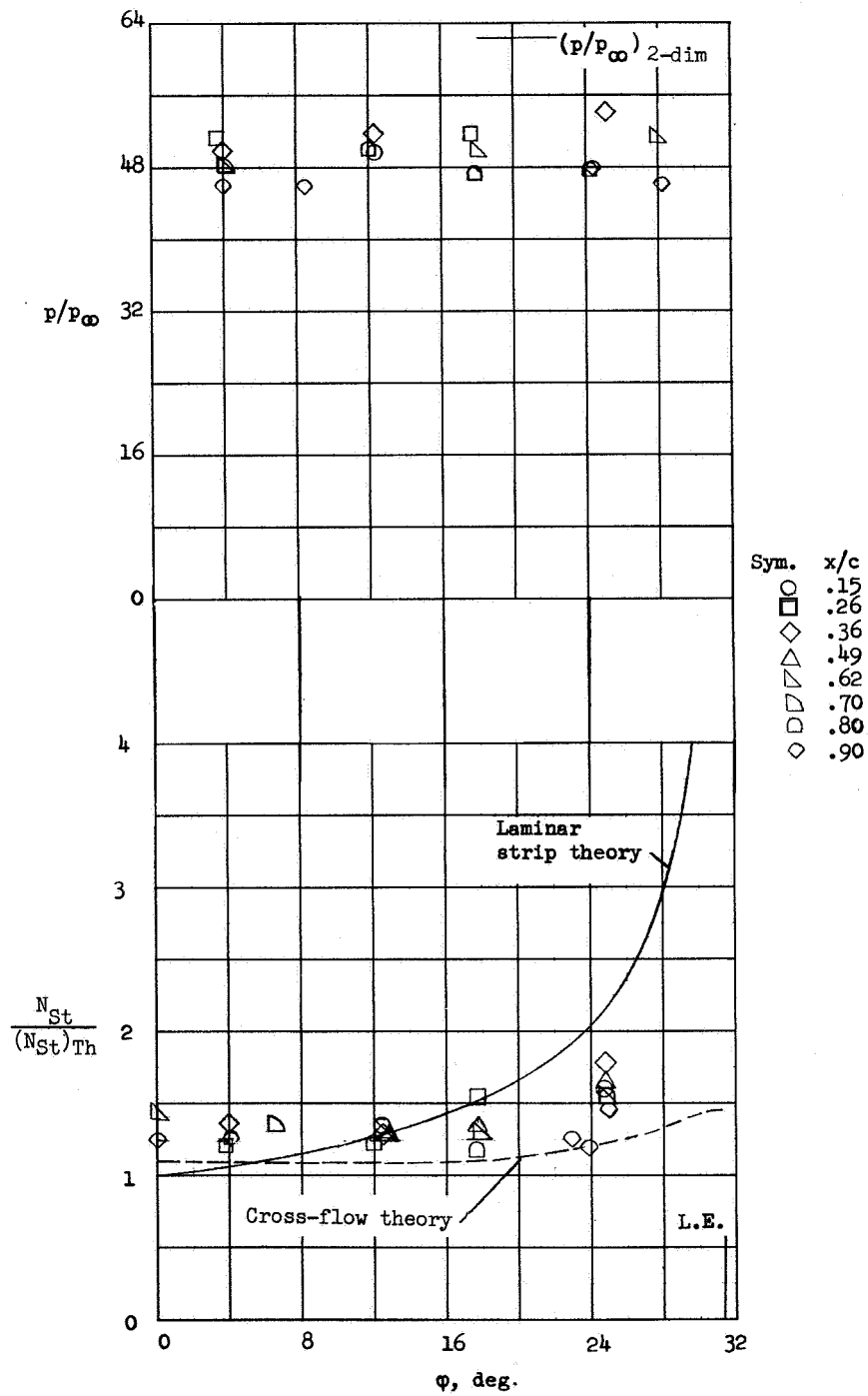
(a) $\alpha' = 1.1^\circ$.

Figure 10.- Spanwise distribution of pressure and ratio of heating to theoretical laminar heating on center line for strip theory. Delta-wing model V ($\Lambda = 60^\circ$, $\Gamma = 13^\circ$, blunt leading edge) at $M_\infty = 9.6$ and $R_C = 0.4 \times 10^6$.



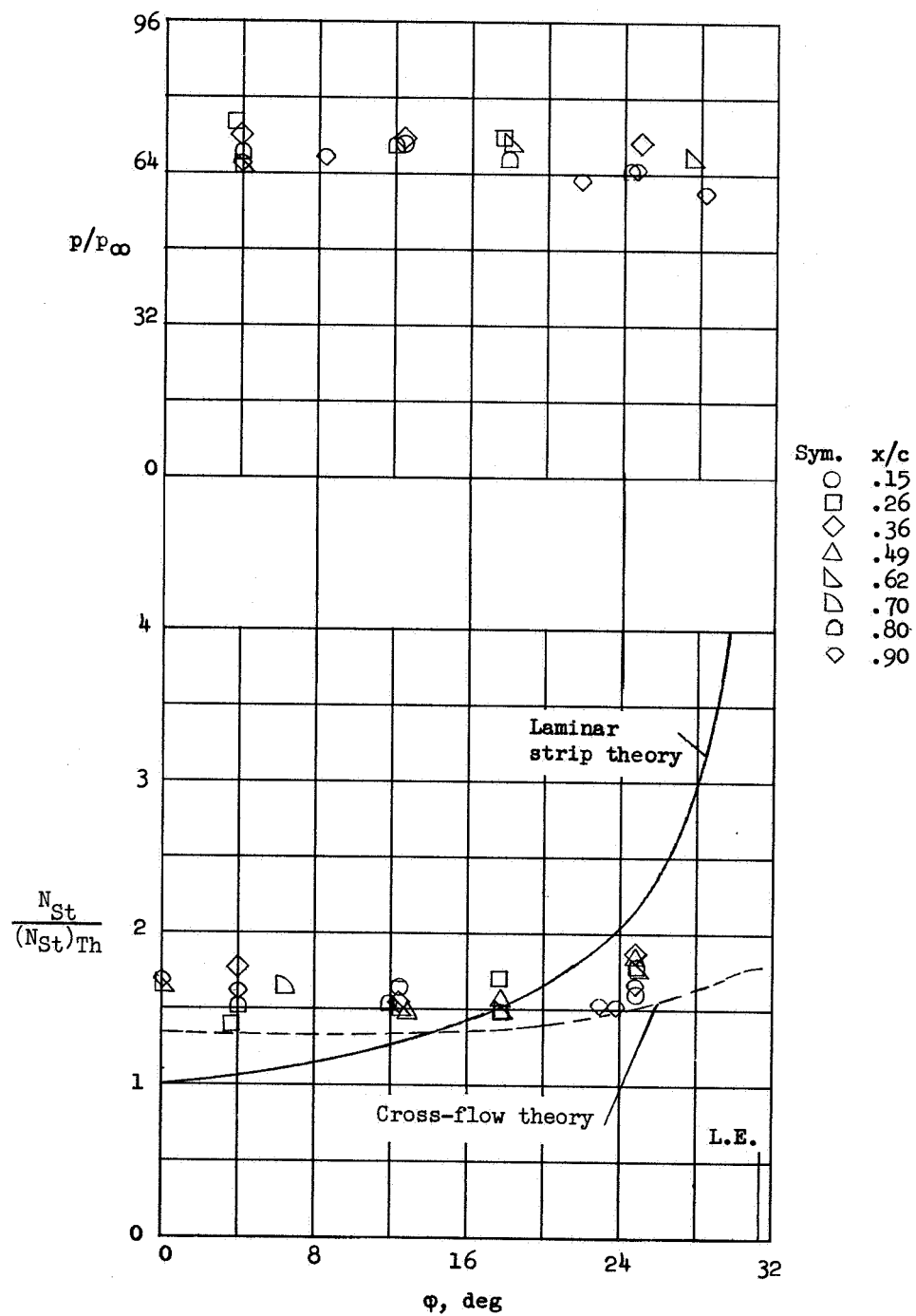
(b) $\alpha' = 6.8^\circ$.

Figure 10.- Continued.



(e) $\alpha' = 38.0^\circ$.

Figure 10.- Continued.



(f) $\alpha' = 47.5^\circ$.

Figure 10.- Concluded.

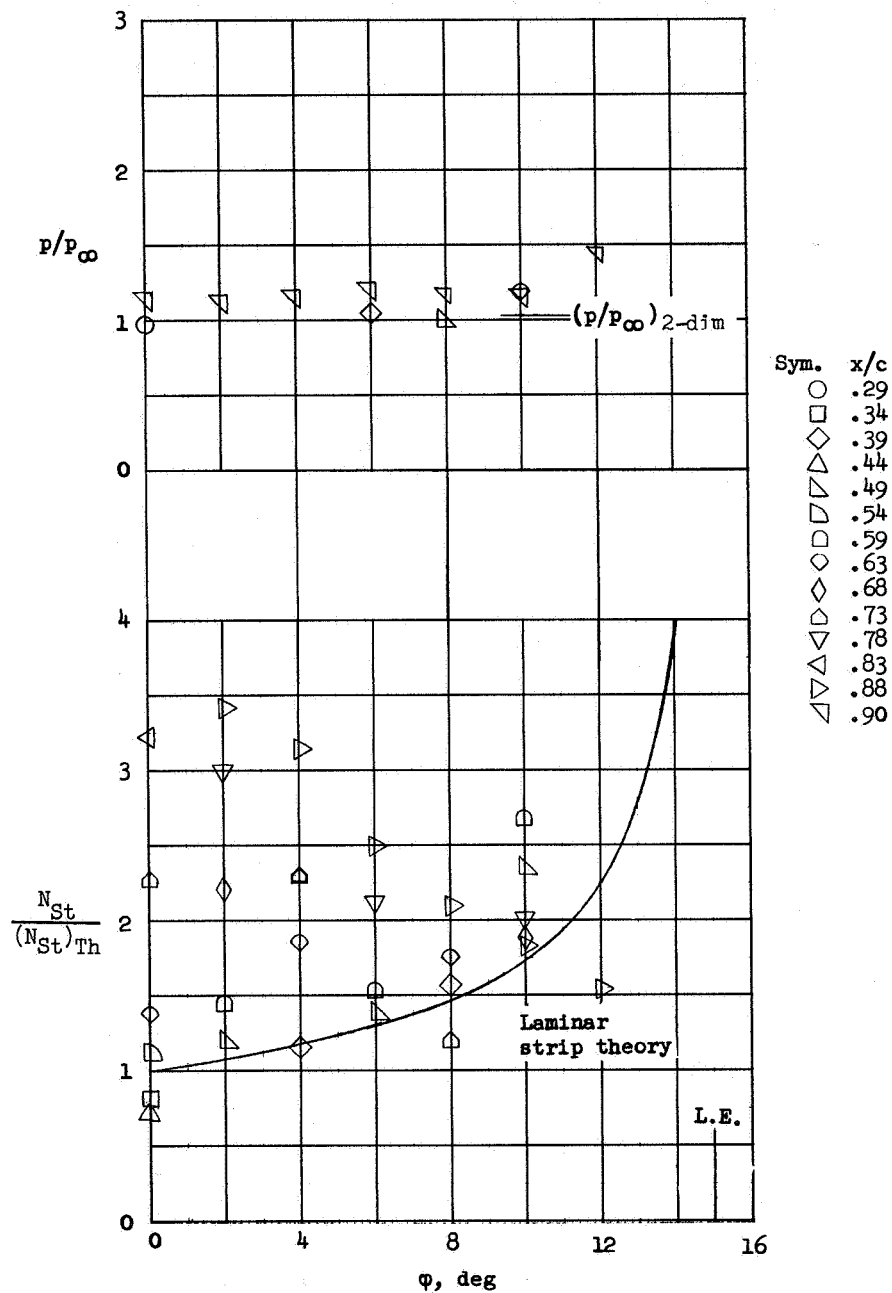
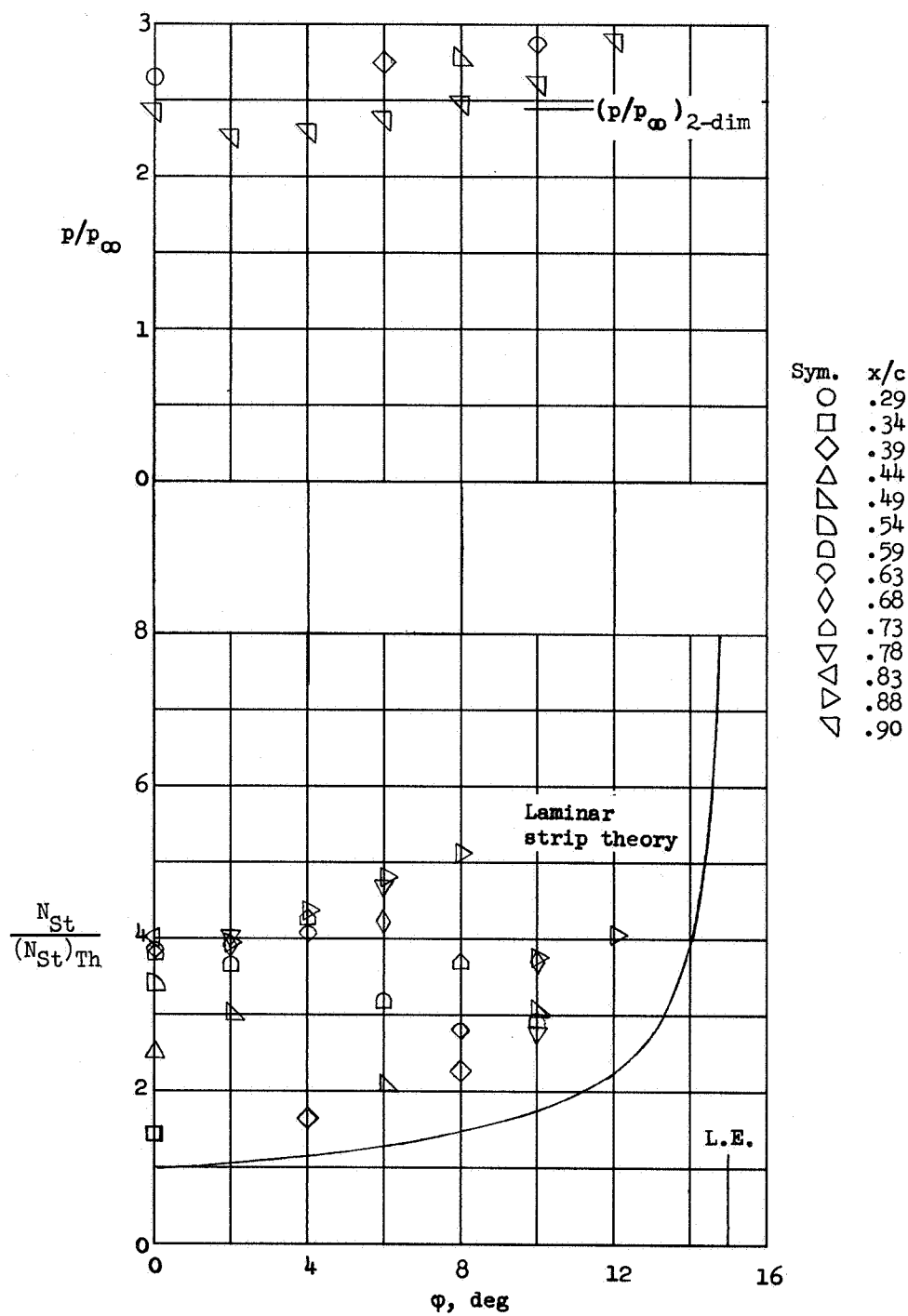
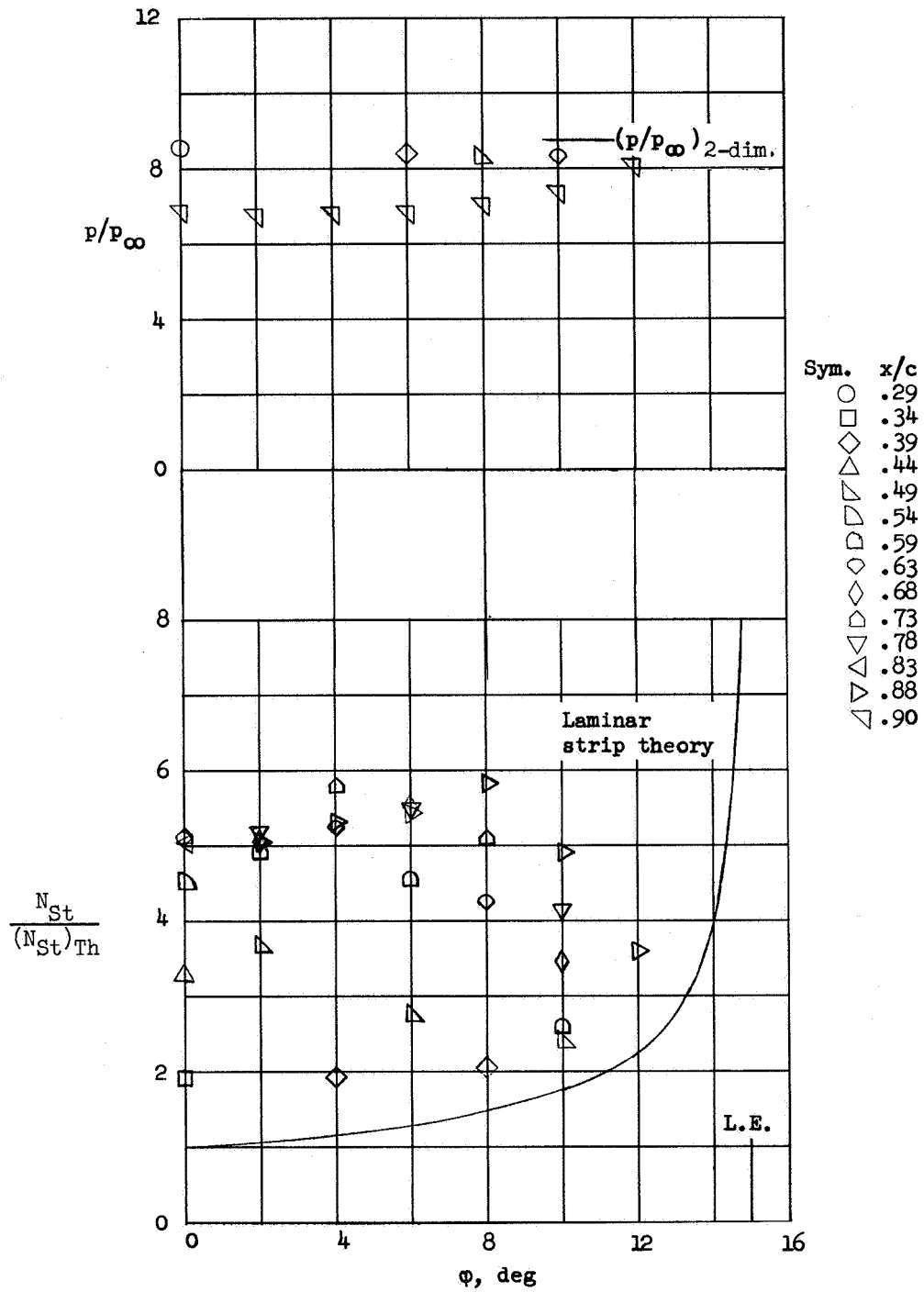
(a) $\alpha = 0.1^\circ$.

Figure 11.- Spanwise distribution of pressure and ratio of heating to theoretical laminar heating on center line for strip theory. Delta-wing model VI ($\Lambda = 75^\circ$, $\Gamma = 0^\circ$, sharp leading edge) at $M_\infty = 6.8$ and $R_c = 2 \times 10^6$.



(b) $\alpha = 5.8^\circ$.

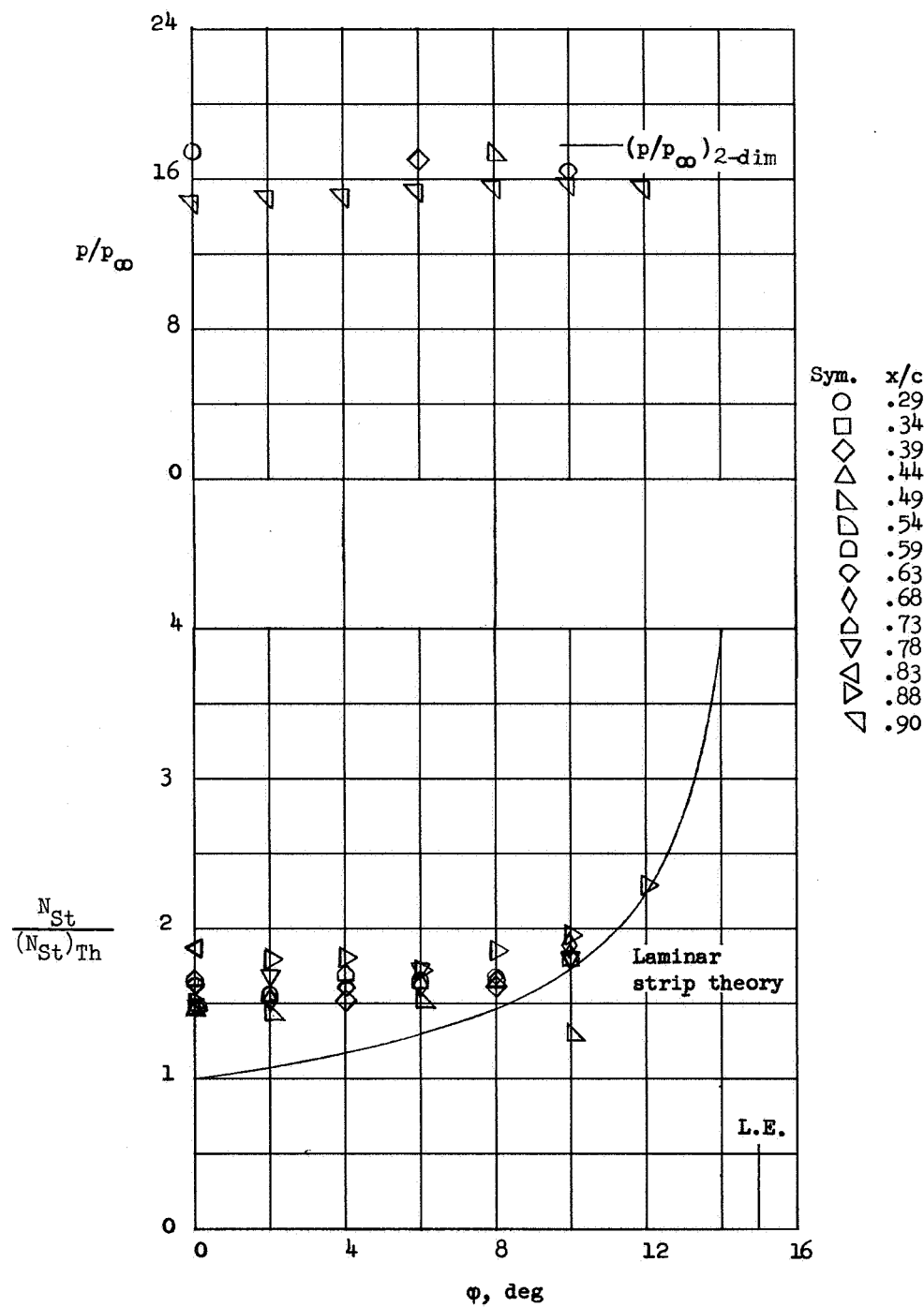
Figure 11.- Continued.



(c) $\alpha = 17.0^\circ$.

Figure 11.- Continued.

L-928



(d) $\alpha = 27.3^\circ$.

Figure 11.- Concluded.

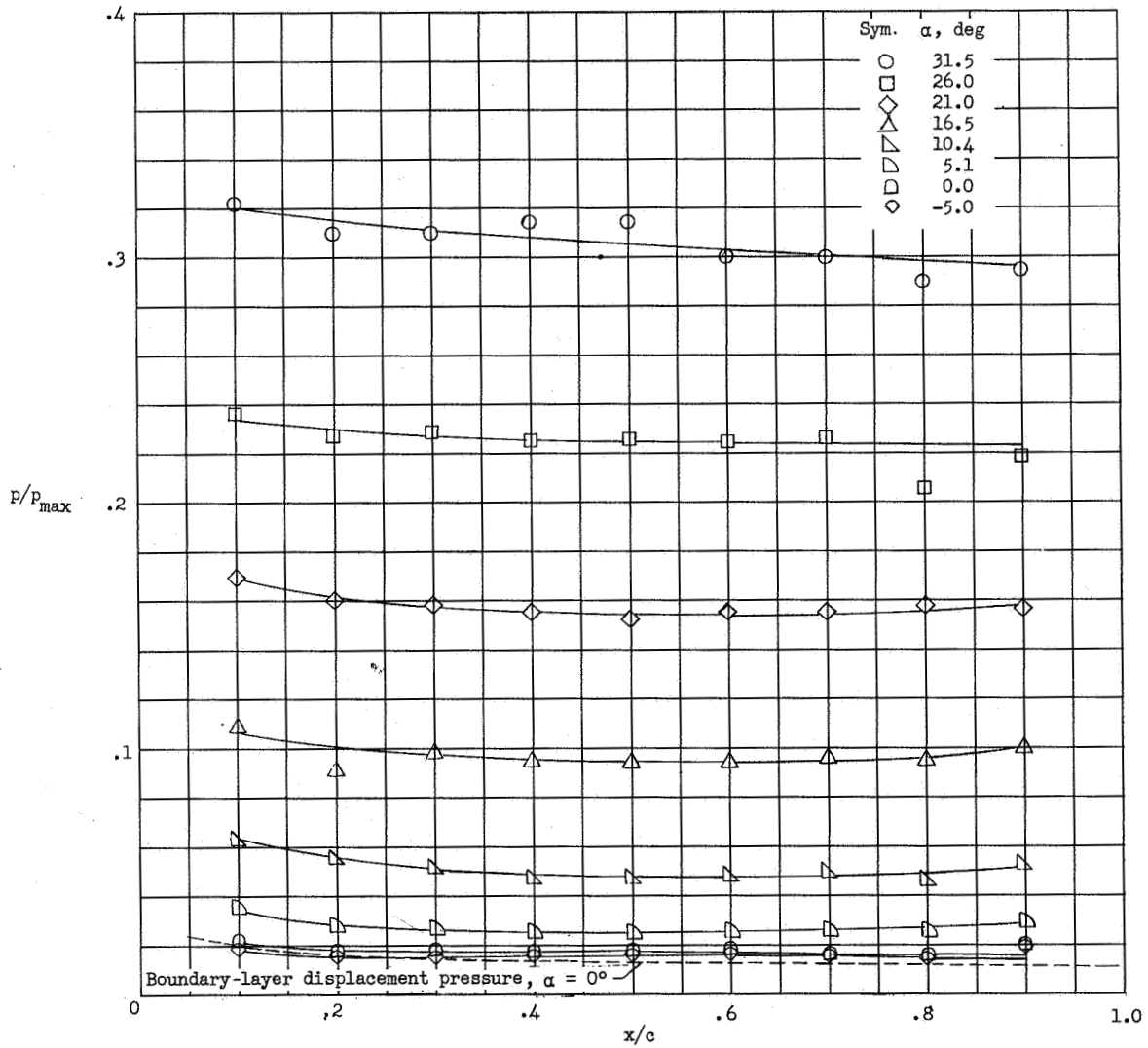


Figure 12.- Center-line pressures at angles of attack for delta-wing model VIII (flat, sharp leading edge, $\Lambda = 75^\circ$) at $M_\infty = 9.6$.

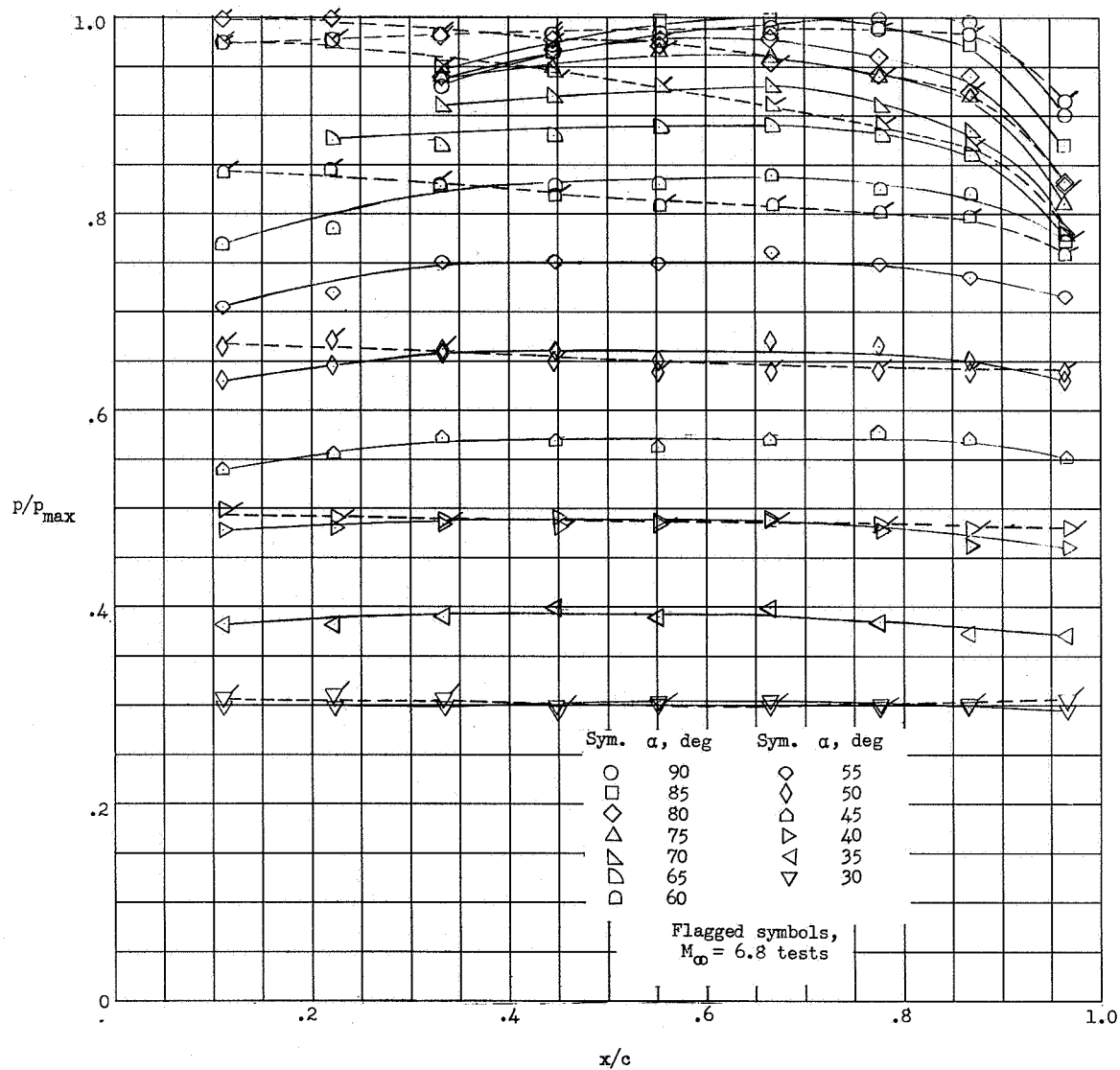


Figure 13.- Center-line pressures at angles of attack for delta-wing model VII (flat, sharp leading edge, $\Lambda = 75^\circ$) at $M_{\infty} = 6.8$ and 9.6.

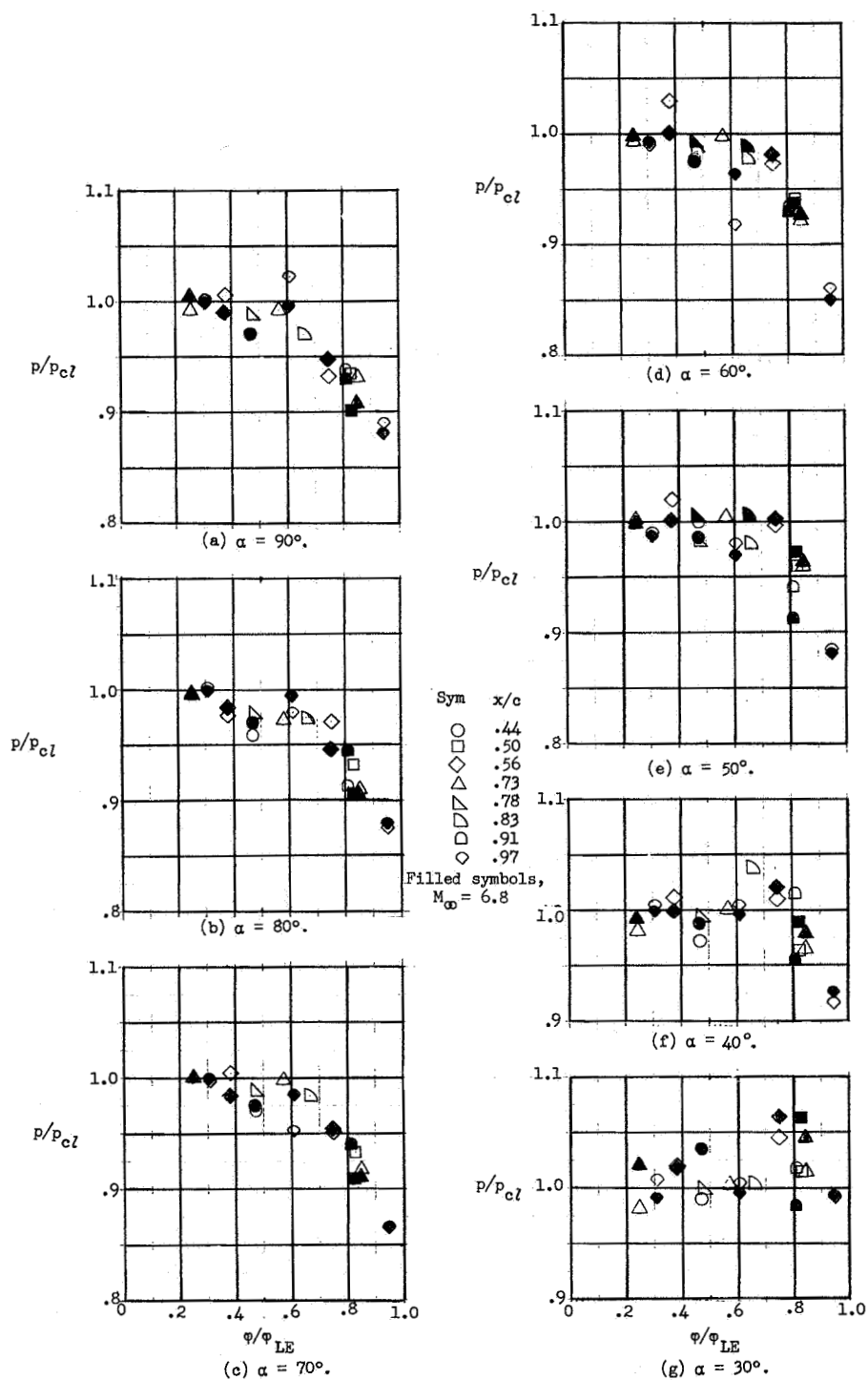


Figure 14.- Spanwise distribution of pressure on delta-wing model VII (flat, sharp leading edge, $\Lambda = 75^\circ$) at $M_\infty = 6.8$ and 9.6.

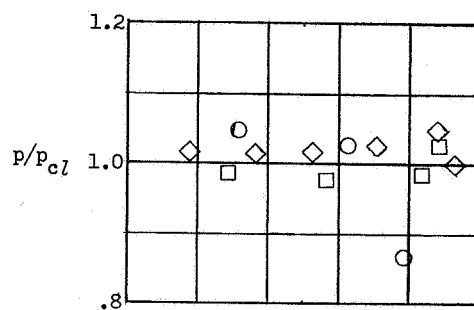
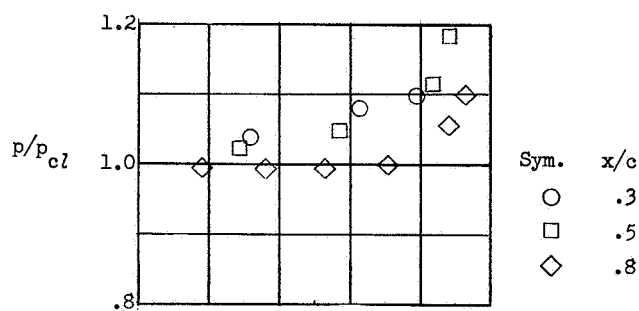
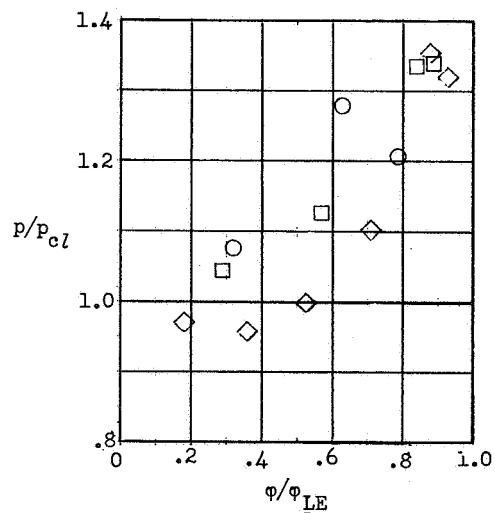
(a) $\alpha = 31.6^\circ$.(b) $\alpha = 21.0^\circ$.(c) $\alpha = 10.4^\circ$.

Figure 15.- Spanwise distribution of pressure on delta-wing model VIII
(flat, sharp leading edge, $\Lambda = 75^\circ$) at $M_\infty = 9.6$.

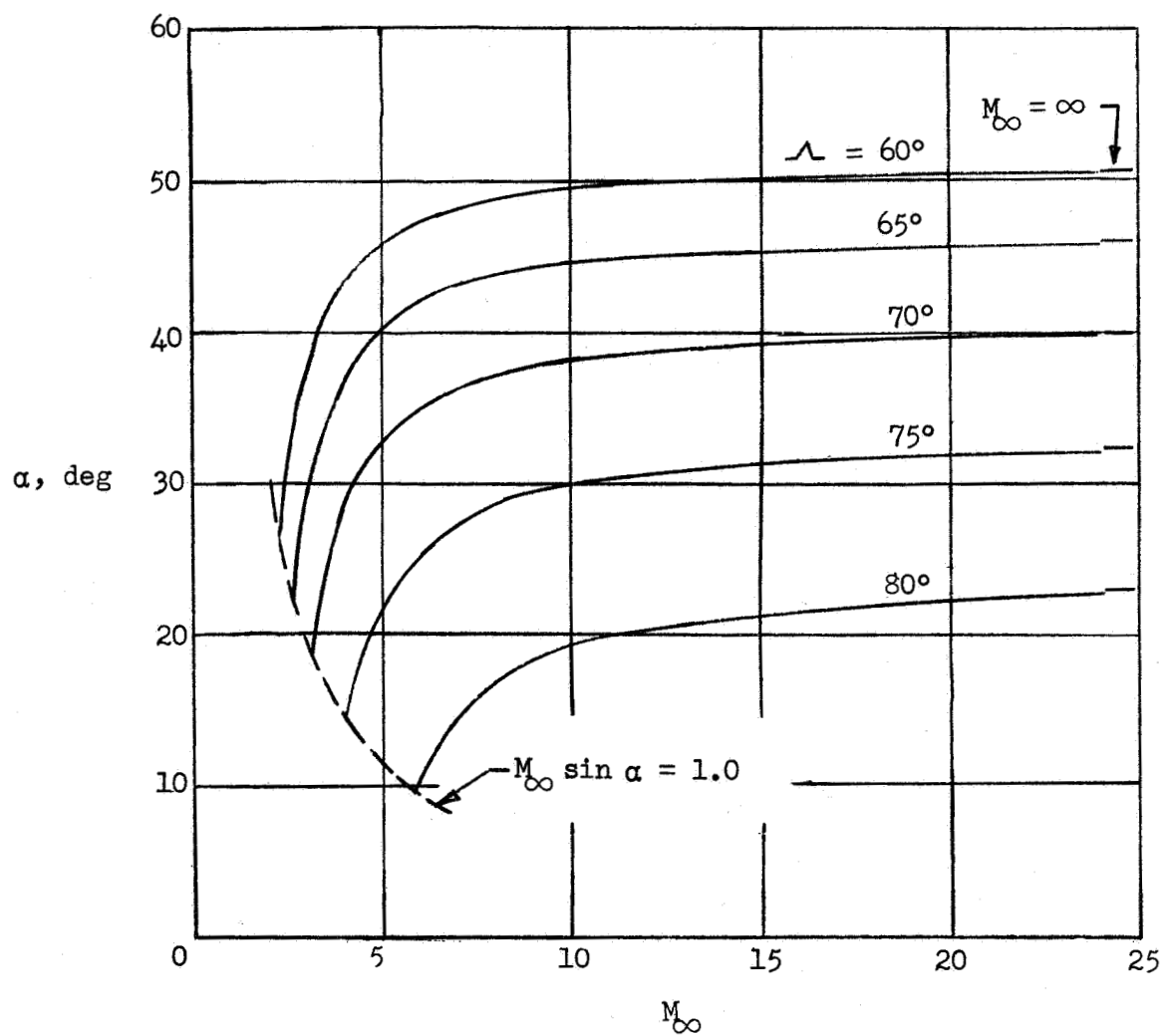
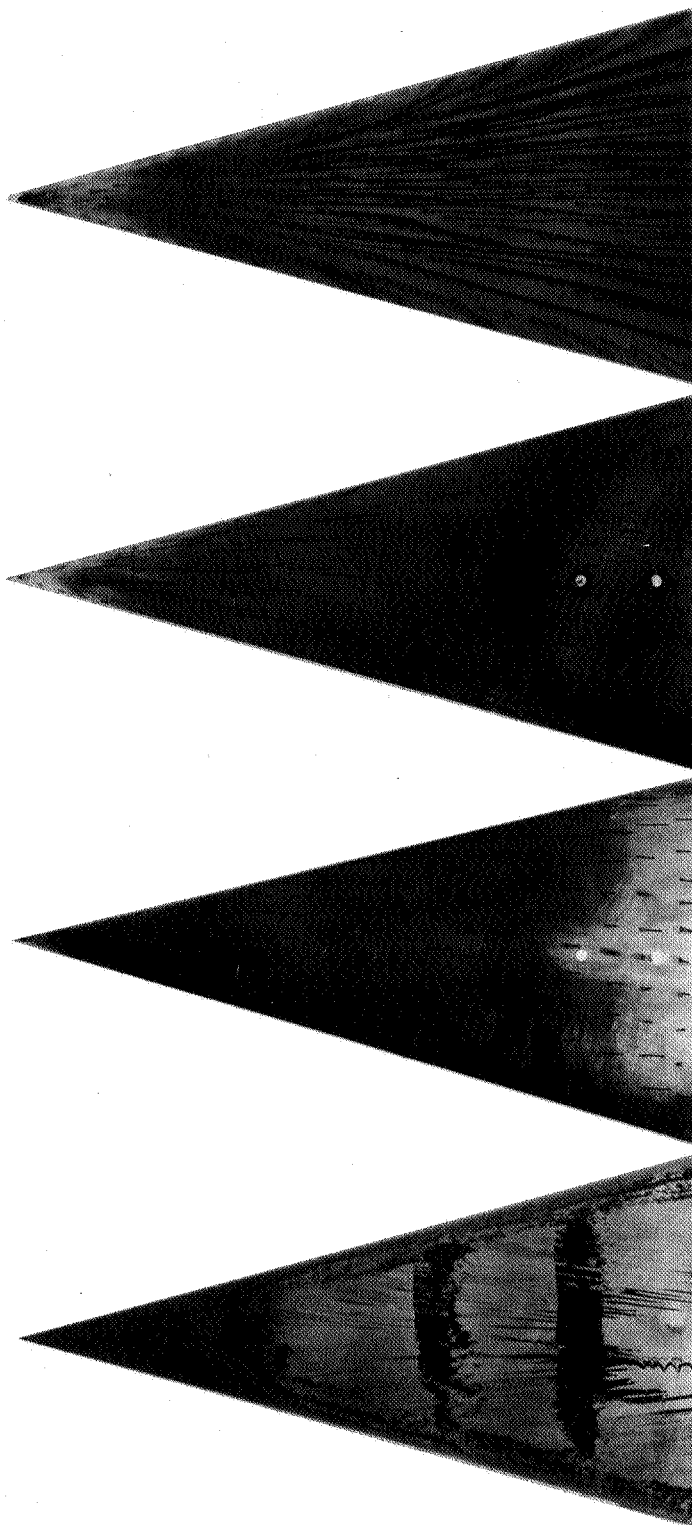
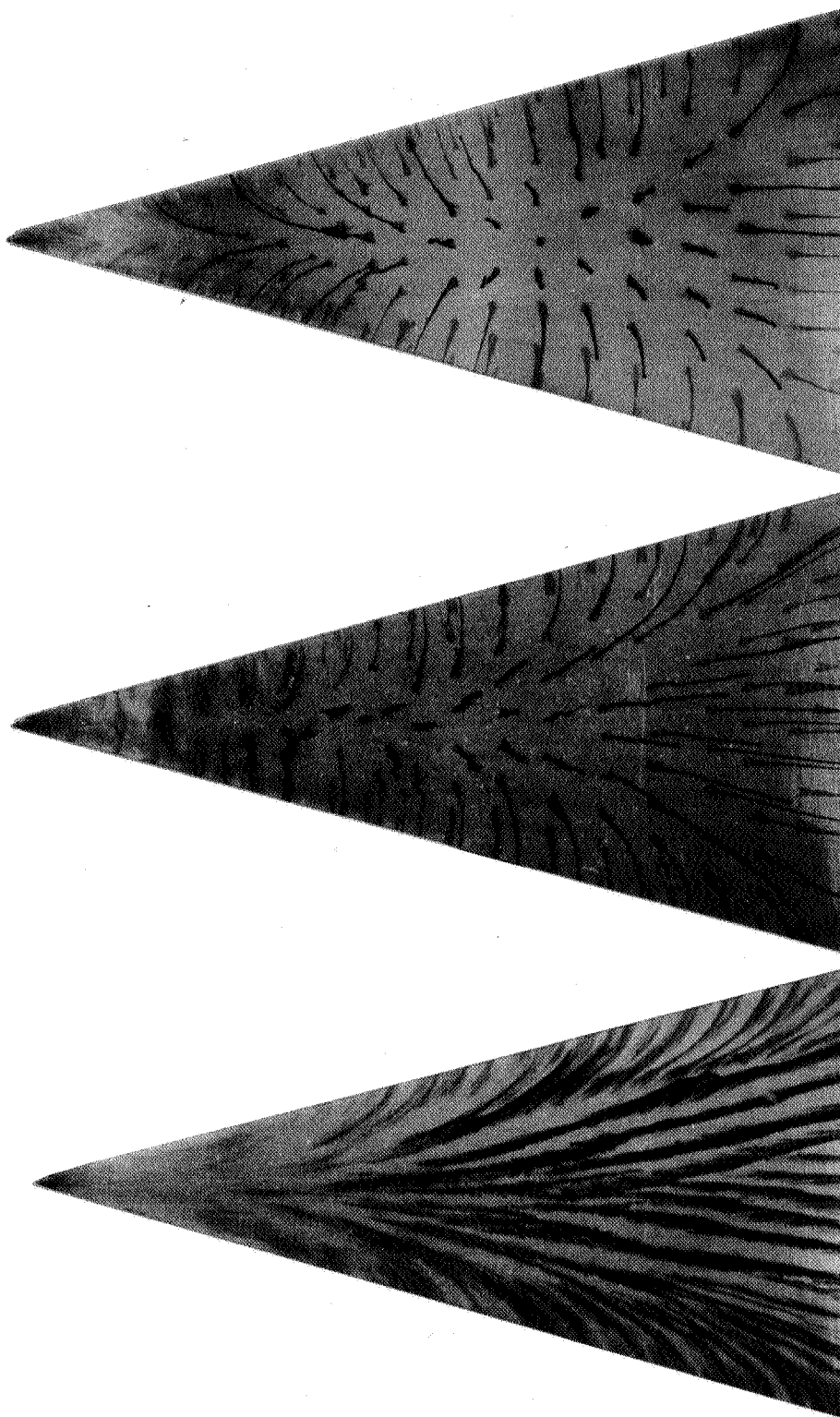


Figure 16.- Theoretical minimum angle of attack for outflow at leading edge of flat, sharp-leading-edge delta wings. $\gamma = 7/5$.



(a) $\alpha = 0^\circ$. (b) $\alpha = 15^\circ$. (c) $\alpha = 30.0^\circ$. (d) $\alpha = 45.0^\circ$.
 Figure 17.- Photographs of oil-flow traces on a flat, sharp-leading-edge, 75° swept delta wing
 L-62-50
 at $M_\infty = 9.6$.

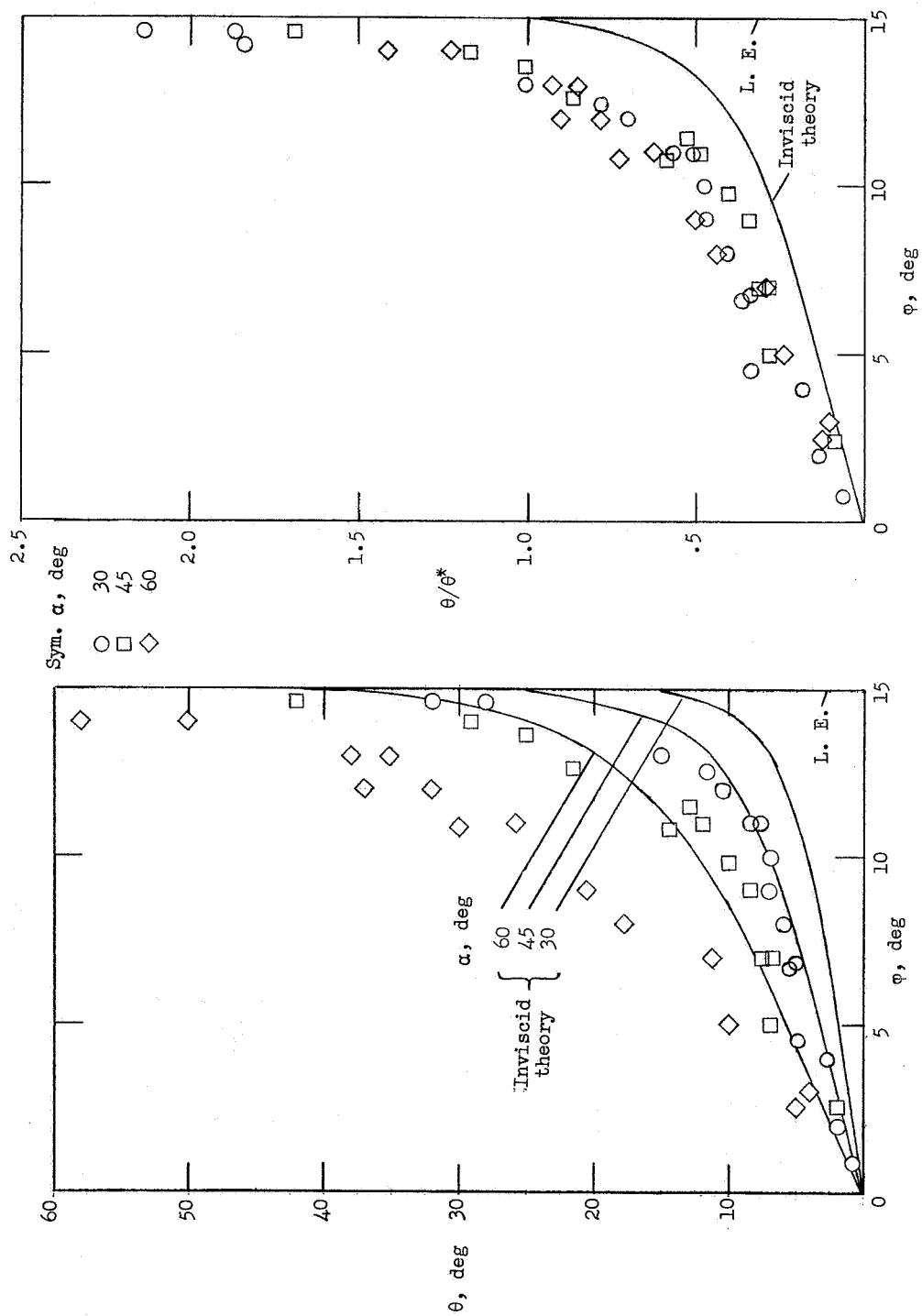


(e) $\alpha = 60.0^\circ$.

(f) $\alpha = 75.0^\circ$.

(g) $\alpha = 90.0^\circ$.

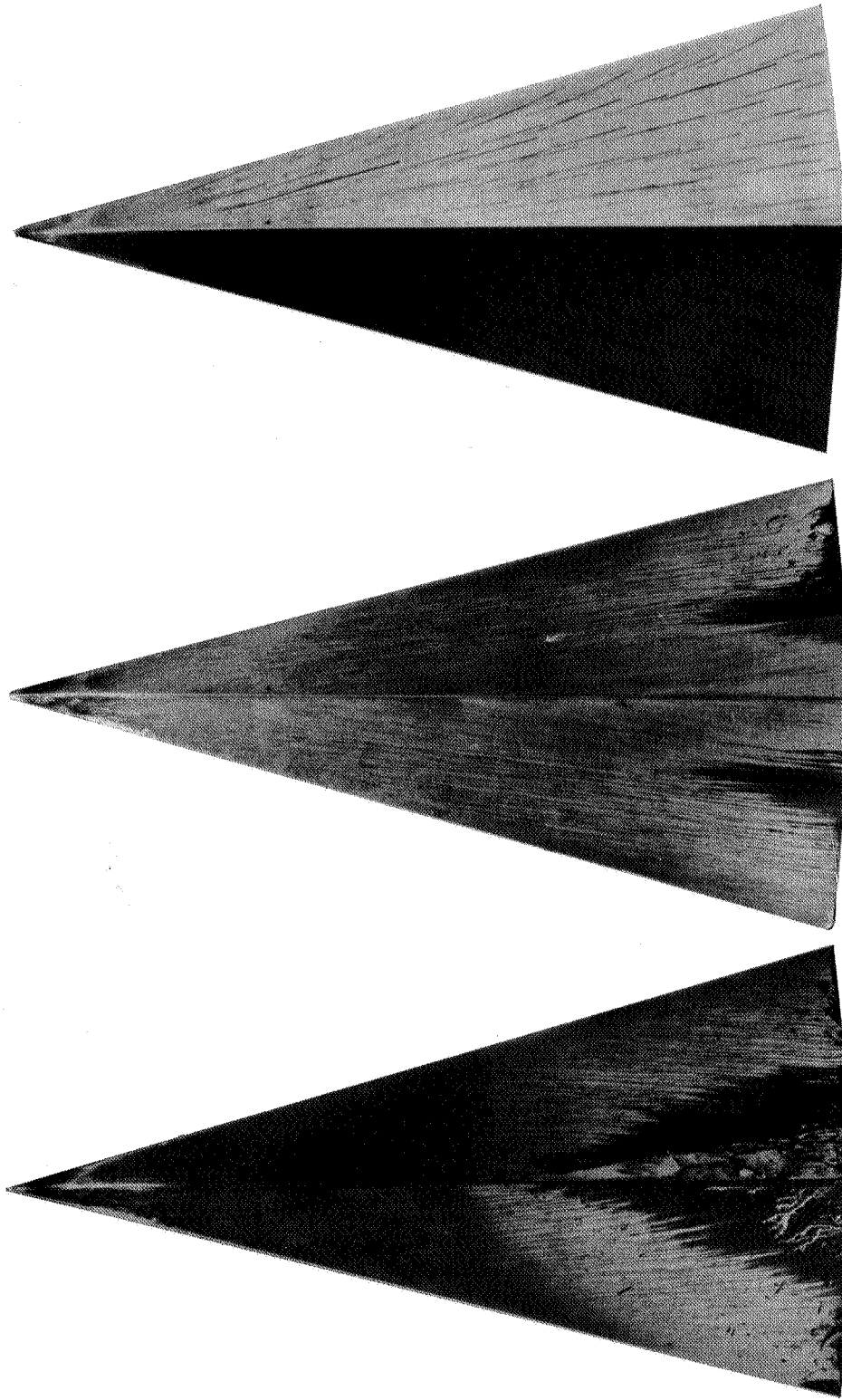
Figure 17.- Concluded. L-62-51



(a) Flow angles.

(b) Correlated flow angles.

Figure 18.- Comparison and correlation of oil-flow trace angles with theoretical flow angles outside the boundary layer on a flat, sharp-leading-edge, 75° swept delta wing at $M_\infty = 9.6$.



(a) $\alpha' = 0^\circ$. (b) $\alpha' = 13.5^\circ$. (c) $\alpha' = 27^\circ$. I-62-52
 Figure 19.- Photographs of oil-flow traces on a 26° dihedral, sharp-leading-edge, 75° swept
 delta wing at $M_\infty = 9.6$.

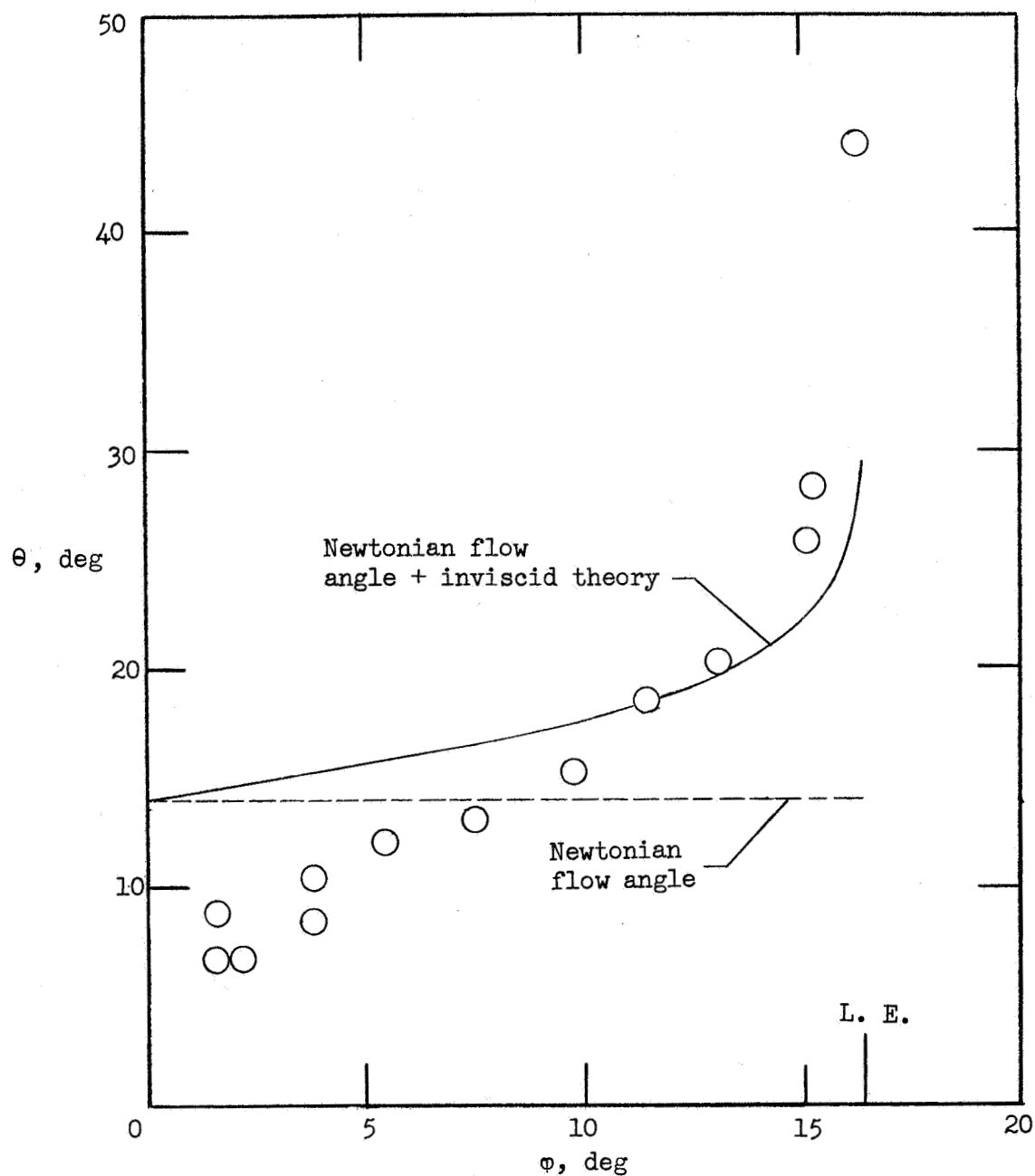


Figure 20.- Comparison of oil-flow trace angles with theoretical flow angles outside the boundary layer for a 26° dihedral, sharp-leading-edge, 75° swept delta wing at $\alpha' = 27^\circ$ and $M_\infty = 9.6$.

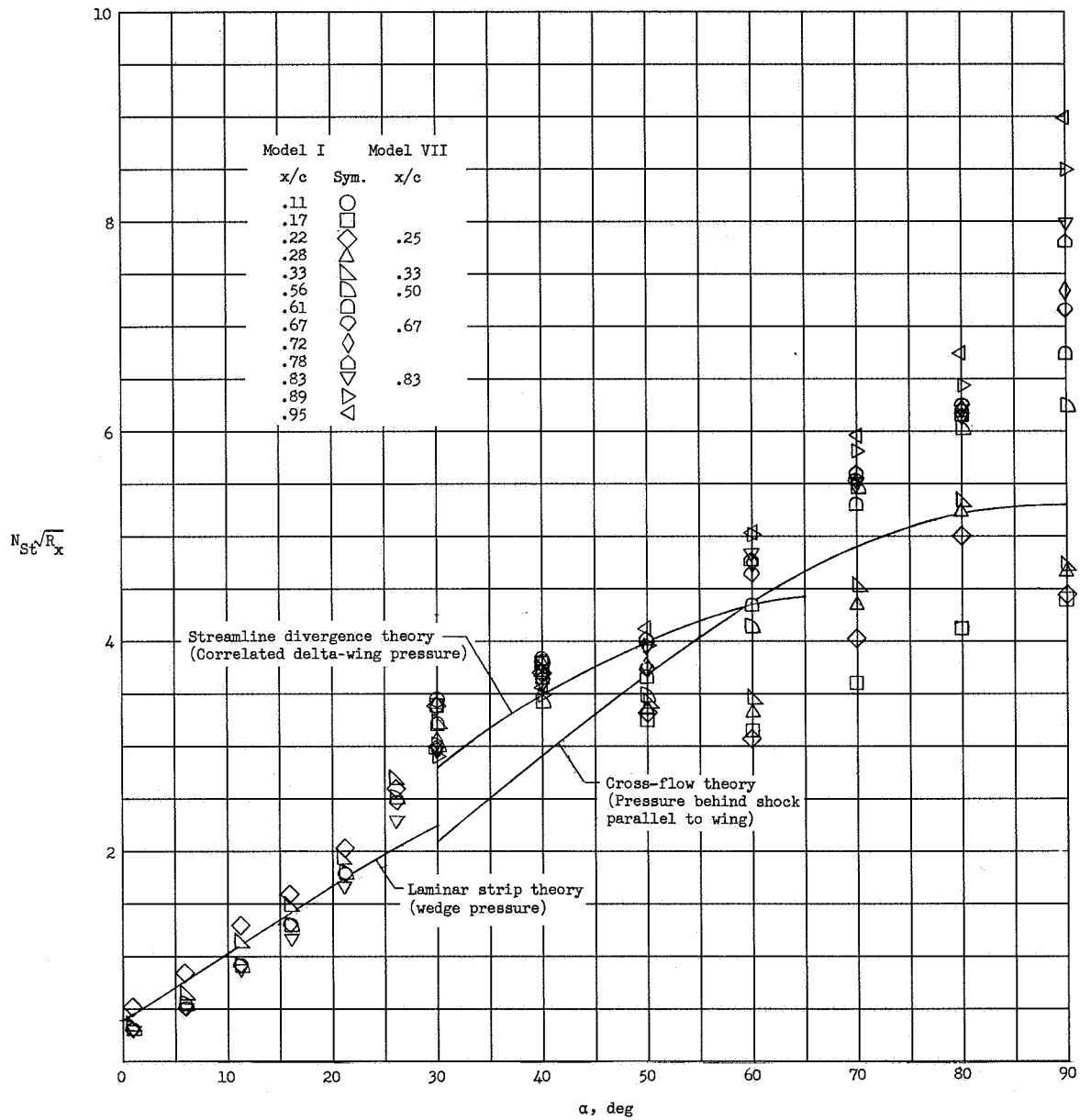


Figure 21.- Comparison of center-line heating with theory for delta wings I and VII (flat, sharp leading edge, $\Lambda = 75^\circ$) at $M_\infty = 9.6$.

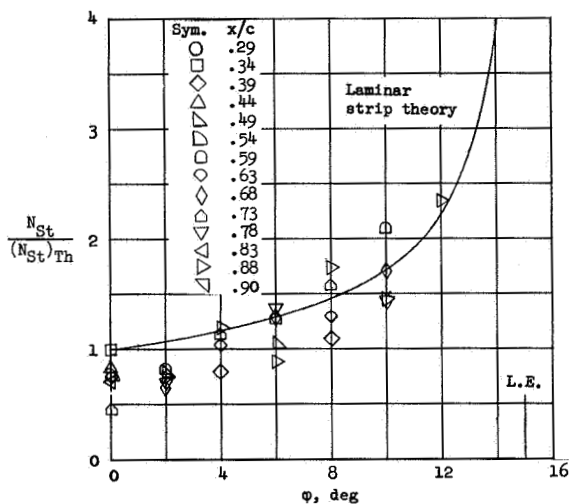
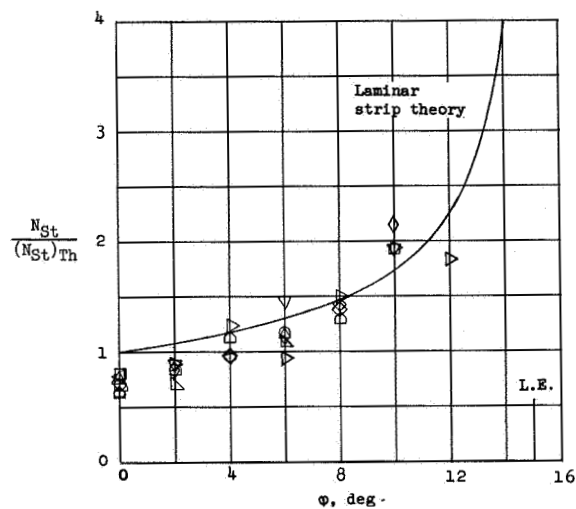
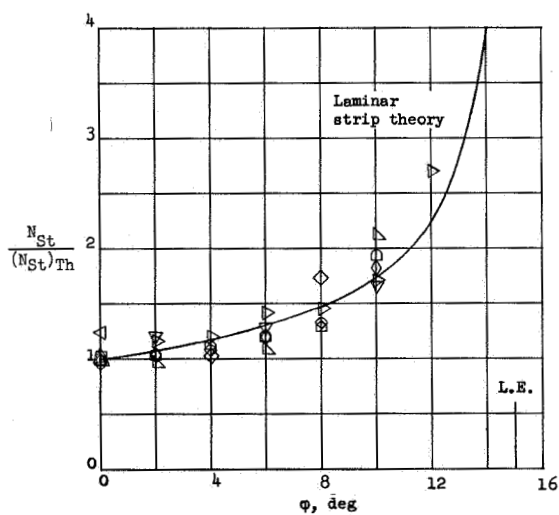
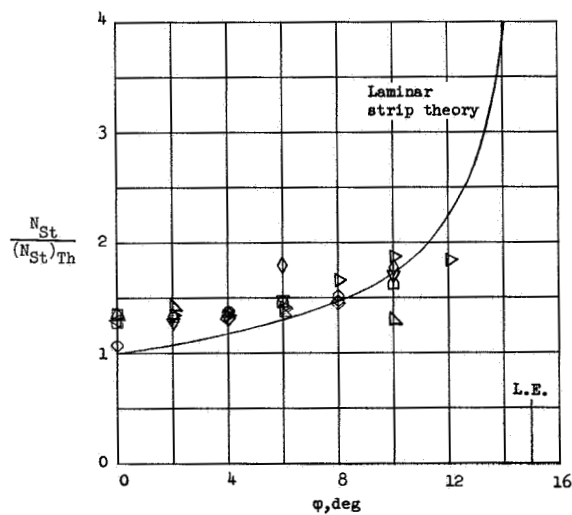
(a) $\alpha = 0.4^\circ$.(b) $\alpha = 5.5^\circ$.(c) $\alpha = 15.5^\circ$.(d) $\alpha = 25.8^\circ$.

Figure 22.- Spanwise distribution of ratio of heating to theoretical laminar heating on center line for strip theory. Delta-wing model VI ($\Lambda = 75^\circ$, $\Gamma = 0^\circ$, sharp leading edge) at $M_\infty = 6.8$ and $R_c = 0.5 \times 10^6$.

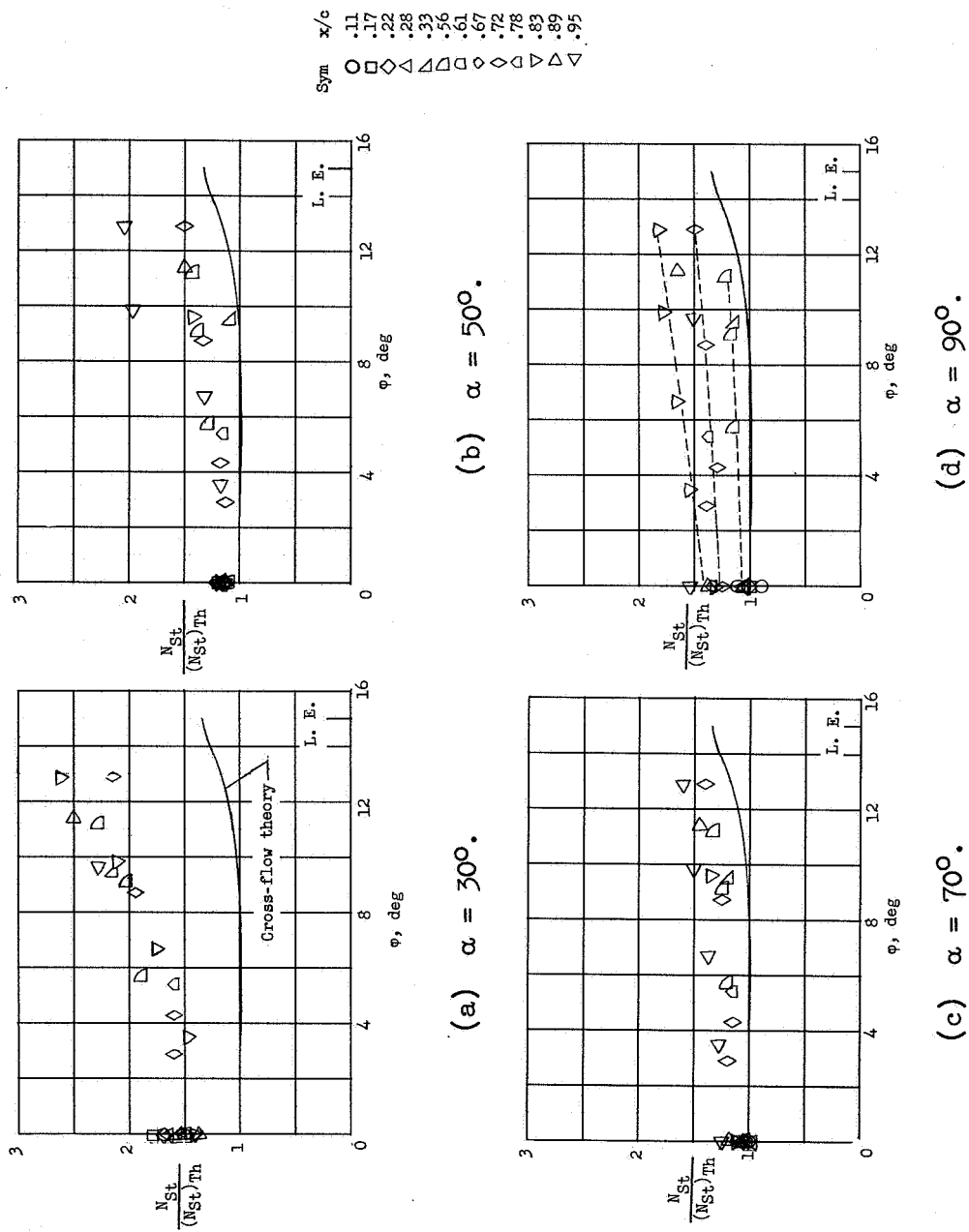


Figure 23.- Spanwise distribution of ratio of heating to theoretical laminar heating on center line for cross-flow theory. Delta-wing model VII ($\Lambda = 75^\circ$, $\Gamma = 0^\circ$, sharp leading edge) at $M_\infty = 6.8$ and $R_c = 0.9 \times 10^6$.

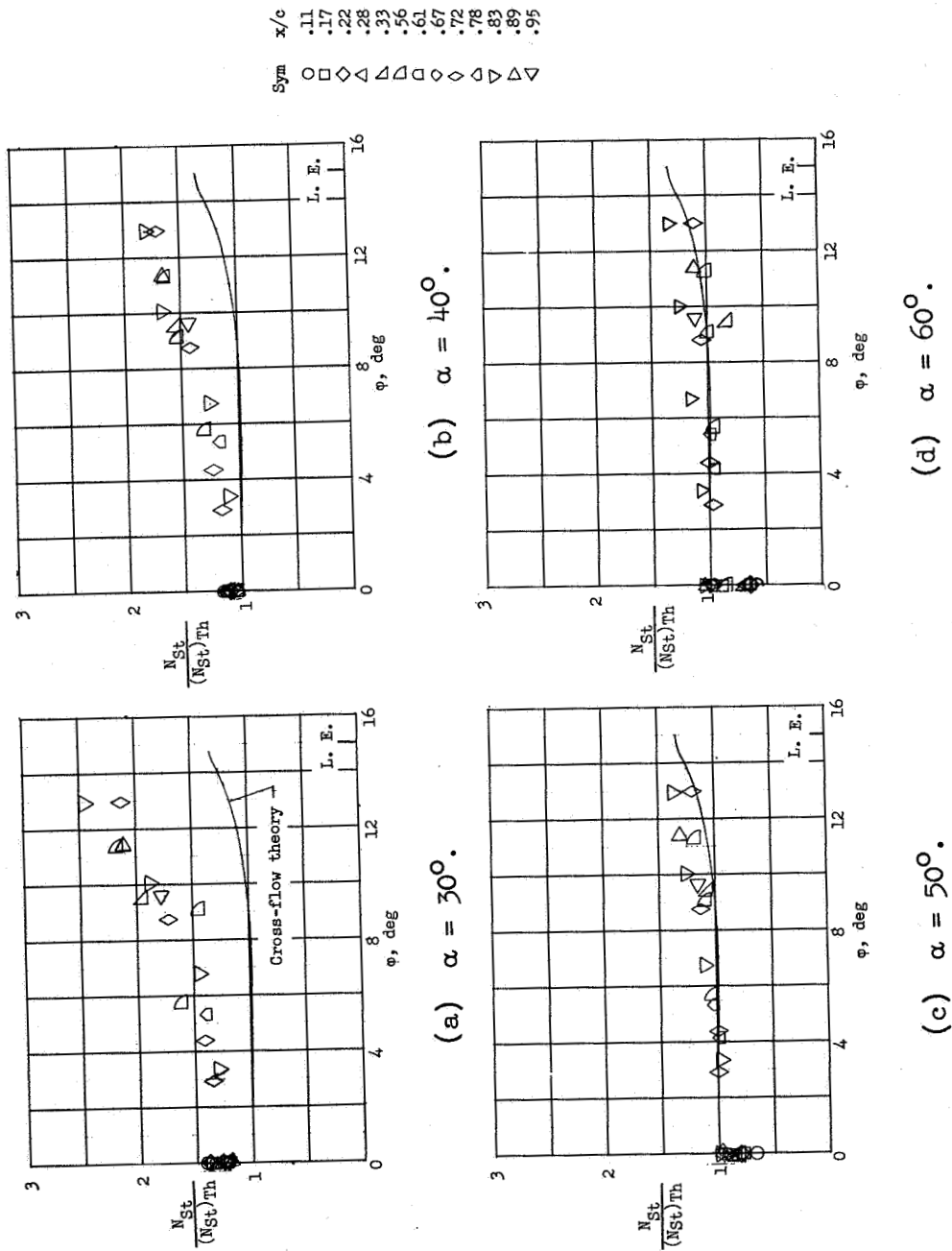
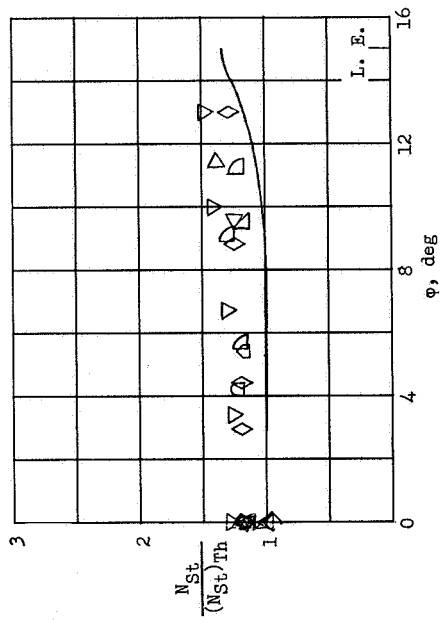


Figure 24.- Spanwise distribution of ratio of heating to theoretical laminar heating on center line for cross-flow theory. Delta-wing model VII ($\Lambda = 75^\circ$, $\Gamma = 0^\circ$, sharp leading edge) at $M_\infty = 9.6$ and $R_C = 0.5 \times 10^6$.

(f) $\alpha = 80^\circ$.

Sym. x/c

○	.11
□	.17
◇	.22
△	.28
▽	.33
△	.56
□	.61
◇	.67
◇	.72
△	.78
▽	.83
△	.89
▽	.95

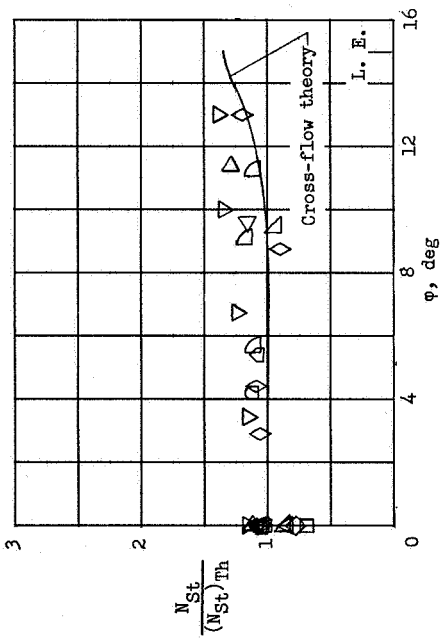
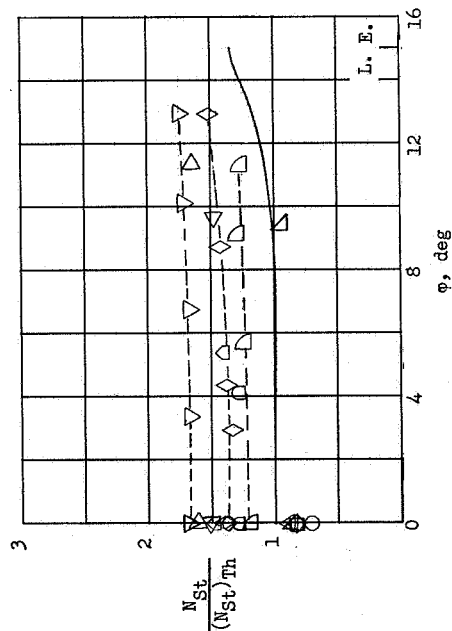
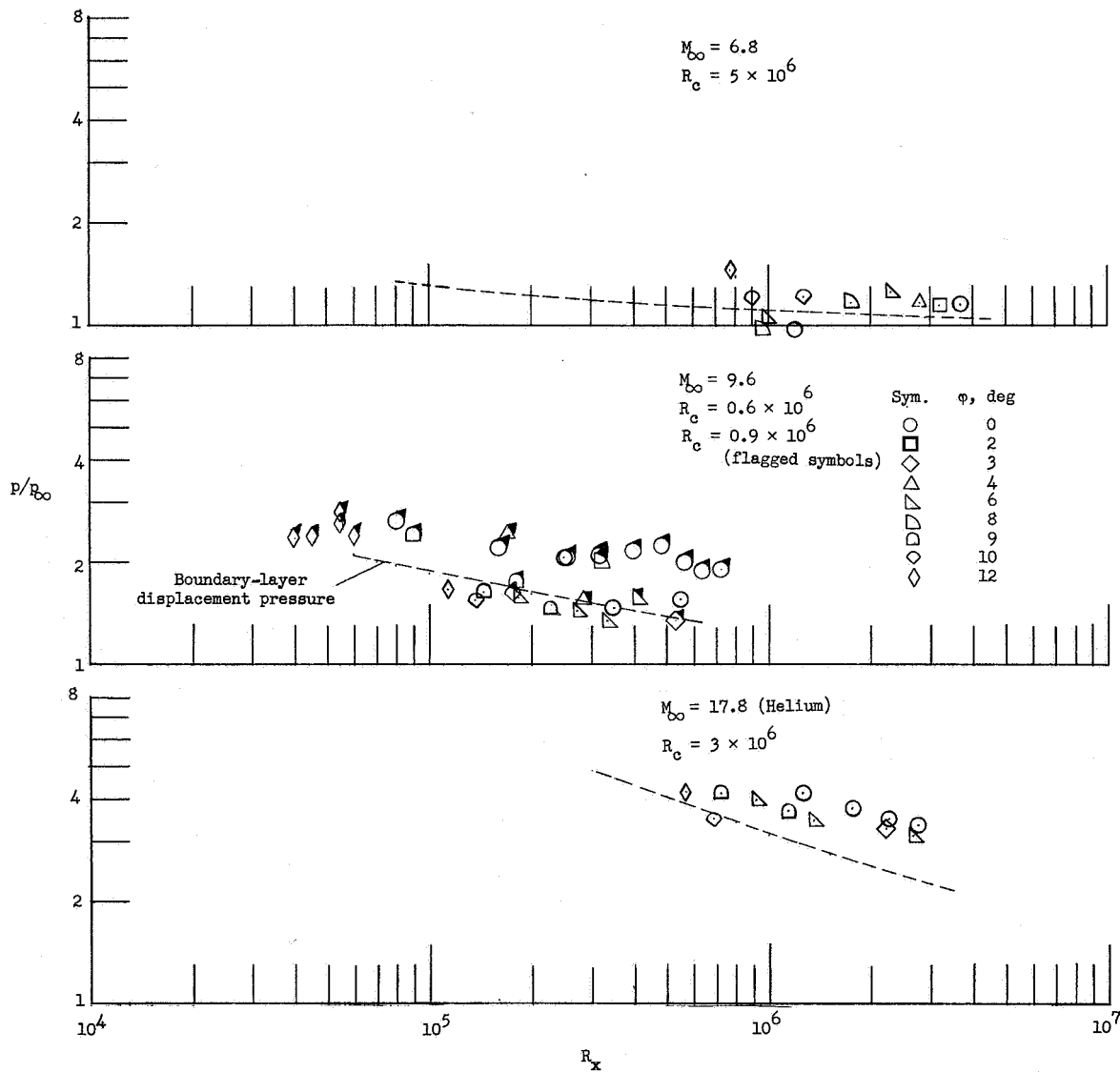
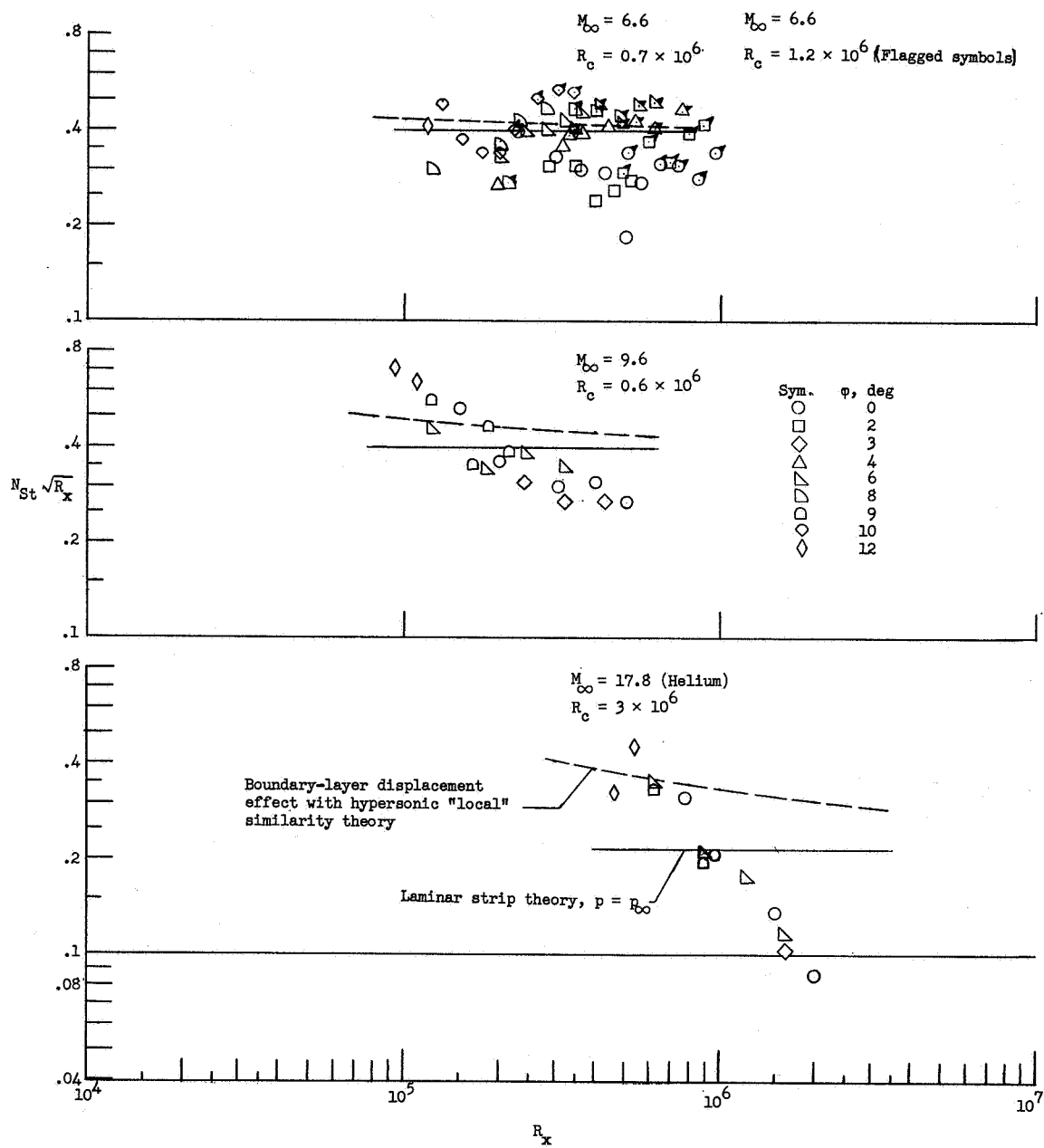
(e) $\alpha = 70^\circ$.(g) $\alpha = 90^\circ$.

Figure 24.- Concluded.



(a) Pressures.

Figure 25.- Variation of pressure and heat transfer with Mach number for flat, sharp-leading-edge, 75° swept delta wing near $\alpha = 0^\circ$.



(b) Heat transfer.

Figure 25.- Concluded.

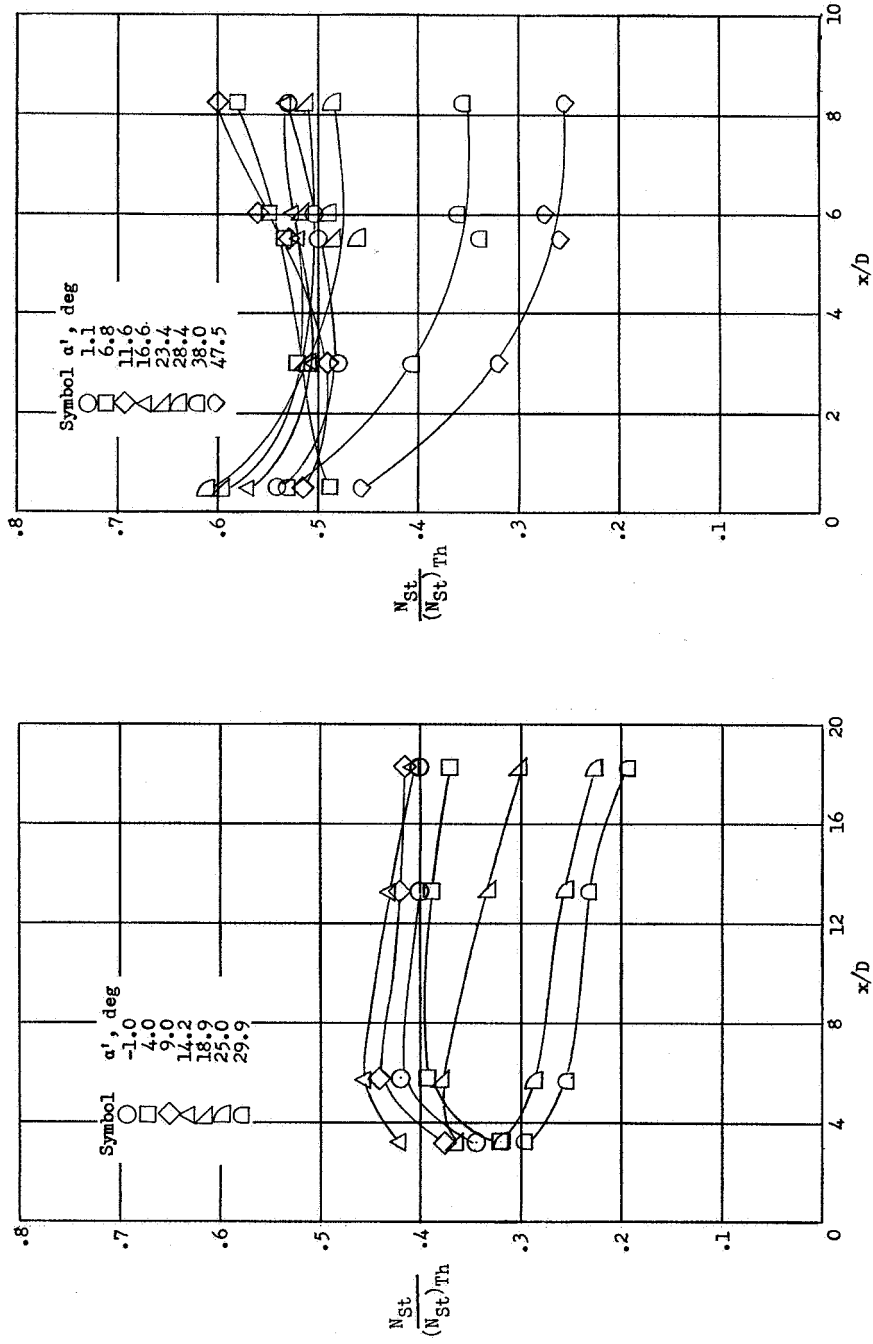
(a) $\Lambda = 75^\circ$; model IV.(b) $\Lambda = 60^\circ$; model V.

Figure 26.- Variation along leading edge of ratio of measured heating at center of leading edge to theoretical maximum leading-edge heating at the leading-edge stagnation line. Models IV and V at $M_\infty = 9.6$ and Reynolds number based on leading-edge diameter of 0.02×10^6 .

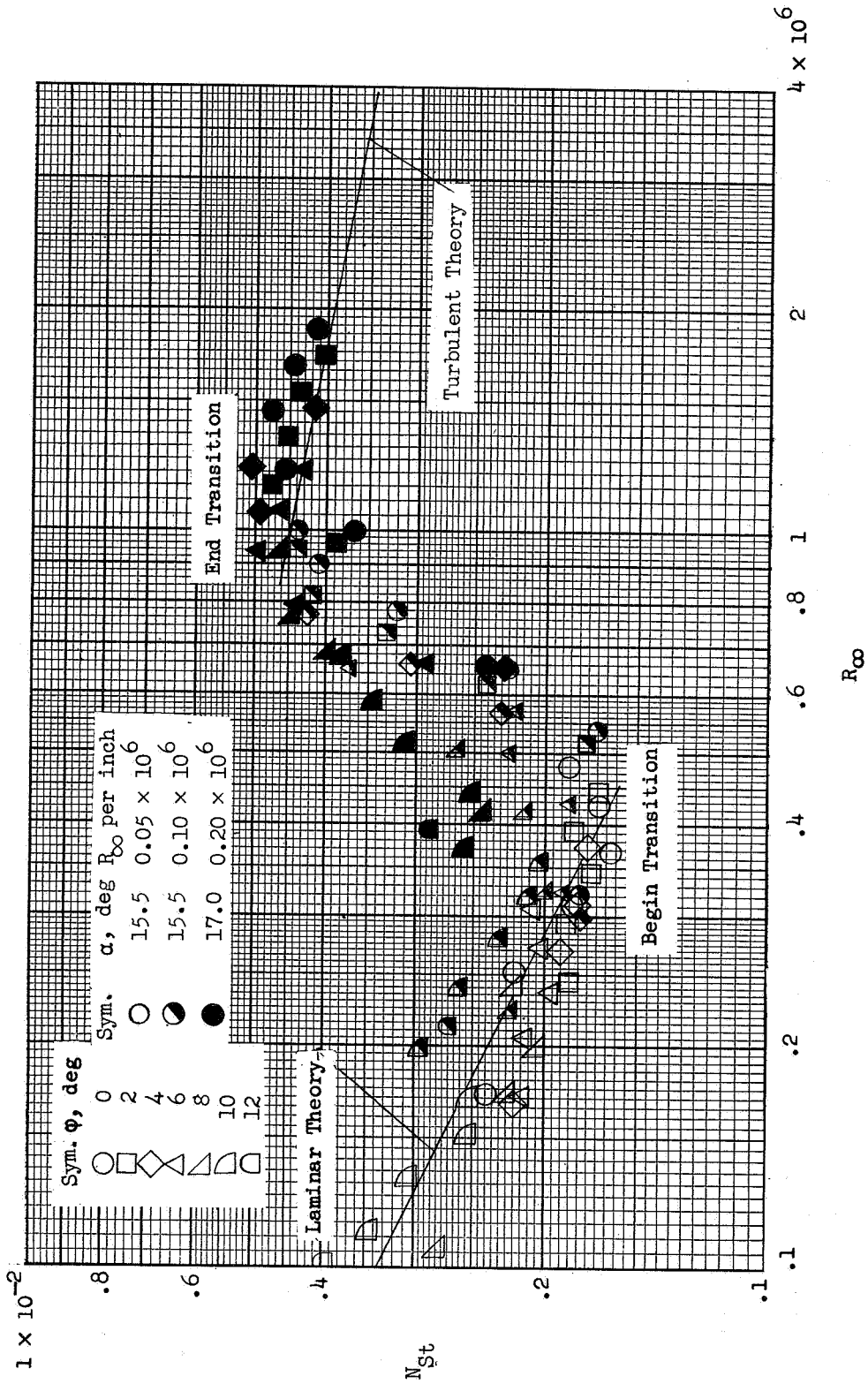


Figure 27.- Variation of Stanton number with Reynolds number for delta-wing model VI (flat, sharp leading edge, $\Lambda = 75^\circ$) at $M_\infty = 6.8$.

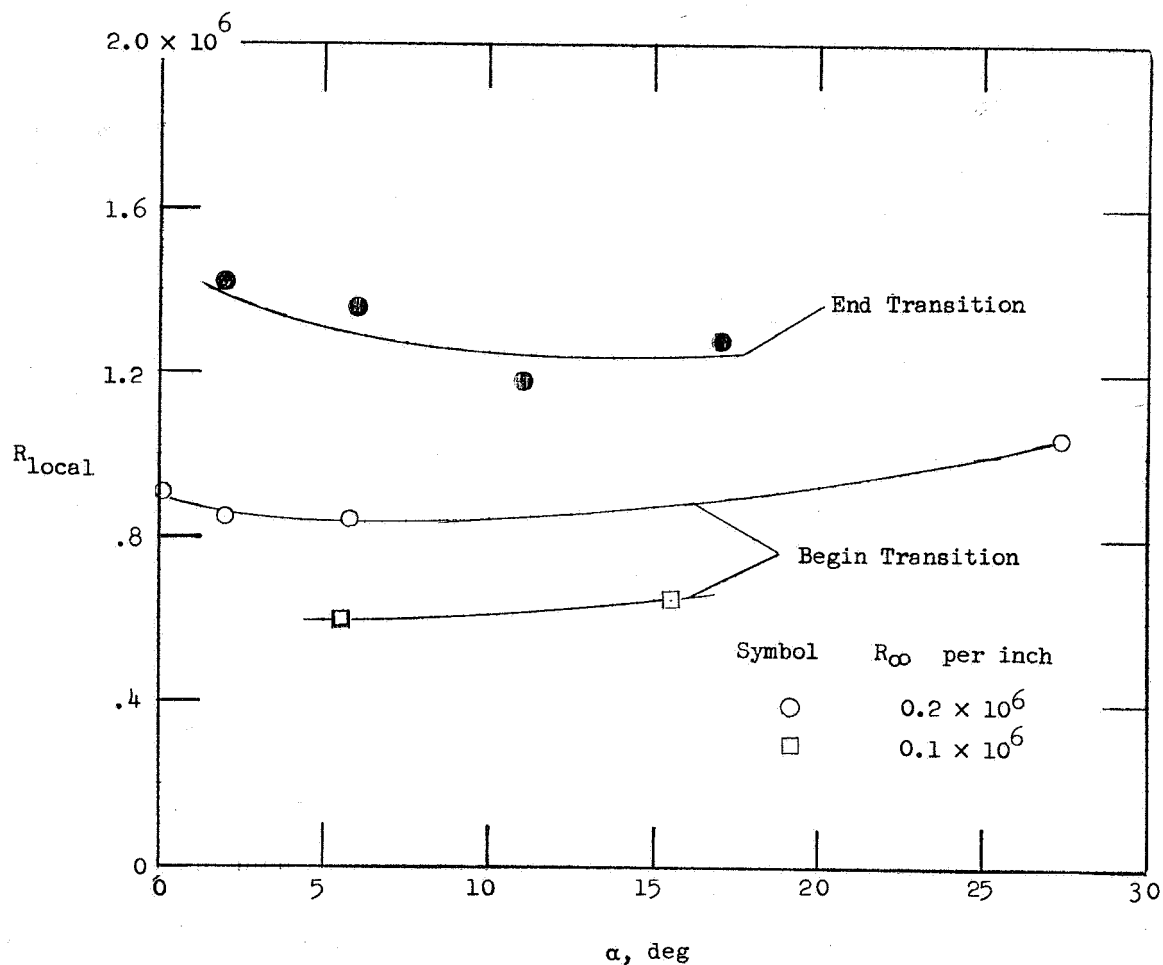


Figure 28.- Variation of local Reynolds number of transition with angle of attack for delta-wing model VI (flat, sharp leading edge, $\Lambda = 75^\circ$) at $M_\infty = 6.8$.

[REDACTED]

[REDACTED]

THIS PAGE IS UNCLASSIFIED

ERRATA

NASA Technical Memorandum X-688

INVESTIGATION OF HEAT TRANSFER AND
PRESSURES ON HIGHLY SWEPT FLAT AND DIHEDRALED DELTA WINGS
AT MACH NUMBERS OF 6.8 AND 9.6 AND
ANGLES OF ATTACK TO 90°By James C. Dunavant
June 1962

Page 7:

Insert the following paragraph after the first paragraph in the section labeled "Heating."

"Heat transfer coefficients were calculated by use of the measured model wall temperature. The model was cooled between each test to a temperature of about 75° or 80° F. During the 2 to 5 seconds required to stabilize tunnel flow conditions, the model wall temperature at most thermocouple stations rose less than 30° F. However, in a few instances when the heating was particularly severe (for example, the thermocouple nearest the vertex of Model VII at 90° angle of attack), the wall temperature rose 80° F before the aerodynamic heating was measured."

Page 68, figure 21:

Interchange the labels "Model I" and "Model VII" in the key above the list of x/c stations.

Pages 70, 71, and 72, figures 23 and 24 should be replaced with attached revised figures:

In these two figures the Stanton number, N_{St} , was inadvertently ratioed to an incorrect value of the theoretical Stanton number for cross-flow theory, $(N_{St})_{Th}$. The corrected figures 23 and 24 have the Stanton number ratioed to the theoretical Stanton number corresponding to the Stanton number of figure 21 labeled "Cross-flow theory (Pressure behind shock parallel to wing)." In addition, some of the symbols at stations $x/c = 0.83$ and 0.95 of these two figures were incorrect and have been corrected in the new figures.

THIS PAGE IS UNCLASSIFIED

Issued 2-25-63 Page 1 of 4 pages

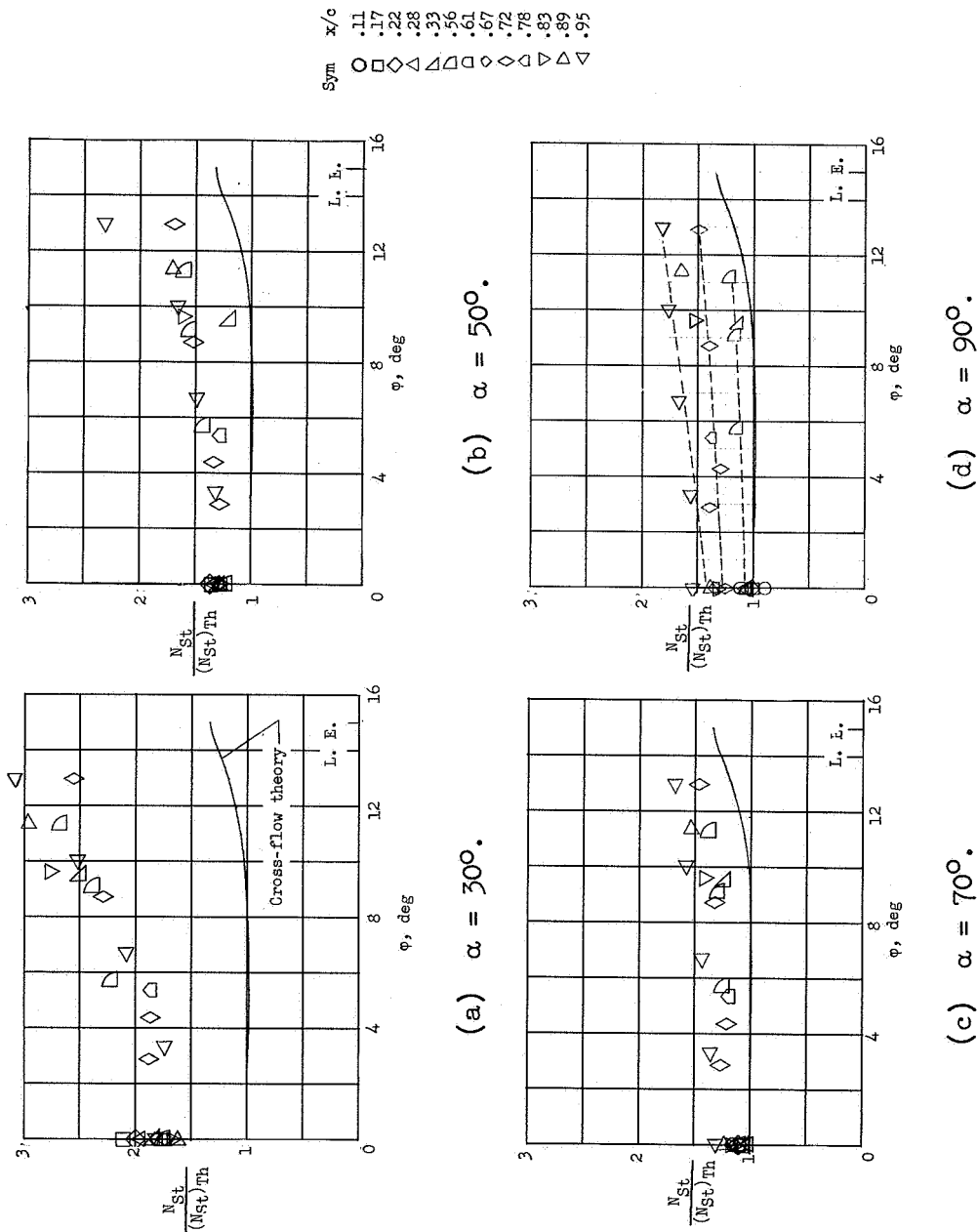


Figure 23.- Spanwise distribution of ratio of heating to theoretical laminar heating on center line for cross-flow theory. Delta-wing model VII ($\Lambda = 75^\circ$, $\Gamma = 0^\circ$, sharp leading edge) at $M_\infty = 6.8$ and $Re = 0.9 \times 10^6$.

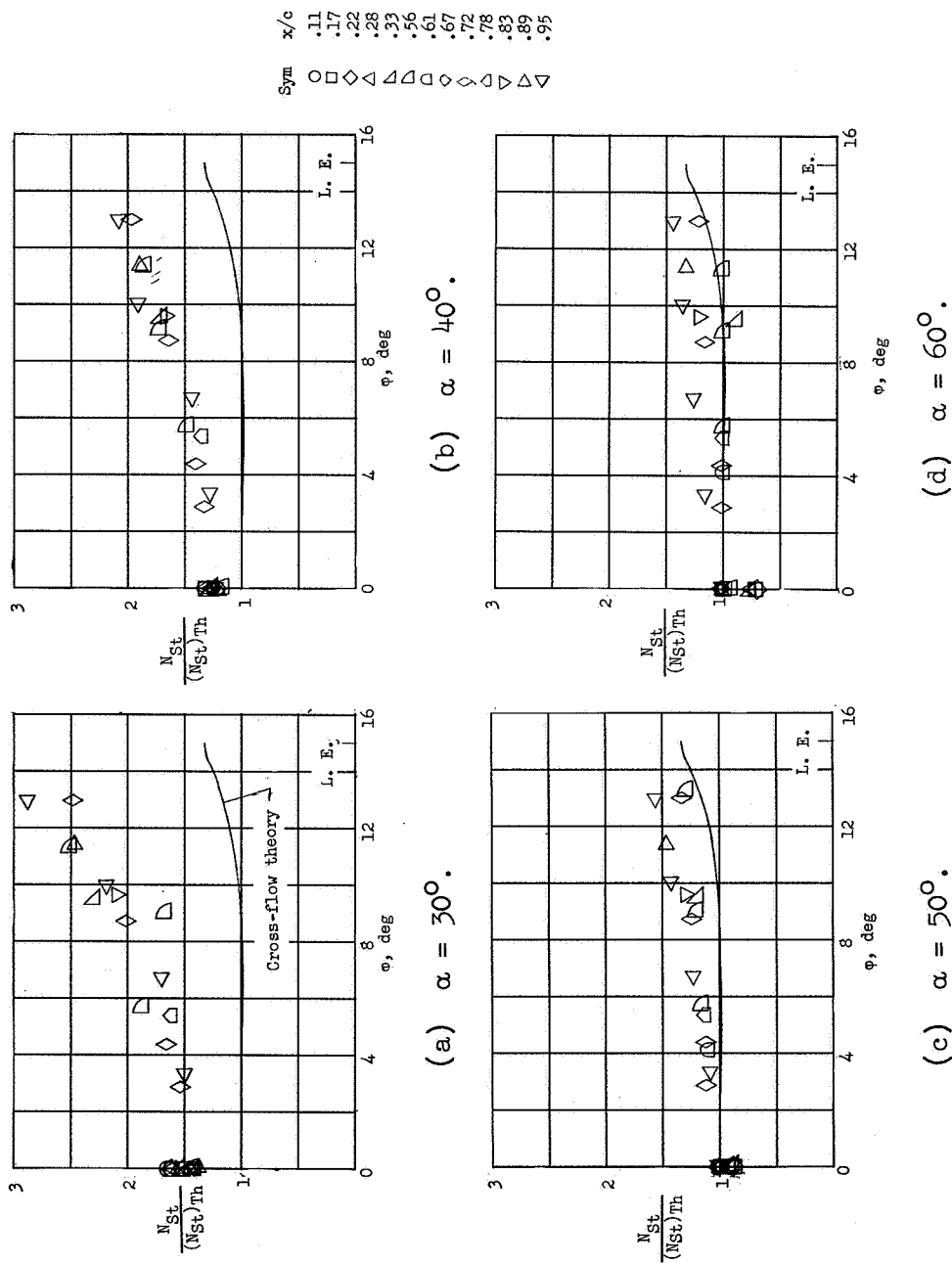
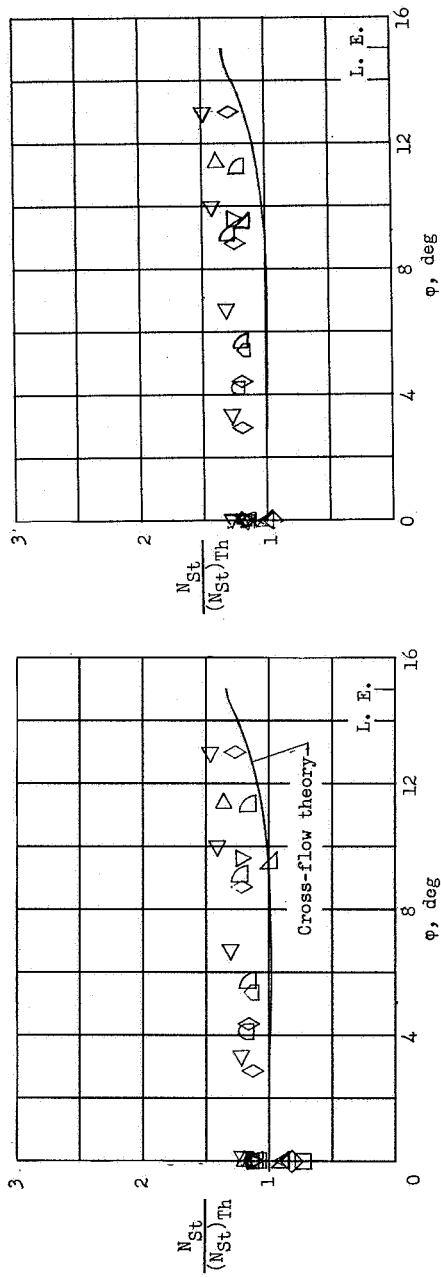


Figure 24.- Spanwise distribution of ratio of heating to theoretical laminar heating on center line for cross-flow theory. Delta-wing model VII ($\Lambda = 75^\circ$, $\Gamma = 0^\circ$, sharp leading edge) at $M_\infty = 9.6$ and $R_c = 0.5 \times 10^6$.



(f) $\alpha = 80^\circ$.

Sym x/c
 O .11
 □ .17
 ◇ .22
 △ .28
 ▽ .33
 △ .56
 □ .61
 ◇ .67
 △ .72
 △ .78
 ▽ .83
 ▽ .89
 ▽ .95

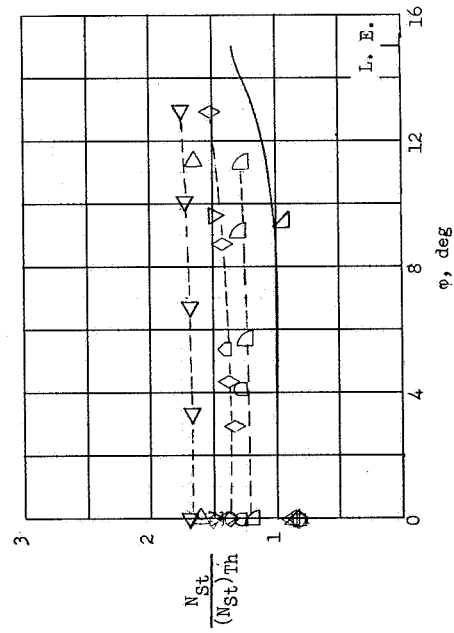


Figure 24.- Concluded.